공학박사 학위논문

차세대 리튬–공기 전지의 안정성 및 효율 향상에 관한 연구

Studies on enhancement of stability and efficiency in next generation lithium–oxygen batteries

2019 년 8 월

서울대학교 대학원

재료공학부

배 영 준

Abstract

Studies on enhancement of stability and efficiency in next generation lithium–oxygen batteries

Youngjoon Bae

Department of Materials Science and Engineering

College of Engineering

The Graduate School

Seoul National University

Current commercialized Li-ion batteries have been mainly used for portable electric devices because of their high power capabilities and energy densities. However, the energy densities of Li-ion batteries are insufficient for explosively growing energy storage systems such as electric vehicles (EVs) and large-scale energy storage systems (EESs) because of the heavy transition metals and limited Li^+ storage sites in cathode materials. To overcome these limitation of Li-ion batteries, many research projects have been devoted to developing next-generation energy storage system such as Li-O_2 batteries, Li-S batteries, and Li-organic batteries. Among them, Li-O_2 batteries based on simple electrochemical reaction ($2Li^+ + O_2 \leftrightarrow Li_2O_2$, $E^o = 2.96$ V *vs.* Li/Li^+) have attracted considerable attention as a potential

alternative chemistry owing to the extremely high theoretical energy density resulted from the absence of heavy transition metal and relatively high theoretical operating voltages. In addition, unlimited reaction sites based on formation and deposition of Li_2O_2 on the surface of cathode materials during discharge make the practical energy density of Li-O_2 cell high. Nevertheless, low efficiency and reversibility caused by various side reactions impede the commercialization of Li-O_2 batteries. Reactive oxygen species such as O_2^-, LiO_2, and Li_2O_2 which are produced during discharge are one of the main causes for the parasitic reactions in electrolyte and carbon cathode. Porous carbon materials have been mainly used as cathode materials in conventional Li-O_2 batteries, because carbon materials have suitable properties as a substrate for storage of Li_2O_2 such as high electric conductivity and specific surface area.

In this thesis, the ways for alleviating the parasitic reactions in Li-O_2 batteries are investigated. I demonstrate that the defect sites of carbon materials are the main reason of the parasitic reactions from not only carbon material, but also electrolyte. By reducing the defect sites on carbon through heat treatment, the degradation of carbon cathode and electrolyte are remarkably suppressed. Because reactive oxygen species are in contact with surface of carbon cathode during discharge, defect sites on the surface of carbon materials are thought to be more vulnerable to those reactive discharge products. Therefore, effective coating of the defect sites are suggested for the stabilization of carbon cathode and electrolyte in Li-O_2 batteries. In addition to these engineering for carbon materials, reactivity

control of oxygen radical should be conducted for the fundamental improvement of the stability of Li-O_2 batteries. Herein, I demonstrate that 5,5-dimethyl-1-pyrroline-N-oxide (DMPO) reduces the reactivity of the superoxide radical during discharge and charge, thus improves the cycle stability in Li-O_2 batteries.

Chapter 2 provides a new perspective on Li–O_2 batteries, for which the cyclic stability can be dramatically increased using well-ordered graphitic carbon-based cathode materials. Through a systematic investigation on the controlled carbon, I demonstrate that the graphitic crystallinity of carbon is an important factor in determining the stability of not only the cathode but also the electrolyte. To discern the degradation factors affecting the cathode from those affecting the electrolyte, I use carbon isotope (^{13}C)-based air electrodes with various degrees of graphitic crystallinity. Furthermore, *in situ* differential electrochemical mass spectroscopy analysis (DEMS) clearly demonstrates that as the crystallinity of the carbon increases, the CO_2 evolution from the cell is reduced, which leads to a three-fold enhancement in the cycle stability of the cell. The straightforward dependency of cycle life on the carbon crystal structure observed in this work provides guidelines for tailoring the carbon structures of carbon-based cathode materials for Li–O_2 batteries.

Chapter 3 demonstrates the effectiveness of coating as a strategy to suppress side reactions. The effect of coating protects the carbon electrode and suppresses electrolyte decomposition. Using *in situ* DEMS analysis and labeling the carbon air electrode with isotopic ^{13}C in an electrolyte composed of ^{12}C for the Li–O_2 cell, the major sources of the parasitic reactions were precisely identified as in Chapter 2.

During charge and discharge, byproducts from the electrolyte and carbon electrode were simultaneously detected to discern their origin by analyzing the ratio of $^{12}CO_2$ and $^{13}CO_2$ evolution. Moreover, I verify the evolution of these ratios with cycling for coated electrodes, providing important insight into the mechanism underlying the cycling enhancement provided by the coating. Furthermore, the limitations of this coating strategy are discussed, as we discover that the Li_2O_2 discharge product gradually grows at the interface between the coating material and carbon, eventually destabilizing the coating. This findings demonstrate that surface protection of the carbon electrode is a viable option to enhance the stability of Li–O_2 batteries; however, fundamental studies of the growth mechanism of the discharge product on the carbon surface are required along with more effective coating strategies.

Chapter 4 explore the effect of DMPO on the reactivity of superoxide radical which are formed during discharge and charge. The addition of DMPO in Li-O_2 cells results in reduction of side products such as Li_2CO_3 after discharge because of the stabilization of superoxide radical by DMPO. Unexpectedly, DMPO reduces the charge overpotential and facilitate the charge process through solution process which leads to homogenous decomposition of discharge products during charge. The detail mechanisms of DMPO are analyzed using electron magnetic resonance and cyclic voltammetry methods. During discharge, superoxide reacts with DMPO to form DMPO-O_2^- complex which finally produce Li_2O_2 thermodynamically when in contact with Li^+. In addition, superoxide radical during charge which originated from $Li_{2-x}O_2$ also forms relatively stable DMPO-O_2 complex and this complex is oxidized

at lower potential than oxidation potential of Li_2O_2 which results in the reduced charge overpotential. The stabilization effect of DMPO is demonstrated by *in situ* DEMS analyses mentioned earlier. Notably, the evolutions of $^{12}CO_2$ and $^{13}CO_2$ during charge with DMPO are suppressed with addition of DMPO. Correspondingly, the cycle stability of Li-O_2 cell with DMPO is enhanced about three times than that of Li-O_2 cell without DMPO. I believe that this finding can be the platform of the future research on the chemical stabilization of reactive radical products, and open up new possibility on the stable and efficient Li-O_2 batteries.

Keywords: Lithium-oxygen batteries, Degradation mechanism, Heat treatment, Atomic layer deposition, Superoxide carrier

Student Number: 2014-31063

Contents

List of Tables x

List of Figures xi

Chapter 1. Introduction 1

1.1. Introduction to lithium-oxygen battery 1

1.2. Research motivation and outlines 3

1.3. References 4

Chapter 2. Tuning the carbon crystallinity for highly stable lithium-oxygen batteries 7

2.1 Research background 7

2.2 Experimental method 10

2.2.1 Preparation of carbon materials 10

2.2.2 Characterization 11

2.2.3 Preparation of Li-O_2 cells 13

2.3 Results and Discussions 15

2.3.1 Characterization of heat treated ^{13}C materials 15

2.3.2 Electrochemical properties of Li–O_2 cells with heat treated

^{13}C cathodes 23
2.3.3 Gas analyses during charge in Li–O_2 cells with heat treated ^{13}C cathode 29
2.3.4. Electrochemical properties of Li–O_2 cells with heat treated ^{13}C cathodes containing lithium protective layer and redox mediator 41
2.4 Concluding remarks 44
2.5 References 45

Chapter 3. Enhanced stability of coated carbon electrode for lithium-oxygen batteries and its limitations ...51
3.1 Research background 51
3.2 Experimental method 55
3.2.1 Preparation of air electrodes 55
3.2.2 Preparation of protected Li metal 58
3.2.3 Preparation of Li-O_2 cells 59
3.2.3 Characterization 60
3.3 Results and Discussions 61
3.3.1 Characterization of ZnO-coated air electrodes 61
3.3.2 Electrochemical properties of Li–O_2 cells using ^{13}C and ZnO-coated ^{13}C cathodes with redox mediator and CPL 74
3.3.3 Gas analyses during charge in Li–O_2 cells with ^{13}C and

ZnO-coated ^{13}C cathodes 79
3.3.4 XPS analyses on ^{13}C and ZnO-coated ^{13}C cathodes after cycling in Li–O_2 cells 91
3.3.5 dq/dV analyses during cycling in Li–O_2 cells with ^{13}C and ZnO-coated ^{13}C cathodes 94
3.3.6 Degradation mechanism of ZnO-coated carbon cathodes 100
3.4 Concluding remarks 104
3.5 References 105

Chapter 4. Dual functioning single-molecule superoxide carrier for stable and efficient lithium-oxygen batteries 111
4.1 Research background 111
4.2 Experimental method 115
4.2.1 Preparation of Li–O_2 cells and conditions for electrochemical cell tests 115
4.2.2 Characterization 116
4.3 Results and Discussions 117
4.3.1 Verification of the effect of DMPO on the stabilization of Li–O_2 cells during discharge 117
4.3.2 Unexpected role of DMPO during charge in Li–O_2 cells 123
4.3.3 Visualization of the effect of DMPO during charge in Li–O_2 cells 126

4.3.4 Reaction mechanism of DMPO during discharge and charge in Li–O_2 cells 128
4.3.5 Gas analyses in Li–O_2 cells with and without DMPO and corresponding cycle stability 135
4.4 Concluding remarks 141
4.5 References 142

Chapter 5. Conclusion 147

Chapter 5. Abstract in Korean 150

Curriculum Vitae 154

List of Tables

Table 2.1. Specific information about the textural properties of ^{13}C, $^{13}C\_1600$, $^{13}C\_2000$, and $^{13}C\_2800$.

Table 3.1. I_D/I_G ratios of CNT, 8-cyc ZnO/CNT, and 15-cyc ZnO/CNT.

Table 4.1. The amounts of evolved gas in DEMS analyses during charge with and without DMPO.

List of Figures

Figure 2.1. (a) Raman spectra and (b) XRD patterns of pristine ^{13}C and heat-treated ^{13}C samples (1600 °C, 2000 °C, 2800 °C). (c–f) FE-TEM images and diffraction patterns of pristine ^{13}C and heat treated ^{13}C samples (1600 °C, 2000 °C, 2800 °C).

Figure 2.2. N_2 sorption isotherms of (a) ^{13}C, (b) ^{13}C_1600, (c) ^{13}C_2000, and (d) ^{13}C_2800.

Figure 2.3. Pore size distribution of (a) ^{13}C, (b) ^{13}C_1600, (c) ^{13}C_2000, and (d) ^{13}C_2800.

Figure 2.4. Discharge profile of Li–O_2 cell using pristine ^{13}C as the air electrode.

Figure 2.5. Electrochemical performances of Li–O_2 cells with restricted capacity of 0.5 mAh. (a) Discharge–charge profiles of the pristine ^{13}C cathode. (b) Cycle retention using the pristine ^{13}C cathode. (c) Discharge–charge profiles of the ^{13}C_1600 cathode. (d) Cycle retention using the ^{13}C_1600 cathode. (e) Discharge–charge profiles of the ^{13}C_2000 cathode. (f) Cycle retention using the ^{13}C_2000 cathode.

Figure 2.6. Discharge–charge profile of Li–O_2 cell using pristine ^{13}C as the air electrode.

Figure 2.7. Electrochemical performance of Li–O_2 cells. (a) Discharge–charge profiles of the ^{13}C_2800 cathode when the capacity is limited to 0.5 mAh. (b) Cycle retention using the ^{13}C_2800 cathode.

Figure 2.8. *In situ* DEMS analyses during 1st charging at (a) pristine ^{13}C, (b) ^{13}C_1600, and (c) ^{13}C_2000 cathodes. (d) Magnified amounts of

evolved $^{13}CO_2$ at pristine ^{13}C, ^{13}C_1600, and ^{13}C_2000 cathodes.

Figure 2.9. *In situ* DEMS analyses at pristine ^{13}C cathode during (a) 1st, (b) 5th, and (c) 10th charging. (d) Summary of the amounts of gas evolution at pristine ^{13}C cathode during cycling.

Figure 2.10. *In situ* DEMS analyses at ^{13}C_2000 cathode during (a) 1st, (b) 5th, (c) 10th, (d) 15th, and (e) 25th charge. (f) Summary of the amounts of gas evolution at ^{13}C_2000 cathode during cycling.

Figure 2.11. Summary of the amounts of (a) $^{13}CO_2$, (b) $^{12}CO_2$, and (c) O_2 evolution during cycling in ^{13}C and ^{13}C_2000.

Figure 2.12. Summary of the evolved gas ratio in terms of (a) $^{13}CO_2$, (b) $^{12}CO_2$, and (c) O_2 during cycling in ^{13}C and ^{13}C_2000.

Figure 2.13. FE-SEM images of (a) pristine ^{13}C cathode, (b) ^{13}C cathode after 15 cycles, (c) ^{13}C_2000 cathode, and (d) ^{13}C_2000 cathode after 15 cycles.

Figure 2.14. Electrochemical performances of Li–O_2 cells with the CPL an d the redox mediator. (a) Discharge–charge profiles of the pris tine ^{13}C cathode. (b) Cycle retention using the pristine ^{13}C cat hode. (c) Discharge–charge profiles of the ^{13}C_1600 cathode. (d) Cycle retention using the ^{13}C_1600 cathode. (e) Discharge –charge profiles of the ^{13}C_2000 cathode. (f) Cycle retention using the ^{13}C_2000 cathode.

Figure 3.1. TEM images of (a) pristine ^{13}C and (b) ZnO-coated ^{13}C. (c) XPS and (d, e) Raman spectra of pristine ^{13}C, 8-cyc ZnO/^{13}C, and 15-cyc

ZnO/^{13}C.

Figure 3.2. Discharge-charge profiles of Li–O_2 cells with (a) pristine CNT, (b) 8-cyc ZnO/CNT, and (c) 10-cyc Al_2O_3/CNT cathodes.

Figure 3.3. Discharge-charge profiles of Li–O_2 cells with (a) 15-cyc ZnO/ CNT and (b) 50-cyc ZnO/CNT cathodes.

Figure 3.4. SEM images of (a,d) pristine CNT, (b,e) 8-cyc ZnO/CNT, and (c,f) 50-cyc ZnO/CNT.

Figure 3.5. TEM images of (a) pristine CNT and (b) ZnO-coated CNT. (c) XPS and (d, e) Raman spectra of CNT, 8-cyc ZnO/CNT, and 15-cyc ZnO/CNT.

Figure 3.6. (a) EDS mapping region in TEM images of the ZnO-coated CNT. (b–d) EDS mapping (C, Zn, and O elements) of the ZnO-coated CNT. (e) EDS spectrum of the ZnO-coated CNT.

Figure 3.7. Discharge–charge profiles of Li–O_2 cells with the LiI redox mediator and CPL-protected Li metal using (a) pristine ^{13}C and (c) ZnO-coated ^{13}C as the air electrodes at a current rate of 0.1 mA/cm^2. Cycle stability of each Li–O_2 cell using the (b) pristine ^{13}C and (d) ZnO-coated ^{13}C as the air electrodes.

Figure 3.8. Discharge–charge profiles of Li–O_2 cells with the (a) pristine ^{13}C cathode and (c) ZnO-coated ^{13}C cathode. Cyclability of Li -O_2 cells with the (b) pristine ^{13}C cathode and (d) ZnO-coated ^{13}C cathode.

Figure 3.9. *In situ* DEMS analyses in Li–O_2 cells with pristine ^{13}C cathod e during (a) first, (b) fifth, and (c) tenth charge. (d) Ratios of evolved gases at pristine ^{13}C cathode during cycling.

Figure 3.10. *In situ* DEMS analyses in Li–O_2 cells with ZnO-coated ^{13}C cathode during (a) first, (b) fifth, (c) tenth, and (d) fifteenth charge. (e) Amounts of evolved gases at the ZnO-coated ^{13}C cathode during cycling. Summary of the amounts of (f) $^{12}CO_2$, (g) $^{13}CO_2$, and (h) O_2 evolutions during cycling at pristine ^{13}C and ZnO-coated ^{13}C cathodes.

Figure 3.11. *In situ* DEMS analyses in Li–O_2 cells with (a) pristine ^{13}C, (b) 8-cyc ZnO/^{13}C, and (c) 15-cyc ZnO/^{13}C cathodes during the first charge.

Figure 3.12. *In situ* DEMS analyses during charging of chemically synthesized Li_2O_2.

Figure 3.13. XPS spectra of pristine ^{13}C electrode and ZnO-coated ^{13}C electrode (a, b) as prepared, (c, d) after five cycles, (e, f) after ten cycles, and (g, h) after fifteen cycles, respectively.

Figure 3.14. dq/dV curves at (a) first, (b) fifth, (c) tenth, (d) fifteenth cycles in Li-O_2 cell with pristine ^{13}C cathode as a cathode.

Figure 3.15. Magnified dq/dV curves at (a) first, (b) fifth, (c) tenth, (d) fifteenth cycles in Li-O_2 cell with pristine ^{13}C cathode as a cathode.

Figure 3.16. dq/dV curves at (a) first, (b) fifth, (c) tenth, (d) fifteenth cycles in Li-O_2 cell with ZnO-coated ^{13}C cathode as a cathode.

Figure 3.17. Magnified dq/dV curves at (a) first, (b) fifth, (c) tenth, (d) fifteenth cycles in Li-O_2 cell with ZnO-coated ^{13}C cathode as a cathode.

Figure 3.18. (a,b) TEM images of ZnO-coated ^{13}C cathode after cycling. TEM images of ZnO-coated CNT cathode after (c) first, (d) third, and (e,f) fifth discharge.

Figure 3.19. TEM images of ZnO-coated CNT cathode after (a) third and (b) fifth charge. The capacity was limited to 1000 mAh g^{-1}.

Figure 4.1. (a) XRD and (b) Raman spectra of discharged cathode with and without DMPO. XPS (c) Li 1s and (d) C 1s spectra of discharged cathode with and without DMPO. DEMS analyses with acid treatment on discharged ^{13}C cathode (e) without DMPO and (f) with DMPO.

Figure 4.2. SEM images of (a, b) pristine carbon cathode, (c, d) 0.5 mAh discharged carbon cathode without DMPO, and (e, f) 0.5 mAh discharge carbon cathode with DMPO.

Figure 4.3. First discharge/charge curves of Li-O_2 cells with presence or absence of DMPO during discharge and charge. (a) Discharge and charge without DMPO (red)/Discharge and charge with DMPO (blue) (b) Discharge and charge without DMPO (red)/Discharge with DMPO and charge without DMPO (purple) (c) Discharge and charge without DMPO (red)/Discharge without DMPO and charge with DMPO (light blue)

Figure 4.4. SEM images of carbon cathode on various state of charge with and without DMPO. (a, g) 0.5 mAh discharged cathode without DMPO. (b-f) 0.015, 0.05, 0.1, 0.2, and 0.5 mAh charged cathode with DMPO, respectively. (h-l) 0.015, 0.05, 0.1, 0.2, and 0.5 mAh charged cathode without DMPO, respectively. Scale bar: 1 μm.

Figure 4.5. (a) EPR analyses after discharge to 0.1, 0.2, 0.3, 0.4, and 0.5 mAh with DMPO. (b) EPR analyses after charge the discharg ed cathode without DMPO (0.5 mAh) to 0 (5h rest), 0.015, 0. 05, 0.2, and 0.5 mAh with DMPO. All the EPR analyses wer e conducted using the electrolytes in the cells. (c) CV curves in Ar and O_2 atmosphere using 1 M TBATFSI in TEGDME as the electrolyte (without DMPO). (d) CV curves in Ar and O_2 atmosphere using 1 M TBATFSI + 0.2 M DMPO in TEG DME as the electrolyte (with DMPO).

Figure 4.6. (a, b) CV curves in Ar atmosphere using 1 M TBATFSI + 0.2 M DMPO in TEGDME as the electrolyte with 1.8~4.5 V and 1.8~4.0 V voltage scans, respectively. (c) CV curves in O_2 atmosphere using 1 M TBATFSI + 0.2 M DMPO in TEGDME as the electrolyte for 100 cycles.

Figure 4.7. DEMS analyses of the Li-O_2 cells using ^{13}C as the carbon cathodes (a) without DMPO and (b) with 0.2 M DMPO, respectively. Discharge/Charge voltage profiles of Li-O_2 cells using hierarchical CNT as the carbon cathodes with (c) 0 M, (d) 0.2 M, and (e) 0.5 M DMPO, respectively. (f) Cycle stabilities of the Li-O_2 cells with 0 M, 0.2 M, and 0.5 M DMPO.

Figure 4.8. Discharge/Charge voltage profiles of Li-O_2 cells using P50 as the carbon cathode with various concentrations of DMPO.

Chapter 1. Introduction

1.1 Introduction to lithium-oxygen batteries

There has been ever increasing demand for high-energy-density energy storage systems with advances in technologies such as electric vehicles and mobile electronic devices. Current state-of-the-art Li-ion batteries have been a great success in battery markets for the mobile devices over the past few decades, owing to their excellent performance such as high power capability.[1, 2] Nevertheless, Li-ion batteries have a limitation on theoretical specific energy because of the use of heavy transition metal and confined Li ion storage sites in crystal structure of electrode materials. Therefore, alternative energy storage systems with high specific energy should be developed for the future demand.

Among several candidates for high-specific-energy systems, Li-O_2 batteries have attracted great attention owing to their extremely high theoretical specific energy (~3500 Wh/kg) based on the simple electrochemical reaction: $2Li^+ + O_2 + 2e^- \leftrightarrow Li_2O_2$ (E^o = 2.96 V vs. Li/Li^+).[3-5] Li-O_2 batteries are usually composed of Li metal, separator with liquid electrolyte, and porous carbon cathode. Li_2O_2 as the discharge product is formed on the carbon cathode during discharge, and is electrochemically decomposed during charge evolving oxygen gas. In general, the detailed discharge reactions in Li-O_2 cells can be described as below.[6-10]

$$O_2(g) + e^- \rightarrow O_2^-(solv) \quad (1)$$

$$Li^+(solv) + O_2^- \rightarrow LiO_2 \quad (2)$$

$$LiO_2 + Li^+ + e^- \rightarrow Li_2O_2(s) \quad (3)$$

$$2LiO_2 \rightarrow Li_2O_2(s) + O_2 \quad (4)$$

At first, oxygen is reduced to a superoxide radical (O_2^-) which subsequently reacts with Li^+ to produce metastable lithium superoxide (LiO_2). Then, LiO_2 is electrochemically reduced or chemically disproportionates, both resulting in lithium peroxide (Li_2O_2).

Although Li-O_2 batteries have a great potential as the future energy storage system, there are several problems which should be resolved for the commercialization. Representative problem is side reactions in electrolyte and carbon cathode during cycling. The intermediate radical species, such as O_2^- or LiO_2, during cycling have been shown to be chemically reactive, leading to chemical degradations of the cell components.[11-20] Side products such as lithium carbonate which is electrically insulating, are formed by these side reactions, whose accumulation on the carbon cathode results in large overpotential and exacerbates the degradations.[18-22] For the realization of commercial Li-O_2 batteries, the side reactions in electrolyte and carbon cathode should be addressed.

1.2 Research motivation and outlines

Although Li-O_2 batteries have been researched extensively as the next generation energy storage system, there are several problems to be resolved such as side reactions in electrolyte and carbon cathode. One of the main causes of these side reactions is reactive radical species produced during cycling of Li-O_2 batteries. To overcome the side reaction issue, the reactive sites where radical species can easily attack should be demonstrated. Based on the demonstration, protection of the reactive sites would block the side reactions in electrolyte and carbon cathode. In this light, I developed simple heat treatment method to determine the reaction sites of the carbon cathode. After the origin of the side reaction was confirmed, I introduced atomic layer deposition (ALD) method to carbon cathode fabrication for protection of reactive sites on carbon cathode. Another method to mitigate the side reaction would be controlling the reactivity of reactive radical species. Through the reactivity control, side reactions related to radical species could be effectively reduced. With these motivations, I demonstrate the effects of heat treatment, ALD protection, and radical capturing on the stability and efficiency of Li-O_2 batteries.

1.3 References

[1] P. G. Bruce, B. Scrosati, J. M. Tarascon, *Angew. Chem., Int. Ed*. **2008**, 47, 2930.

[2] M. Armand, J. M. Tarascon, *Nature* **2008**, 451, 652.

[3] M. D. Bhatt, H. Geaney, M. Nolan, C. O'Dwyer, *Phys. Chem. Chem. Phys.* **2014**, 16, 12093.

[4] P. G. Bruce, S. A. Freunberger, L. J. Hardwick, J.-M. Tarascon, *Nat. Mater.* **2012**, 11, 19.

[5] H.-D. Lim, B. Lee, Y. Bae, H. Park, Y. Ko, H. Kim, J. Kim, K. Kang, *Chem. Soc. Rev.* **2017**, 46, 2873.

[6] Z. W. Chang, J. J. Xu, Q. C. Liu, L. Li, X. b. Zhang, *Adv. Energy Mater.* **2015**, 5, 1500633.

[7] V. S. Bryantsev, V. Giordani, W. Walker, M. Blanco, S. Zecevic, K. Sasaki, J. Uddin, D. Addison, G. V. Chase, *J. Phys. Chem. A* **2011**, 115, 12399.

[8] R. Cao, E. D. Walter, W. Xu, E. N. Nasybulin, P. Bhattacharya, M. E. Bowden, M. H. Engelhard, J. G. Zhang, *ChemSusChem* **2014**, 7, 2436.

[9] D. Aurbach, B. D. McCloskey, L. F. Nazar, P. G. Bruce, *Nat. Energy* **2016**, 1, 16128.

[10] L. Johnson, C. Li, Z. Liu, Y. Chen, S. A. Freunberger, P. C. Ashok, B. B. Praveen, K. Dholakia, J.-M. Tarascon, P. G. Bruce, *Nat. Chem.* **2014**, 6, 1091.

[11] S. A. Freunberger, Y. Chen, N. E. Drewett, L. J. Hardwick, F. Bardé, P. G. Bruce, *Angew. Chem., Int. Ed.* **2011**, 50, 8609.

[12] X. Yao, Q. Dong, Q. Cheng, D. Wang, *Angew. Chem., Int. Ed.* **2016**, 55, 11344.

[13] V. S. Bryantsev and M. Blanco, *J. Phys. Chem. Lett.* **2011**, 2, 379.

[14] V. S. Bryantsev, *Chem. Phys. Lett.* **2013**, 558, 42.

[15] V. S. Bryantsev, J. Uddin, V. Giordani, W. Walker, D. Addison, G. V. Chase, *J. Electrochem. Soc.* **2013**, 160, A160.

[16] A. Khetan, A. Luntz, V. Viswanathan, *J. Phys. Chem. Lett.* **2015**, 6, 1254.

[17] A. Khetan, H. Pitsch, V. Viswanathan, *J. Phys. Chem. Lett.* **2014**, 5, 2419.

[18] Y. Bae, D.-H. Ko, S. Lee, H.-D. Lim, Y.-J. Kim, H.-S. Shim, H. Park, Y. Ko, S. K. Park, H. J. Kwon, H. Kim, H.-T. Kim, Y.-S. Min, D. Im, K. Kang, *Adv. Energy Mater.* **2018**, 8, 1702661.

[19] Y. Bae, Y. S. Yun, H.-D. Lim, H. Lee, Y.-J. Kim, J. Kim, H. Park, Y. Ko, S. Lee, H. J. Kwon, H. Kim, H.-T. Kim, D. Im, K. Kang, *Chem. Mater.* **2016**, 28, 8160.

[20] M. M. Ottakam Thotiyl, S. A. Freunberger, Z. Peng, P. G. Bruce, *J. Am. Chem. Soc.* **2012**, 135, 494.

[21] B. D. McCloskey, A. Speidel, R. Scheffler, D. Miller, V. Viswanathan, J. Hummelshøj, J. Nørskov, A. Luntz, *J. Phys. Chem. Lett.* **2012**, 3, 997.

[22] D. M. Itkis, D. A. Semenenko, E. Y. Kataev, A. I. Belova, V. S. Neudachina, A. P. Sirotina, M. Hävecker, D. Teschner, A. Knop-Gericke, P. Dudin, A.

Barinov, E. A. Goodilin, Y. Shao-Horn, L. V. Yashina, *Nano Lett*. **2013**, 13, 4697.

Chapter 2. Tuning the carbon crystallinity for highly stable lithium-oxygen batteries

2.1 Research Background

$Li–O_2$ batteries have attracted much attention because of their exceptionally high theoretical energy density and the use of the unlimited O_2 resources from ambient air using a relatively simple reaction: $2Li^+ + O_2 + 2e^- \rightarrow Li_2O_2$ (E^o = 2.96 V vs. Li/Li^+).[1-3] The deposition and striping of the discharge product, Li_2O_2, during the cycling occurs primarily on the air electrode; thus, the design of its architecture and constituent material is important to maximize the performance of $Li–O_2$ batteries and has been a central area of research.[4-16] Carbon-based materials were naturally the first choice for such an air electrode because of their desirable properties, including their high electrical conductivity, light weight, and chemical stability.[7-9, 14, 17-19] Moreover, it is comparatively easier to prepare a high-surface-area electrode using carbon-based materials to achieve high specific capacity than for any other possible electrode materials by taking advantage of well-known technologies with low

processing and raw material costs.[20, 21] Thus, the use of carbon as the air electrode appears to be the most suitable choice, especially for low-cost and high-energy Li–O_2 batteries. Consequently, various types of carbon-based air electrodes have been extensively investigated, such as activated porous carbon, carbon nanotube, or graphene derivatives.[19, 22-42]

Recent studies, however, have indicated that the carbon-based air electrode could be one of the sources that contribute to the cycle degradation of Li–O_2 batteries.[43-48] Although the capacity fading is mainly attributed to continuous side reactions involving electrolyte degradation and passivation of the air electrode with byproducts such as Li_2CO_3 during the cell operation,[45, 48] it was observed that the interfacial reaction between the carbon surface and Li_2O_2 was partly responsible for the formation of the Li_2CO_3 byproducts, questioning the chemical stability of carbon with the discharge product.[45, 47] Once the byproducts are deposited on the air electrode, they not only clog the air electrode, hindering the transport of O_2 and Li ions but also deteriorate the carbon electrode by forming Li_2CO_3, which can decompose upon the charging reaction evolving CO_2 gases. Furthermore, at high-voltage charging, the electrochemical corrosion of carbon itself may occur, triggering subsequent decomposition of the electrolyte.[44] Although such side reactions induced by the carbon can be avoided using Au or TiC electrodes, practical applications are significantly limited because of the cost and unacceptably low specific capacity.[4, 5] Therefore, identifying a strategy to minimize the side reactions

induced by the carbon electrode might be a more appropriate approach to efficiently enhance the cyclic stability of Li–O_2 batteries.

Herein, we investigate the correlation between the side reactions in the Li–O_2 cell and the characteristics of carbon in the electrode from the perspective of both the electrode and electrolyte stabilities. To discern the origins of the carbon-containing byproducts, all the carbon air electrodes were fabricated using the carbon isotope ^{13}C, whereas the electrolyte primarily contains naturally abundant ^{12}C, which could be individually probed using *in situ* differential electrochemical mass spectroscopy (DEMS) analysis. The carbon local structure of the active ^{13}C electrode materials were systematically controlled using simple heat treatments with varying degrees of sp^2 and sp^3 ratios. Differences in carbon local ordering were observed to induce dramatic changes in the corrosion of the active carbon electrode and electrolyte decomposition, leading to distinct cyclic performances. These findings clearly demonstrate the importance of controlling the carbon microstructure in the active cathode material and hint at the prospective future direction of designing a stable air electrode for Li–O_2 batteries.

2.2 Experimental method

2.2.1 Preparation of carbon materials

The active carbon materials composed of ^{13}C were purchased from Sigma–Aldrich, USA (99%). The samples were heated to 1600, 2000, or 2800 °C, respectively, in a high-temperature graphite furnace for 2 h at a heating rate of 5 °C min^{-1}. A graphite furnace was used because conventionally used furnaces have a limitation in the heating temperature (< 1800 °C). The samples were labeled based on the heating temperature as ^{13}C_1600, ^{13}C_2000, and ^{13}C_2800.

2.2.2 Characterization

The morphologies of the samples were characterized using field-emission scanning electron microscopy (FE-SEM, MERLIN Compact, ZEISS, Germany) and field-emission transmission electron microscopy (FE-TEM, JEM2100F, JEOL, Japan). The Raman spectra (LabRam HR, Horiba Jobin-Yvon, France) were recorded using a continuous-wave linearly polarized laser (wavelength: 514.5 nm; 2.41 eV; power: 16 mW). The laser beam was focused using a 100× objective lens, resulting in a spot diameter of approximately 1 μm. The acquisition time and number of circulations to collect each spectrum were 10 s and 3, respectively. X-ray diffraction (XRD, DMAX 2500, Rigaku, Japan) was performed using Cu Kα radiation (wavelength $\lambda = 0.154$ nm), and the diffractometer was operated at 40 kV and 100 mA. The porous properties of the samples were analyzed using nitrogen adsorption and desorption isotherms that were obtained using a surface area and porosimetry analyzer (ASAP 2020, Micromeritics, USA) at -196 °C. In situ gas detection spectroscopy was used to analyze the gases evolving from the Li–O_2 cell during charging. The in situ DEMS system was composed of a mass spectrometer (MS) (HPR-20, Hiden Analytical, UK) and the potentio-galvanostat. Before the DEMS experiment, the cells were initially discharged and connected to the MS to detect the gases evolving during the charging process. The cells were fully relaxed in Ar for 4 h before charging. Ar was used as a carrier gas, and the flow rate of Ar was 10 mL min-1. The MS was calibrated for O_2, CO_2, and Ar using a 0.22% O_2,

0.20% CO_2, and 99.58% Ar (v/v) mixture gas. The calibration included modification of the relative sensitivities of each gas to prevent nonlinearity and cross-sensitivity.

2.2.3 Preparation of Li–O_2 cells

The air electrode for the Li–O_2 cell was fabricated using a mixture of the prepared ^{13}C carbon and binder (Kynar 2801) at a weight ratio of 90:10. Th e mixture was dispersed in N-methy-2-pyrrolidone (NMP, Sigma-Aldrich, 99. 5%) and cast onto a Ni-mesh current collector. The loading densities of the air electrodes were ~1mg cm^{-2}. Li metal foil (7/16-inch diameter), a glass fi ber separator (Whatman GF/D microfiber filter paper, 2.7-μm pore size), and the prepared air electrode were stacked in sequence in a Swagelok-type cell. The electrolyte was 1 M lithium bis(trifluoromethane)sulfonimide (LiTFSI) in tetraethylene glycol dimethylether (TEGDME), and 0.05M LiI was added int o the electrolyte for the redox mediator test. Composite protective layer (CP L) on Li metal was fabricated as follow. A slurry composed of 50 wt% of Al_2O_3 powder, 12.5 wt% of PVdF-HFP polymer, and 37.5 wt% of liquid ele ctrolyte (1 M $LiClO_4$ in EC/PC (50/50 by volume)) was prepared as a plasti cizer to form a gel polymer electrolyte phase dissolved in N,N-dimethylform amide (DMF, Sigma-Aldrich, 99.8%) solvent. The CPL (25 μm thickness) w as prepared using a doctor-blade coating of the resulting slurry on Li metal foil (Honzo, thickness of 450 μm) and subsequent drying at 25 °C for 2 h under vacuum. All the cells were assembled in a glove box and operated in an O_2 atmosphere (770 Torr). Each cell was relaxed for 1 h in an O_2 atmo sphere before testing to ensure cell stabilization. The cells were operated usi ng the capacity-limited mode of 0.5 mAh within the voltage range of 2.0 to

4.5 V. All the cells were galvanostatically discharged and charged at a curre nt density of 0.1 mA cm^{-2}. A potentio-galvanostat (WBCS 3000, WonA Tec h, Korea) was used to measure the electrochemical properties.

2.3 Results and Discussions

2.3.1. Characterization of heat treated ^{13}C materials.

The ^{13}C carbon samples used for the fabrication of the air electrode were characterized as shown in Figure 2.1. The as-received sample (labeled ^{13}C) exhibited the typical characteristics of amorphous carbon; however, the microstructure of the ^{13}C sample notably changed with an increase in the heat-treated temperature (HTT). The Raman spectra of ^{13}C, $^{13}C\_1600$, $^{13}C\_2000$, and $^{13}C\_2800$ in Figure 2.1a reveal the systematic variation of the intensity ratio of the *D* and *G* bands. The *D* and *G* bands (centered at ~1291 and ~1521 cm^{-1}, respectively) correspond to disorder in the A_{1g} breathing mode of the six-fold aromatic ring near the basal edge and the hexagon structure related to the E_{2g} vibration mode of the sp^2-hybridized C atoms, respectively. Thus, the I_G/I_D intensity ratios are an indicator of the crystallinity and domain size of the hexagonal carbon structure.[49] With an increase of the HTT, Figure 2.1a shows that the I_G/I_D intensity increases and the *G* and *D* bands become narrower, indicating the growth of the hexagonal carbon structures in the samples. The *D*, *G*, and 2*D* bands of the $^{13}C\_2800$ are slightly shifted into high-frequency regions, which may have originated from contamination of the ^{13}C by ^{12}C during the heating process in the graphite furnace (see the supporting information for details). According to the nitrogen adsorption and desorption isotherm measurements, all the samples displayed International Union of Pure and Applied Chemistry (IUPAC) Type IV shapes, indicating that they exhibit mesoporous structures (Figure 2.2). In addition,

the samples exhibited similar pore size distributions with a main pore size of ~25 nm (Figure 2.3). However, the specific surface area of ^{13}C_2800 was significantly reduced compared with the other ^{13}C samples because of the sintering effect (Table 2.1). In this respect, the electrochemical data of the ^{13}C_2800 samples in the following sections were only used to support the results of the other samples. The XRD patterns of the samples also indicated the development of a graphitic structure with increasing HTT, as demonstrated by the growth of the characteristic graphite (002) peak (Figure 2.1b). It could be directly observed by FE-TEM (Figure 2.1c–f). The FE-TEM images of ^{13}C in Figure 2.1c exhibit a highly disordered carbon structure. However, the image of ^{13}C_1600 in Figure 2.1d reveals the presence of graphitic layers, and more graphitic structures with high crystallinity can be observed in the ^{13}C_2000 samples in Figure 2.1e. The ^{13}C_2800 displays the most developed graphitic structure and is composed of graphitic layers with a thickness of ~50 nm, as observed in Figure 2.1f.

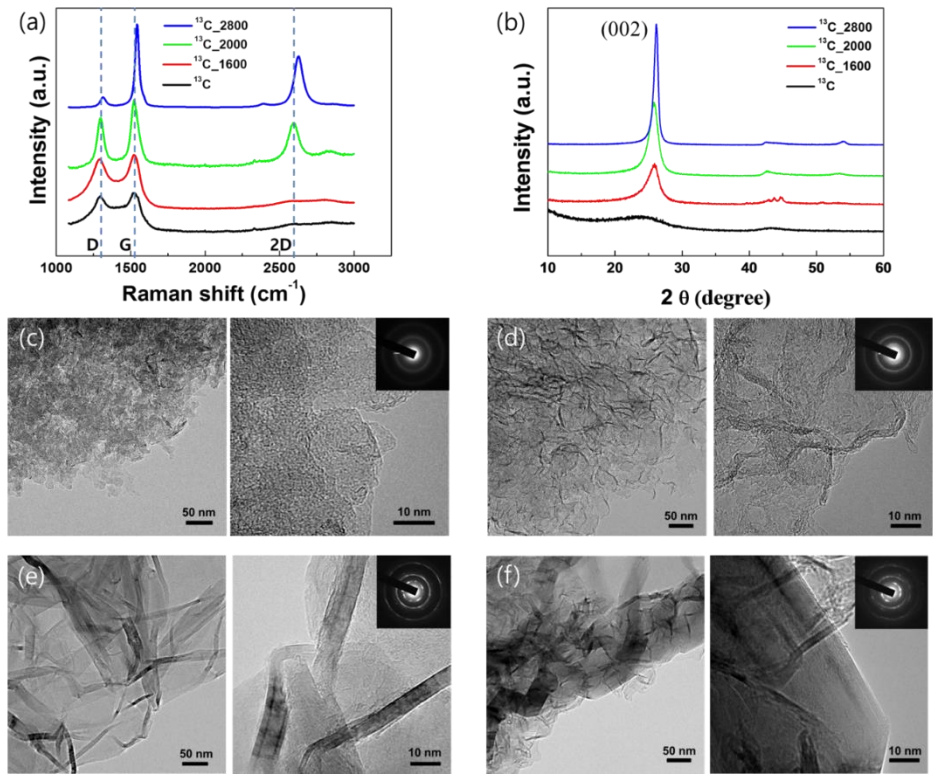

Figure 2.1. (a) Raman spectra and (b) XRD patterns of pristine ^{13}C and heat -treated ^{13}C samples (1600 °C, 2000 °C, 2800 °C). (c–f) FE-TEM images a nd diffraction patterns of pristine ^{13}C and heat treated ^{13}C samples (1600 °C, 2000 °C, 2800 °C).

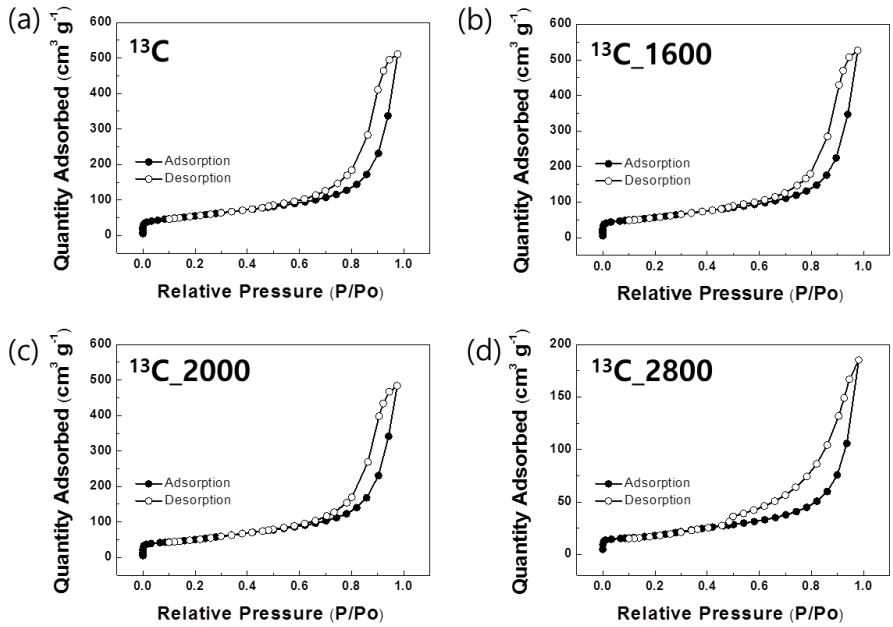

Figure 2.2. N_2 sorption isotherms of (a) ^{13}C, (b) $^{13}C\_1600$, (c) $^{13}C\_2000$, and (d) $^{13}C\_2800$.

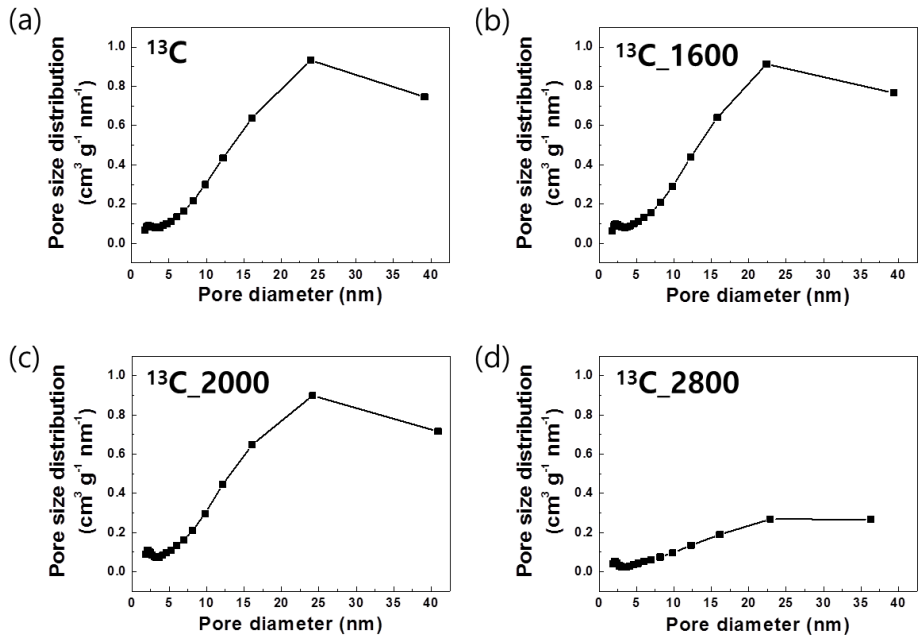

Figure 2.3. Pore size distribution of (a) ^{13}C, (b) ^{13}C_1600, (c) ^{13}C_2000, and (d) ^{13}C_2800.

Table 2.1. Specific information about the textural properties of ^{13}C, $^{13}C\_1600$, $^{13}C\_2000$, and $^{13}C\_2800$.

Sample	S_{BET} (m^2/g)	S_{MIC} (m^2/g)	S_{MESO} (m^2/g)	Pore size (nm)
^{13}C	194.7	6.8	187.9	16.2
$^{13}C\_1600$	201.9	64.9	137.0	16.1
$^{13}C\_2000$	181.1	66.4	114.7	16.5
$^{13}C\_2800$	64.6	34.0	30.6	17.8

Supplementary note 2.1. Analysis for pore structure and specific surface area.

The pore structure and specific surface area of the carbon samples were characterized using a nitrogen adsorption and desorption isotherm method. The isotherm curves of ^{13}C, $^{13}C\_1600$, $^{13}C\_2000$, and $^{13}C\_2800$ are indicative of International Union of Pure and Applied Chemistry (IUPAC) Type IV shapes, indicating that they have a mesoporous structure (Figures 2.2a–d). The pore size distribution data calculated using the Barrett–Joyner–Halender method indicate that all the samples have a broad pore size distribution and that their main pore size is approximately 25 nm (Figures 2.3a–d). The specific surface areas of ^{13}C, $^{13}C\_1600$, and $^{13}C\_2000$ are 194.7, 201.9 and 181.1 $m^2\ g^{-1}$, respectively, which are similar to each other. In contrast, $^{13}C\_2800$ has a much smaller specific surface area of 64.6 $m^2\ g^{-1}$. Table 2.1 presents specific information about the textural properties of all the samples.

Supplementary note 2.2. Contamination of ^{13}C_2800 by graphite furnace.

The *D*, *G*, and 2*D* bands of the ^{13}C_2800 are slightly shifted into high-frequency regions, which may have originated from contamination of the ^{13}C by ^{12}C during the heating process in the graphite furnace. For ^{12}C, the *D* and *G* bands are normally observed at ~1360 and ~1560 cm^{-1}, respectively [*Phys. Rev. B* 64, 075414 (2001)], and it can be shifted by $\sqrt{12/13}$ from the ^{12}C positions due to the larger atomic mass of ^{13}C [J. Appl. Phys. 47, 1971 (2008)]. In the heating temperature above 2000 °C, ^{13}C carbon was thermally transformed into graphitic structure and in this process, fused with considerable ^{12}C carbons consisting of graphite furnace.

2.3.2. Electrochemical properties of Li–O_2 cells with heat treated ^{13}C cathodes

The electrochemical performances were investigated for Li–O_2 cells using air electrodes fabricated with pristine ^{13}C, ^{13}C_1600, and ^{13}C_2000, keeping all the other conditions identical. The capacity was restricted to 0.5 mAh which corresponds to 400 mAh g_c^{-1} and 36% of depth of discharge (Figure 2.4) to avoid the deep discharge which could lead to clogging and high overpotential during charging.[9] 1 M LiTFSI in TEGDME was used as electrolyte in our system, since it is widely used electrolyte system in Li-O_2 batteries,[6-9] and its non-volatile property was important for the prolonged gas analysis in this work. For the DEMS analysis, Ar as a carrier gas flows constantly in the cell during charging, therefore the volatile electrolyte are prone to evaporate after a few cycles. Figures 2.5a and b present the discharge–charge profiles and show the cyclic stability of the Li–O_2 cell using pristine ^{13}C as the air electrode. Initially, a high capacity was retained up to 18 cycles; however, the overpotential between the charge and discharge gradually increased with an increasing number of cycles, which led to the failure of the cell, in agreement with the previous reports (Figure 2.6).[9] The Li–O_2 cell using the ^{13}C_1600 cathode exhibited slightly better cycle retention. Figures 2.5c and d illustrate that the build-up of the overpotential with the number of cycles is slower, and the capacity begins to fade after 25 cycles, suggesting that the change of the carbon crystallinity affects the cyclic stability. This effect is more clearly demonstrated for the ^{13}C_2000 cathode, which exhibited a notably improved cyclic stability. As observed in Figures

2.5e and f, the voltage profiles were nearly unchanged for more than 40 cycles, and only a slight overpotential increase of ~0.2 V was observed until 60 cycles. The overall cycle retention was enhanced by approximately 3 times. Considering that all the other cell conditions were identical and the surface area/pore distributions of the carbon samples were equivalent, this result suggests the strong correlation between the crystallinity of carbon and the cyclic stability. This correlation is also supported by the stable electrochemical performance of the ^{13}C_2800 cathode observed in Figure 2.7. Although the ^{13}C_2800 cell exhibited relatively slow kinetic behavior because of the 3-times-smaller active surface area of the sample, the cycle retention of the ^{13}C_2800 cathode was similar to that of the ^{13}C_2000 cathode. In addition, the increase in the overpotential remained negligibly small up to 60 cycles. Even though heat treated cathode showed better cyclic stability, the capacity rapidly decreased after a certain point, which is commonly observed in the capacity-restricted cycle test.[7, 50-52] The seemingly dramatic degradation of cycles are due to insulating byproducts like Li_2CO_3 which are gradually deposited on the electrode with repetitive cycles. In the Li-O_2 battery system without any catalyst, it is difficult to achieve coulombic efficiency of nearly 100%; hence, the byproducts are inevitably formed on the surface of electrode, inducing an increase of resistivity of Li-O_2 cell. When the cell resistivity reaches a critical point, the overpotential shifts the voltage profile as large as to the cut-off voltages. After this critical point, a further increase in the overpotential even in a slight degree would lead to a large capacity reduction due to the voltage cut-off.

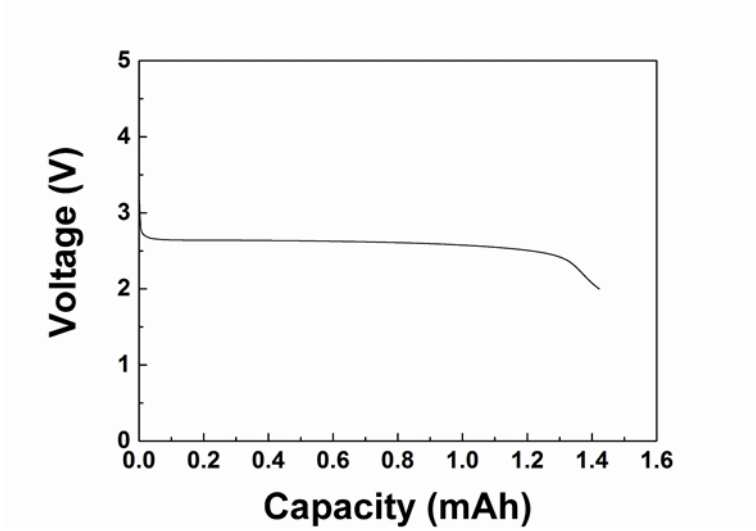

Figure 2.4. Discharge profile of Li–O_2 cell using pristine ^{13}C as the air electrode.

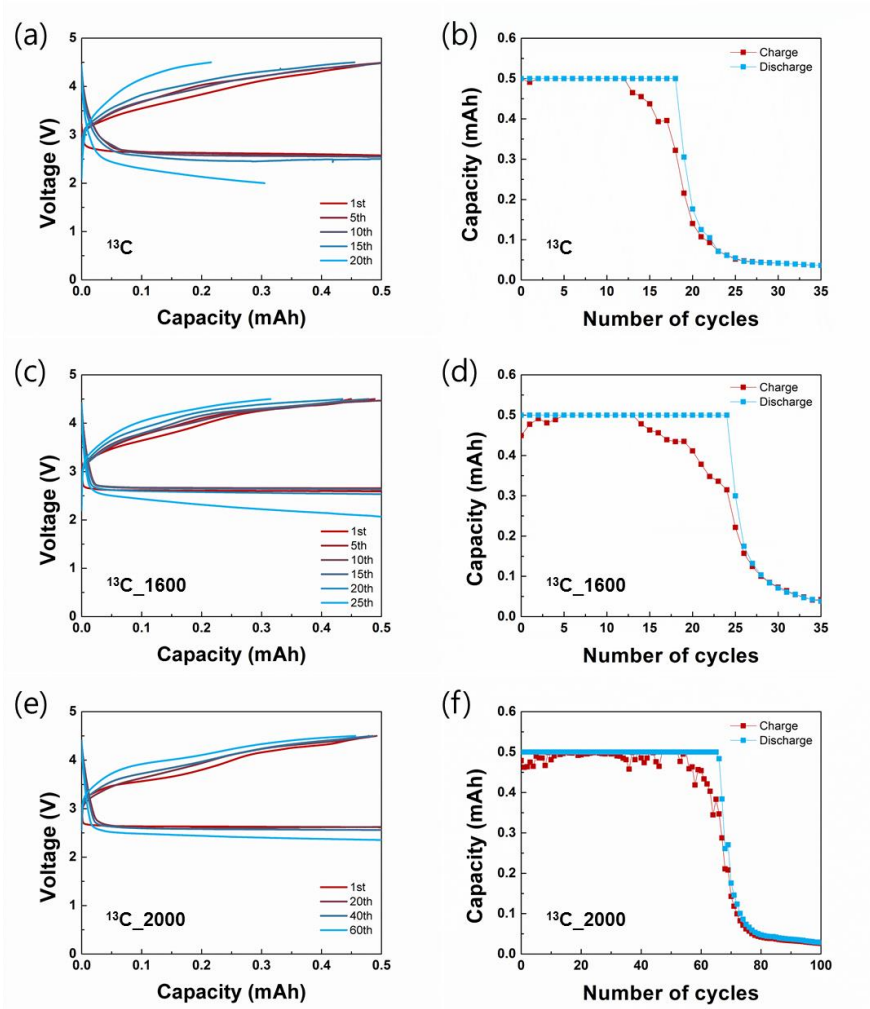

Figure 2.5. Electrochemical performances of Li–O_2 cells with restricted capacity of 0.5 mAh. (a) Discharge–charge profiles of the pristine ^{13}C cathode. (b) Cycle retention using the pristine ^{13}C cathode. (c) Discharge–charge profiles of the ^{13}C_1600 cathode. (d) Cycle retention using the ^{13}C_1600 cathode. (e) Discharge–charge profiles of the ^{13}C_2000 cathode. (f) Cycle retention using the ^{13}C_2000 cathode.

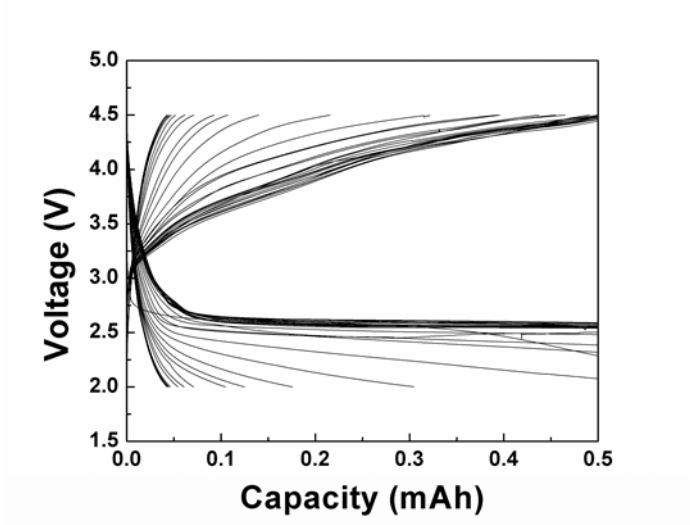

Figure 2.6. Discharge–charge profile of Li–O_2 cell using pristine ^{13}C as the air electrode.

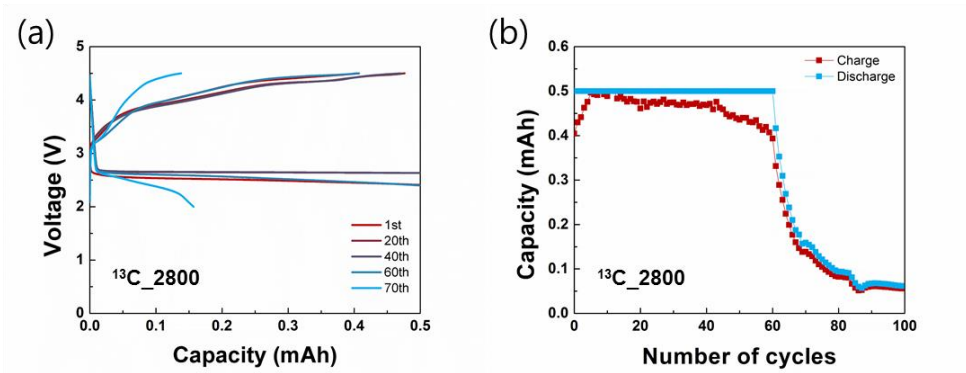

Figure 2.7. Electrochemical performance of Li–O_2 cells. (a) Discharge–charge profiles of the ^{13}C_2800 cathode when the capacity is limited to 0.5 mAh. (b) Cycle retention using the ^{13}C_2800 cathode.

2.3.3. Gas analyses during charge in Li–O_2 cells with heat treated ^{13}C cathode.

To further verify the correlation between the crystallinity of the carbon and the cycle retention, the reactions occurring in each cell were probed using *in situ* DEMS analysis. Figures 2.8a–c present the *in situ* DEMS results during the first charging of the Li–O_2 cells in which ^{13}C, ^{13}C_1600, and ^{13}C_2000 samples were used as the air electrode, respectively. The red, gray, and blue lines represent the evolution of O_2, $^{12}CO_2$, and $^{13}CO_2$ gases, respectively, along the charge voltage profile (purple). The use of isotope ^{13}C carbons in the air cathodes enabled us to discern the origins of the CO_2 evolution, where $^{12}CO_2$ gas originates from electrolyte decomposition and $^{13}CO_2$ gas originates from the side reaction involving the air electrode. The amounts of O_2 evolution were measured to be 3.67, 4.00, and 4.55 μmol for the cells using ^{13}C, ^{13}C_1600, and ^{13}C_2000 cathodes, respectively. Compared with the theoretically expected value of 9.33 μmol, these values are relatively small, indicating the concurrent side reactions occurring from the first cycle, which is commonly observed in typical Li–O_2 cells.[12] However, it should be noted that more oxygen evolution was observed for the more crystalline carbon electrodes, leading to a higher efficiency. Moreover, the overall amount of CO_2 evolution was systematically reduced as the carbon became more crystalline. Figure 2.8d compares the amounts of evolved $^{13}CO_2$ gas for different samples during the first charge on a magnified scale. Notably, the evolution of $^{13}CO_2$ gas was remarkably suppressed for the ^{13}C_2000 cathode (0.03 μmol) compared with that for the pristine ^{13}C (0.51 μmol) or ^{13}C_1600 (0.12 μmol) cathodes. Because $^{13}CO_2$ is solely evolved from the

decomposition of the carbon electrode, it can be deduced that the air cathodes with the high-crystalline carbon were more resistant to the decomposition during the electrochemical reaction in Li–O_2 cells. The higher stability of the crystalline carbon electrode is attributed to the chemical stability of the graphitic carbon, whereas the decomposition of the carbon electrode is likely to occur from the defect sites in the carbon structure. Note that the DEMS profile for O_2 evolution (the red lines in Figure 2.8) always has a double-hill shape resembling an 'M' regardless of the sample.[6, 12] In addition, the beginning point of the CO_2 evolution (grey lines) coincides with the emergence of the second hill in the 'M' shape. We believe that the nature of discharge products can be hinted from the two hills of the oxygen evolution in DEMS experiment. While it has been suggested that Li_2O_2 can be formed by either surface-reaction or solution-process, which results in amorphous like defective Li_2O_2 or crystalline Li_2O_2, respectively, the distinct charge transport properties of the two may result in the two different potentials in the oxygen evolution.[53-55] In previous reports, the ionic and electronic conductivities of crystalline Li_2O_2 were calculated to be ~10^{-19} S/cm,[53] which are relatively low for facile charge conduction. On the other hand, the ionic and electronic conductivities of amorphous Li_2O_2 were calculated to be ~10^{-7} and ~10^{-16} S/cm, respectively.[54] Considering two different nature of Li_2O_2 in transport properties, it is speculated that the amorphous like defective Li_2O_2 that is reportedly formed by the surface-reaction is likely to contribute to the oxygen evolution in the first hill due to the more facile decomposition. Subsequently, more crystalline or segregated Li_2O_2 (most likely from the solution process) would be

decomposed in a higher potential constituting the second hill. For the decomposition of the crystalline Li_2O_2, the surface delithiation process ($Li_2O_2 \rightarrow LiO_2 + Li^+ + e^-$) is expected to occur first,[3] and this reaction does not evolve oxygen, thus may result in the valley between the two hills. More discussion on the shape of the DEMS profile will be continued in the following section.

To understand how the cells degrade with the number of cycles in relation to the side reactions evolving CO_2, we probed the amount of gases as a function of the number of cycles until each cell became electrochemically inactive. Figures 2.9 and 2.10 present the DEMS results for the two representative cells using pristine ^{13}C and ^{13}C_2000 cathodes, respectively. The amounts of evolved $^{13}CO_2$ in the pristine ^{13}C (0.56 μmol) and ^{13}C_2000 (0.03 μmol) cathodes in the first cycle (Figures 2.9a and 2.10a) were similar to those observed in Figures 2.8a and c, respectively, confirming the reliability of our experiments. Figures 2.9b and c show the gas evolutions during the 5^{th} and 10^{th} cycles of the Li–O_2 cell using the pristine ^{13}C cathode. As demonstrated in Figure 2.9b, after 5 cycles, the evolution of $^{13}CO_2$ was significantly increased, whereas the O_2 evolution was notably reduced. Moreover, the O_2 evolution ceased even before the charging process was complete, as indicated by the red line in Figure 2.9b. The charging of the cell over 0.35 mAh capacity only involved the CO_2 gas evolution both from the electrolyte and the carbon electrode. After a few more cycles, *i.e.*, the 10^{th} cycle, as shown in Figure 2.9c, the O_2 evolution ended up faster in the middle of the charging process, which was taken up by the significant CO_2 evolution. Notably, the starting points of both the $^{12}CO_2$ and $^{13}CO_2$

evolution shifted to a much earlier stage of the charge as the cycle continued. When the cell becomes close to electrochemically inactive, the CO_2 evolution begins with the start of the charging. This finding indicates that the degradation of the electrolyte and carbon electrode become more serious with cycling. In addition, it is interesting to note that the 'M' shape of the DEMS profile was almost lost after a certain number of cycles, as observed in Figure 2.9c, and it appears that only the second hill of the 'M' was maintained, where the CO_2 evolution coincided. This finding may imply the gradual change of the main discharge product and the loss of the defective Li_2O_2 discharge product, which is comparatively easy to charge. It is believed that as the surface of the carbon electrode becomes passivated/damaged, the deposition/striping of the defective Li_2O_2 discharge product is significantly prohibited. The amounts of gas evolved at each cycle are summarized in Figure 2.9d. During the cycling, the amount of O_2 evolution decreased and those of $^{12}CO_2$ and $^{13}CO_2$ increased. In particular, the increase in the amount of the evolved $^{13}CO_2$ was more rapid, indicating that the degradation of the carbon electrode becomes more severe than that of the electrolyte for the low-crystalline ^{13}C cathode at extended cycle numbers.

The evolution of gases in the ^{13}C_2000 cathode, however, appears to be markedly different during cycling. Figures 2.10a–e show the gas evolutions during the 1^{st}, 5^{th}, 10^{th}, 15^{th}, and 25^{th} cycles of the Li–O_2 cell using the ^{13}C_2000 cathode. In contrast to the previous case, the evolution of the CO_2 gases was well suppressed overall, and the 'M' shape of O_2 evolution was maintained for more than 20 cycles. Figure 2.10f plots the amounts of gas evolved as a function of cycles for the

^{13}C_2000 cathode and indicates that they did not significantly change with cycling even though the amount of $^{13}CO_2$ slightly increased with cycling. The high-crystalline carbon electrode exhibits a high resistivity to carbon degradation. Nevertheless, the repeated discharge and charge can make the pristine carbon more defective, which results in the carbon becoming more vulnerable to the side reactions and, thus, the increased amounts of evolved $^{13}CO_2$. Note that the amounts of $^{13}CO_2$ were still smaller than the amounts of evolved $^{12}CO_2$ for the ^{13}C_2000 cathode, which indicates that the decomposition of the electrolyte was more dominant in the cyclic degradation than the decomposition of the carbon electrode.

To better compare the ^{13}C and ^{13}C_2000 cathodes, the O_2, $^{12}CO_2$, and $^{13}CO_2$ evolutions during cycling are provided in Figure 2.11. The amounts of evolved $^{13}CO_2$ and $^{12}CO_2$ increased during cycling; however, the increasing rate of $^{13}CO_2$ evolution was significantly slower for the ^{13}C_2000 cathode than the pristine ^{13}C cathode (Figure 2.11a). The amounts of evolved $^{12}CO_2$ from the electrolyte decomposition also increased more rapidly with cycling for the pristine ^{13}C cathode, whereas the ^{13}C_2000 cathode evolved relatively similar amounts of $^{12}CO_2$ gas for each cycle (Figure 2.11b). Although it is generally known that oxygen radicals are generated during the discharge process of Li–O_2 cells and typically degrade the electrolyte,[56] these results indicate that the stability of the electrolyte is sensitively affected by the states of the carbon in the air electrode; in addition, the degradation of the carbon structure also promotes the electrolyte degradation. The damaged surface of the carbon can aggravate the electrolyte stability with cycling, accelerating the

electrolyte decomposition. This finding implies that a well-ordered carbon microstructure of active cathode materials is important in maintaining not only the stability of the air electrode but also that of the electrolyte with cycling. In Figure 2.12, we also plotted the relative ratios of the evolved gases. It confirms that the ratio of $^{13}CO_2$ in the pristine ^{13}C cathode rapidly increased with cycles, whereas the ratio of $^{13}CO_2$ in the ^{13}C_2000 cathode increased tardily. As to the ratio of $^{12}CO_2$, the increasing rate of $^{12}CO_2$ in the pristine ^{13}C cathode was still slightly higher than that of $^{12}CO_2$ in the ^{13}C_2000 cathode, which indicates the tendency of the easier electrolyte decomposition at defect sites of carbon. With regard to the ratio of O_2 in Figure 2.12c, the ratio of O_2 in the pristine ^{13}C cathode rapidly decreased during cycling, while that in the ^{13}C_2000 cathode stayed relatively steady, which is also consistent with the result in Figure 2.11c. FE-SEM images of the cathodes before cycling and after 15 cycles in Figures 2.13a–d confirm the different cyclic stability of the ^{13}C and ^{13}C_2000 cathodes. The pristine ^{13}C and ^{13}C_2000 cathodes initially contained many pores in their structures to accommodate discharge products. After 15 cycles, the pores in the ^{13}C cathode were clogged by remaining discharge products and/or byproducts even after the charging process. In contrast, the pore structure of the ^{13}C_2000 cathode was relatively well maintained after 15 cycles because of the low degradation rate during cycling, as discussed above.

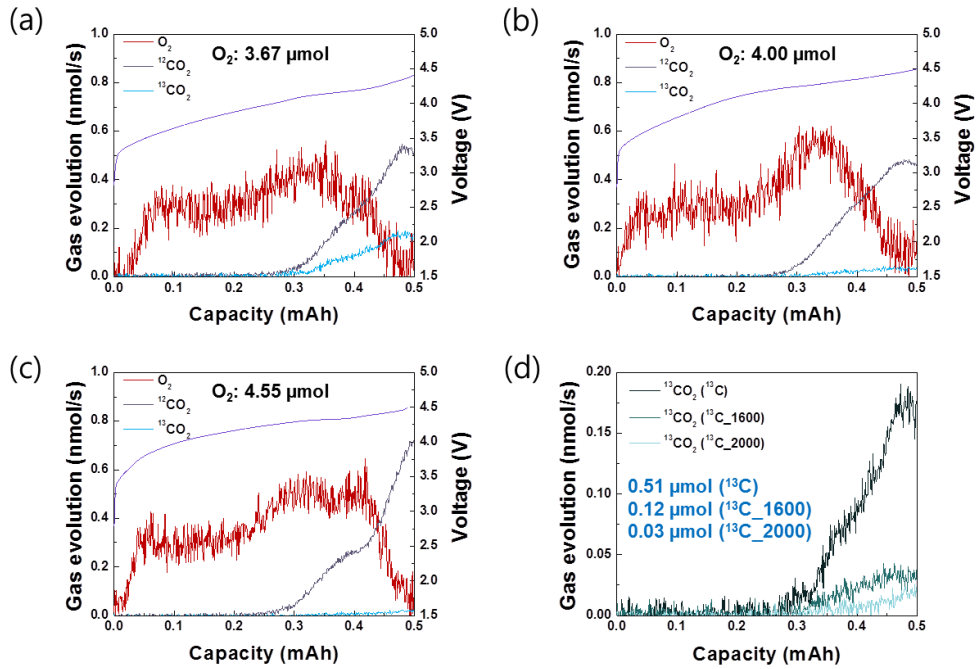

Figure 2.8. *In situ* DEMS analyses during 1st charging at (a) pristine ^{13}C, (b) ^{13}C_1600, and (c) ^{13}C_2000 cathodes. (d) Magnified amounts of evolved $^{13}CO_2$ at pristine ^{13}C, ^{13}C_1600, and ^{13}C_2000 cathodes.

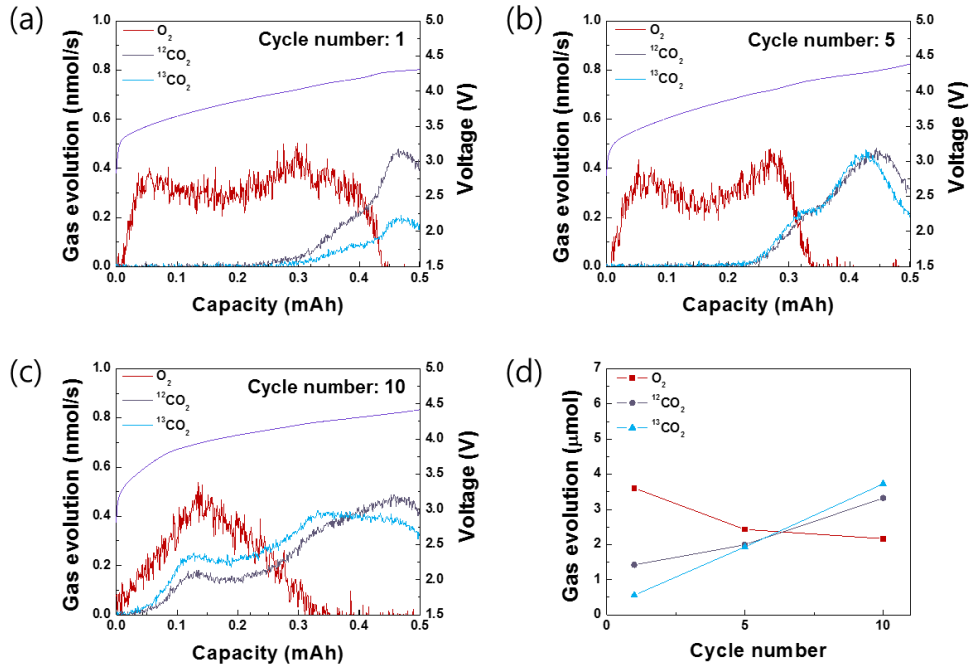

Figure 2.9. *In situ* DEMS analyses at pristine ^{13}C cathode during (a) 1st, (b) 5th, and (c) 10th charging. (d) Summary of the amounts of gas evolution at pristine ^{13}C cathode during cycling.

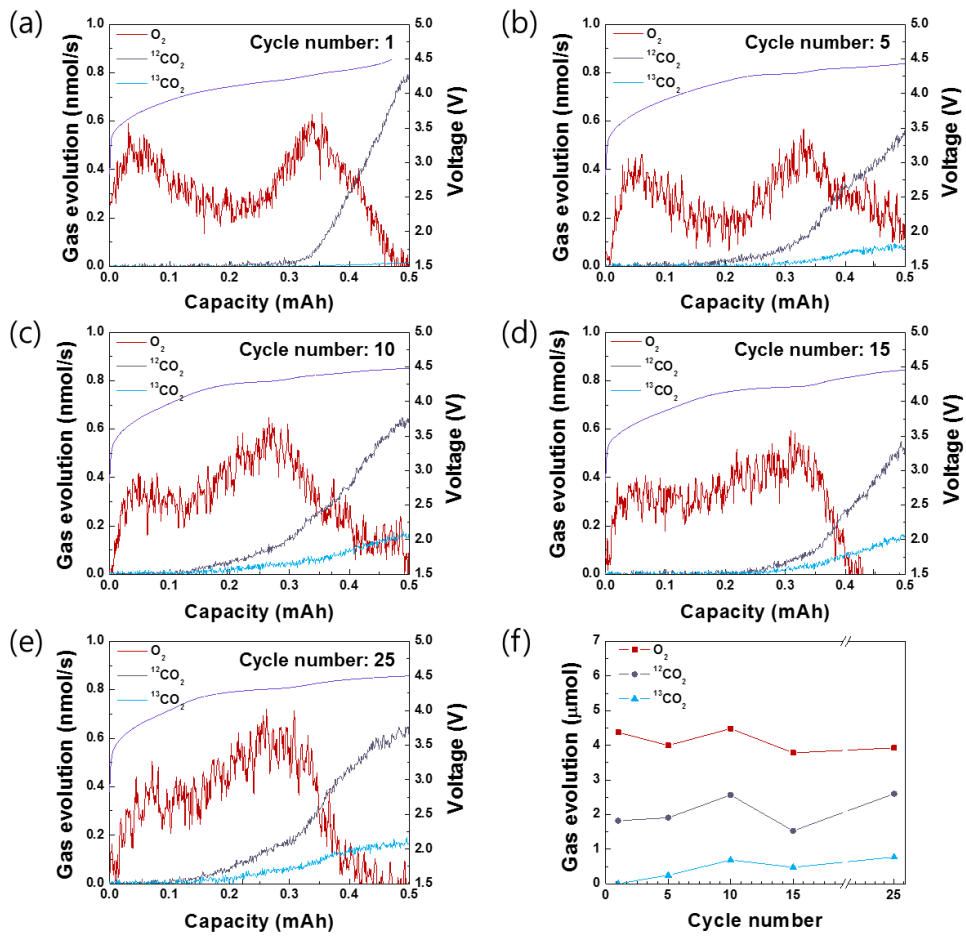

Figure 2.10. *In situ* DEMS analyses at ^{13}C_2000 cathode during (a) 1st, (b) 5th, (c) 10th, (d) 15th, and (e) 25th charge. (f) Summary of the amounts of gas evolution at ^{13}C_2000 cathode during cycling.

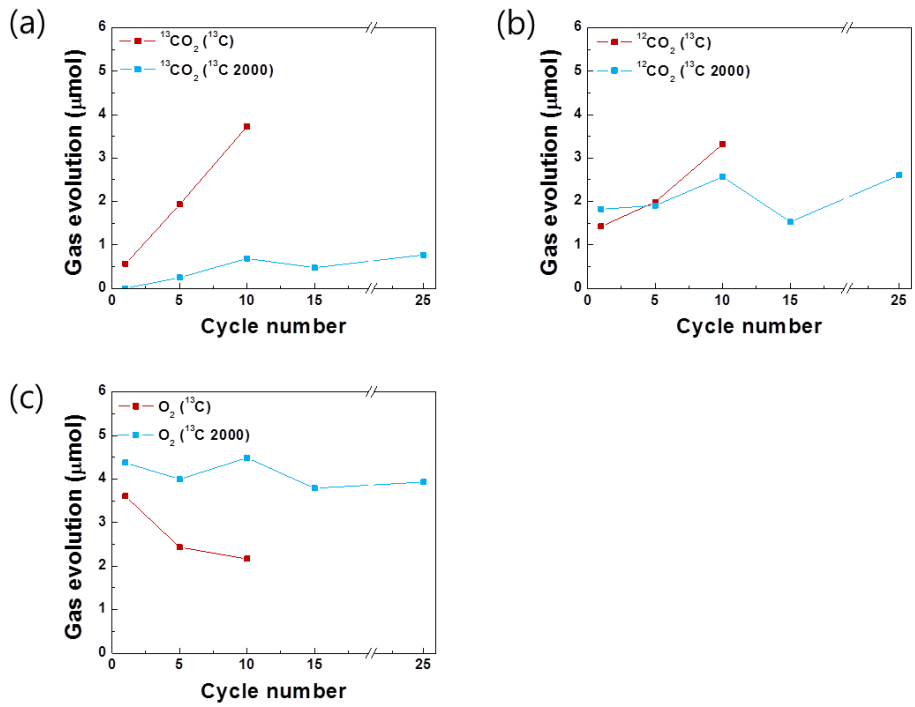

Figure 2.11. Summary of the amounts of (a) $^{13}CO_2$, (b) $^{12}CO_2$, and (c) O_2 evolution during cycling in ^{13}C and ^{13}C_2000.

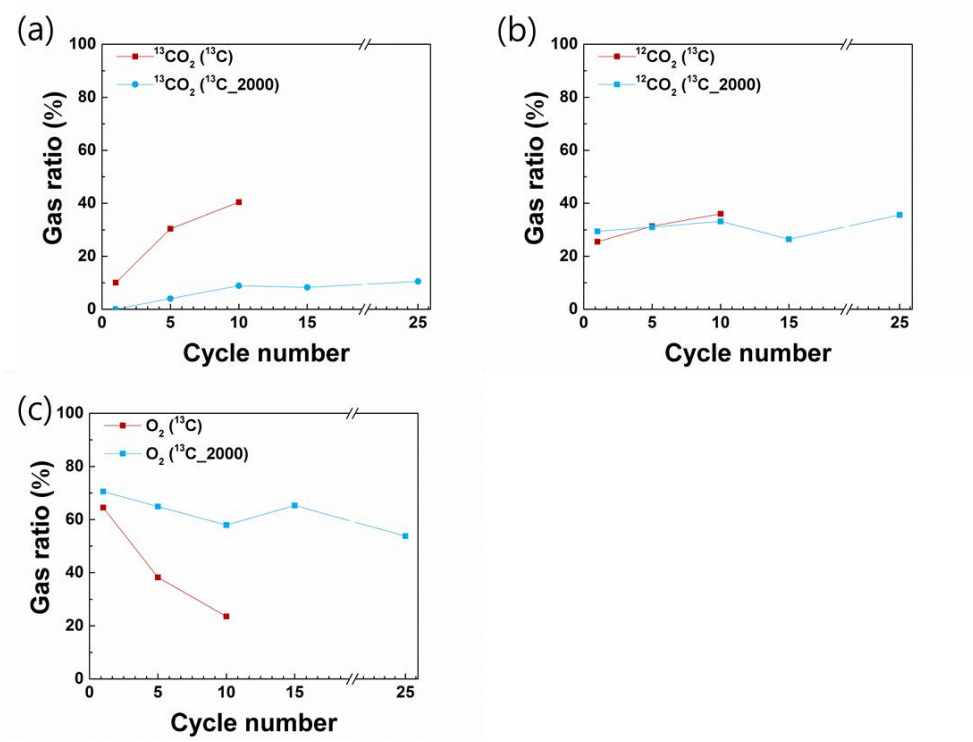

Figure 2.12. Summary of the evolved gas ratio in terms of (a) $^{13}CO_2$, (b) $^{12}CO_2$, and (c) O_2 during cycling in ^{13}C and ^{13}C_2000.

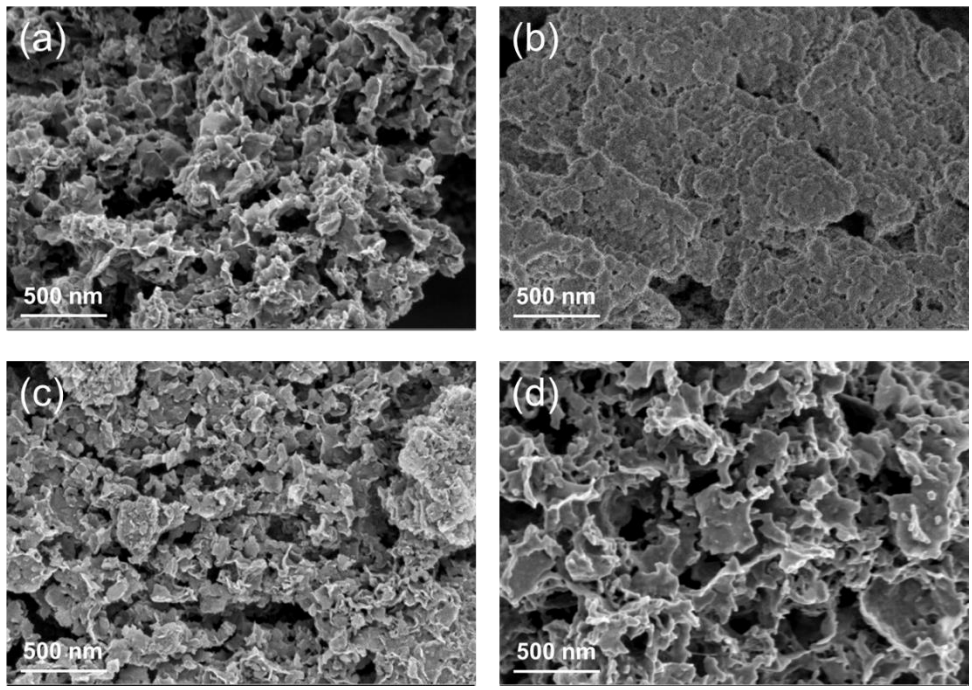

Figure 2.13. FE-SEM images of (a) pristine ^{13}C cathode, (b) ^{13}C cathode after 15 cycles, (c) ^{13}C_2000 cathode, and (d) ^{13}C_2000 cathode after 15 cycles.

2.3.4. Electrochemical properties of Li–O_2 cells with heat treated ^{13}C cathodes containing lithium protective layer and redox mediator.

To demonstrate that our finding on the correlation between the carbon microstructure and the cyclic stability is still valid with the conventional cell optimization process, we optimized the Li-O_2 cells by adopting redox mediator and lithium protective layer. Redox mediators effectively decompose the discharge products during charging, lowering the overpotential and retarding the cycle degradation.[8, 57-59] The application of the CPL on Li metal can stabilize the Li metal anode in the cell and may prevent the possible shuttling of the redox mediator.[60] Figure 2.14 shows the discharge-charge profiles and cyclic stabilities of Li-O_2 cells employing pristine ^{13}C, ^{13}C_1600, and ^{13}C_2000 as the air electrodes. In all cases, the overpotentials had been distinctly reduced during charging and the cyclic stabilities had been remarkably improved. In the case of the pristine ^{13}C cathode, the stable cycle could be maintained up to 46 cycles. Because of the low charging voltage, side reactions associated with the high charging voltage may be alleviated, resulting in about three-fold enhanced cyclic stability compared with the result in Figure 2.5b. In the case of the ^{13}C_1600 cathode, the cycle retention increased to the cycle number of 57 and the overall charge voltages remained slightly lower than those of pristine ^{13}C cathode in Figure 2.14a. These results also indicate that the cyclic stability is influenced by the crystallinity of carbon electrode even in the optimized Li-O_2 cell with the CPL and the redox mediator. The relationship between the cyclic stability and the crystallinity of carbon is more clearly demonstrated in the

^{13}C_2000 cathode as shown in Figure 2.14e, f. The highest capacity retention could be achieved with the ^{13}C_2000 cathode, which was more than 100 cycles. Moreover, the charging profile did not change notably maintaining the low overpotential for more than 100 cycles. In consistent with the above discussions, this result also confirms that the carbon electrode with more ordered graphitic structure leads to less parasitic reactions even in the optimized Li-air batteries.

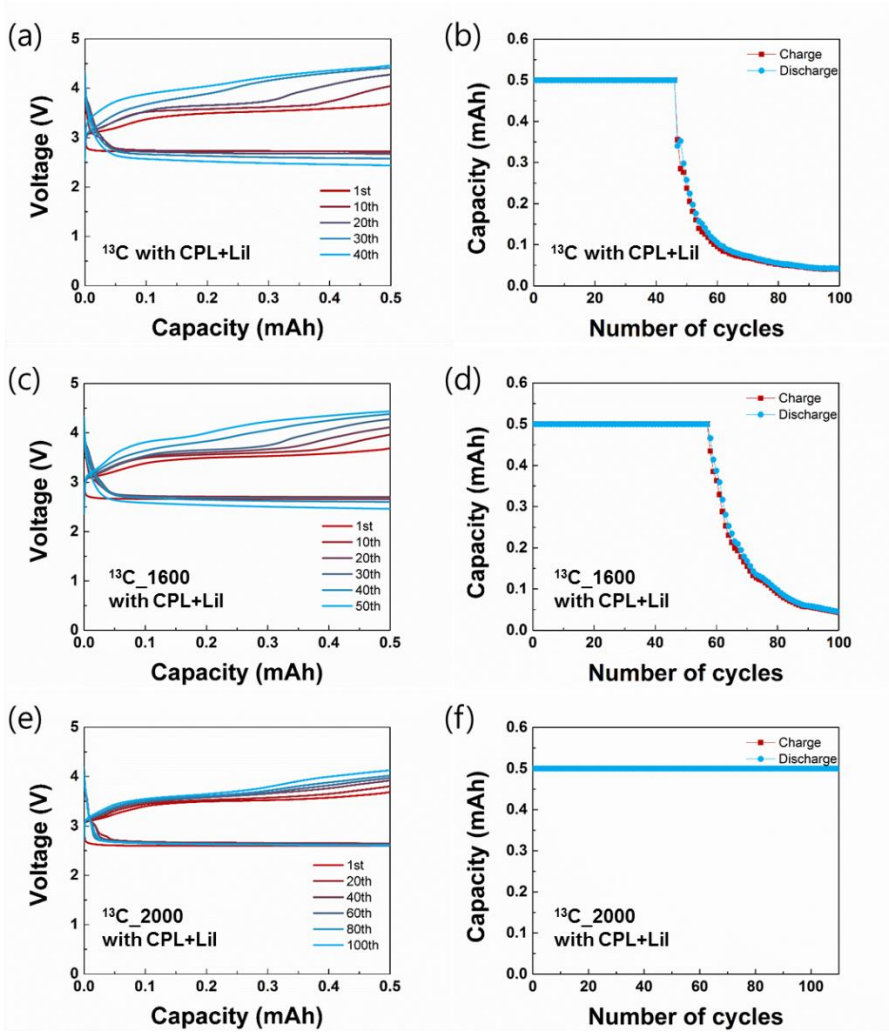

Figure 2.14. Electrochemical performances of Li–O_2 cells with the CPL and the redox mediator. (a) Discharge–charge profiles of the pristine ^{13}C cathode. (b) Cycle retention using the pristine ^{13}C cathode. (c) Discharge–charge profiles of the ^{13}C_1600 cathode. (d) Cycle retention using the ^{13}C_1600 cathode. (e) Discharge–charge profiles of the ^{13}C_2000 cathode. (f) Cycle retention using the ^{13}C_2000 cathode.

2.4 Concluding remarks

The effect of the carbon microstructure on the stability of the air cathode and electrolyte in Li–O_2 batteries was studied using isotope ^{13}C carbon to distinguish side reactions from the electrolyte decomposition and carbon degradation. It was observed that the high-crystalline carbon is capable of delivering superior rechargeability with minimal degradation of the electrolyte and carbon itself compared with the disordered carbon. Comprehensive *in situ* DEMS experiments revealed that when less-crystalline carbon was used for the air electrode, the reversible O_2 reaction was rapidly reduced with cycling along with the degradation of both the electrolyte and carbon electrode. In contrast, the high-crystalline carbon was markedly more resistant to the decomposition, leading to higher cyclic stability, which was attributed to the chemical stability of graphitic carbon. Our findings demonstrate the importance of controlling the carbon microstructure in the air electrode design and suggest a new possibility of using carbon materials as an air electrode for Li–O_2 batteries with long cyclic stability.

2.5 References

[1] K. M. Abraham, Z. Jiang, *J. Electrochem. Soc.* **1996**, 143, 1.

[2] P. G. Bruce, S. A. Freunberger, L. J. Hardwick, J.-M. Tarascon, *Nat. Mater.* **2012**, 11, 19.

[3] Y.-C. Lu, Y. Shao-Horn, *J. Phys, Chem. Lett.* **2012**, 4, 93.

[4] M. M. O. Thotiyl, S. A. Freunberger, Z. Peng, Y. Chen, Z. Liu, P. G. Bruce, *Nat. Mater.* **2013**, 12, 1050.

[5] Z. Peng, S. A. Freunberger, Y. Chen, P. G. Bruce, *Science* **2012**, 337, 563.

[6] D. Kundu, R. Black, E. J. Berg, L. F. Nazar, *Energy Environ. Sci.* **2015**, 8, 1292.

[7] H.-D. Lim, H. Song, H. Gwon, K.-Y. Park, J. Kim, Y. Bae, H. Kim, S.-K. Jung, T. Kim, Y. H. Kim, *Energy Environ. Sci.* **2013**, 6, 3570.

[8] H. D. Lim, H. Song, J. Kim, H. Gwon, Y. Bae, K. Y. Park, J. Hong, H. Kim, T. Kim, Y. H. Kim, *Angew. Chem., Int. Ed.* **2014**, 53, 3926.

[9] H. D. Lim, K. Y. Park, H. Song, E. Y. Jang, H. Gwon, J. Kim, Y. H. Kim, M. D. Lima, R. O. Robles, X. Lepró, *Adv. Mater.* **2013**, 25, 1348.

[10] F. Li, D. M. Tang, T. Zhang, K. Liao, P. He, D. Golberg, A. Yamada, H. Zhou, *Adv. Energy Mater.* **2015**, 5.

[11] H. Kim, H.-D. Lim, J. Kim, K. Kang, *J. Mater. Chem. A* **2014**, 2, 33.

[12] B. D. Adams, R. Black, C. Radtke, Z. Williams, B. L. Mehdi, N. D. Browning, L. F. Nazar, *ACS nano* **2014**, 8, 12483.

[13] H.-G. Jung, Y. S. Jeong, J.-B. Park, Y.-K. Sun, B. Scrosati, Y. J. Lee, *Acs Nano* **2013**, 7, 3532.

[14] J. Xie, X. Yao, Q. Cheng, I. P. Madden, P. Dornath, C. C. Chang, W. Fan, D. Wang, *Angew. Chem.* **2015**, 127, 4373.

[15] E. Yilmaz, C. Yogi, K. Yamanaka, T. Ohta, H. R. Byon, *Nano Lett.* **2013**, 13, 4679.

[16] G. Zhao, R. Mo, B. Wang, L. Zhang, K. Sun, *Chem. Mater.* **2014**, 26, 2551.

[17] A. Débart, A. J. Paterson, J. Bao, P. G. Bruce, *Angew. Chem., Int. Ed.* **2008**, 47, 4521.

[18] A. L. M. Reddy, A. Srivastava, S. R. Gowda, H. Gullapalli, M. Dubey, P. M. Ajayan, *ACS nano* **2010**, 4, 6337.

[19] Y. Li, J. Wang, X. Li, J. Liu, D. Geng, J. Yang, R. Li, X. Sun, *Electrochem. Commun.* **2011**, 13, 668.

[20] Y. S. Yun, G. Yoon, K. Kang, H.-J. Jin, *Carbon* **2014**, 80, 246.

[21] Y. Yun, D.-H. Kim, S. Hong, M. Park, Y. Park, B. Kim, H.-J. Jin, K. Kang, *Nanoscale* **2015**, 7, 15051.

[22] Z. K. Luo, C. S. Liang, F. Wang, Y. H. Xu, J. Chen, D. Liu, H. Y. Sun, H. Yang, X. P. Fan, *Adv. Funct. Mater.* **2014**, 24, 2101.

[23] J. Xiao, D. Mei, X. Li, W. Xu, D. Wang, G. L. Graff, W. D. Bennett, Z. Nie, L. V. Saraf, I. A. Aksay, *Nano Lett.* **2011**, 11, 5071.

[24] Y. Shen, D. Sun, L. Yu, W. Zhang, Y. Shang, H. Tang, J. Wu, A. Cao, Y. Huang, *Carbon* **2013**, 62, 288.

[25] T. Zhang, H. Zhou, *Nat. Commun.* **2013**, 4, 1817.

[26] H. Kitaura, H. Zhou, *Adv. Energy Mater.* **2012**, 2, 889.

[27] H. W. Park, D. U. Lee, M. G. Park, R. Ahmed, M. H. Seo, L. F. Nazar, Z. Chen, *ChemSusChem* **2015**, 8, 1058.

[28] P. Tan, W. Shyy, Z. Wei, L. An, T. Zhao, *Electrochim. Acta* **2014**, 147, 1.

[29] R. Mi, H. Liu, H. Wang, K.-W. Wong, J. Mei, Y. Chen, W.-M. Lau, H. Yan, *Carbon* **2014**, 67, 744.

[30] B. Sun, B. Wang, D. Su, L. Xiao, H. Ahn, G. Wang, *Carbon* **2012**, 50, 727.

[31] C. Sun, F. Li, C. Ma, Y. Wang, Y. Ren, W. Yang, Z. Ma, J. Li, Y. Chen,

Y. Kim, *J. Mater. Chem. A* **2014**, 2, 7188.

[32] Y. S. Jeong, J.-B. Park, H.-G. Jung, J. Kim, X. Luo, J. Lu, L. Curtiss, K. Amine, Y.-K. Sun, B. Scrosati, *Nano Lett.* **2015**, 15, 4261.

[33] X. Ren, J. Zhu, F. Du, J. Liu, W. Zhang, *J. Phys. Chem. C* **2014**, 118, 22412.

[34] M. Christy, H. Jang, K. S. Nahm, *J. Power Sources* **2015**, 288, 451.

[35] G. Wu, N. H. Mack, W. Gao, S. Ma, R. Zhong, J. Han, J. K. Baldwin, P. Zelenay, *Acs Nano* **2012**, 6, 9764.

[36] W.-H. Ryu, T.-H. Yoon, S. H. Song, S. Jeon, Y.-J. Park, I.-D. Kim, *Nano Lett.* **2013**, 13, 4190.

[37] W. B. Luo, S. L. Chou, J. Z. Wang, Y. C. Zhai, H. K. Liu, *small* **2015**, 11, 2817.

[38] L. Wang, M. Ara, K. Wadumesthrige, S. Salley, K. S. Ng, *J. Power Sources* **2013**, 234, 8.

[39] Y. Li, J. Wang, X. Li, D. Geng, M. N. Banis, R. Li, X. Sun, *Electrochem. Commun.* **2012**, 18, 12.

[40] Z. L. Wang, D. Xu, J. J. Xu, L. L. Zhang, X. B. Zhang, *Adv. Funct. Mater.* **2012**, 22, 3699.

[41] H.-G. Jung, J. Hassoun, J.-B. Park, Y.-K. Sun, B. Scrosati, *Nat. Chem.* **2012**, 4, 579.

[42] Y. Li, X. Li, D. Geng, Y. Tang, R. Li, J.-P. Dodelet, M. Lefèvre, X. Sun, *Carbon* **2013**, 64, 170.

[43] D. M. Itkis, D. A. Semenenko, E. Y. Kataev, A. I. Belova, V. S. Neudachina, A. P. Sirotina, M. Hävecker, D. Teschner, A. Knop-Gericke, P. Dudin, *Nano Lett.* **2013**, 13, 4697.

[44] M. M. Ottakam Thotiyl, S. A. Freunberger, Z. Peng, P. G. Bruce, *J. Am. Chem. Soc.* **2012**, 135, 494.

[45] B. McCloskey, A. Speidel, R. Scheffler, D. Miller, V. Viswanathan, J. Hummelshøj, J. Nørskov, A. Luntz, *J. Phys, Chem. Lett.* **2012**, 3, 997.

[46] S. J. Kang, T. Mori, S. Narizuka, W. Wilcke, H.-C. Kim, *Nat. Commun.* **2014**, 5.

[47] B. M. Gallant, R. R. Mitchell, D. G. Kwabi, J. Zhou, L. Zuin, C. V. Thompson, Y. Shao-Horn, *J. Phys. Chem. C* **2012**, 116, 20800.

[48] M. Leskes, A. J. Moore, G. R. Goward, C. P. Grey, *J. Phys. Chem. C* **2013**, 117, 26929.

[49] S. Y. Cho, Y. S. Yun, S. Lee, D. Jang, K.-Y. Park, J. K. Kim, B. H. Kim, K. Kang, D. L. Kaplan, H.-J. Jin, *Nat. Commun.* **2015**, 6, 7145.

[50] F. Li, T. Zhang, Y. Yamada, A. Yamada, H. Zhou, *Adv. Energy Mater.* **2013,** 3, 532.

[51] B. G. Kim, S. Kim, H. Lee, J. W. Choi, *Chem. Mater.* **2014,** 26, 4757.

[52] H. Kim, T. Y. Kim, V. Roev, H. C. Lee, H. J. Kwon, H. Lee, S. Kwon, D. Im, *ACS Appl. Mater. Interfaces* **2016,** 8, 1344.

[53] M. D. Radin, D. J. Siegel, *Energy Environ. Sci.* **2013,** 6, 2370.

[54] F. Tian, M. D. Radin, D. J. Siegel, *Chem. Mater.* **2014,** 26, 2952.

[55] L. Johnson, C. Li, Z. Liu, Y. Chen, S. A. Freunberger, P. C. Ashok, B. B. Praveen, K. Dholakia, J.-M. Tarascon, P. G. Bruce, *Nat. Chem.* **2014,** 6, 1091.

[56] S. A. Freunberger, Y. Chen, N. E. Drewett, L. J. Hardwick, F. Bardé, P. G. Bruce, *Angew. Chem., Int. Ed.* **2011,** 50, 8609.

[57] Y. Chen, S. A. Freunberger, Z. Peng, O. Fontaine, P. G. Bruce, *Nat. Chem.* **2013,** 5, 489.

[58] B. J. Bergner, A. Schürmann, K. Peppler, A. Garsuch, J. R. Janek, *J. Am. Chem. Soc.* **2014,** 136, 15054.

[59] W.-J. Kwak, D. Hirshberg, D. Sharon, M. Afri, A. A. Frimer, H.-G. Jung, D. Aurbach, Y.-K. Sun, *Energy Environ. Sci.* **2016**, 9, 2334.

[60] D. J. Lee, H. Lee, Y. J. Kim, J. K. Park, H. T. Kim, *Adv. Mater.* **2016,** 28, 857.

Chapter 3. Enhanced Stability of Coated Carbon Electrode for Li–O_2 Batteries and Its Limitations

(The essence of this chapter has been published in *Advanced Energy Materials*. Reproduced with permission from [Bae, Y. *et al.*, *Adv. Energy Mater.* **2018**, 8, 1702661] Copyright (2018) WILEY-VCH)

3.1 Research Background

The increasing demands for electric vehicles have spurred a worldwide search for next-generation rechargeable batteries with higher energy density.[1-5] Among various battery systems, the lithium–oxygen (Li–O_2) chemistry offers one of the highest theoretical energy densities, which can reach 3500 Wh kg^{-1} based on the reaction $2Li^+ + O_2 + 2e^- \rightarrow Li_2O_2$ (E^0 = 2.96 V vs. Li/Li^+).[3,6,7] In a typical discharge reaction, oxygen is reduced and reacts with lithium ions to produce lithium peroxide (Li_2O_2), which is mainly deposited on the surface of the air electrode, and the reverse reaction occurs upon charging. The most widely used air electrodes are carbon-based materials because of their large surface areas per weight and high electrical conductivity, which are suitable for promoting the electrochemical formation of Li_2O_2 on the electrode, providing a high gravimetric energy density. For these reasons, carbon-based air electrodes have been intensely researched in recent years,

and various types of carbon materials such as porous carbon, carbon nanotubes (CNTs), and graphene have been reported as air electrodes.[8-18]

Recent studies, however, have shown that parasitic reactions involving carbon-based air electrodes could be one of the factors resulting in the deterioration of the electrochemical cycling of Li–O_2 batteries.[19-22] Upon cycling, carbon can react with Li_2O_2, a discharge product deposited on the carbon electrode, to form insulating Li_2CO_3, which degrades the efficiency and cycle stability.[19,20] Moreover, carbon itself can be corroded under high oxidizing potential in Li–O_2 batteries and can thus be passivated with carbon-containing byproducts.[19,20] The damaged carbon surface aggravates the electrolyte decomposition, resulting in the formation of additional byproducts.[22] These byproducts from the electrolyte and carbon electrode can be partially decomposed during charge and typically lead to the evolution of CO_2 gas instead of O_2. As the cycle continues, insulating byproducts are gradually accumulated, which generally results in a high overpotential, low round-trip efficiency, and short cycle life.[23-25] Even though non-carbon-based air electrodes such as gold, silver, and TiC electrodes have been developed to overcome these issues, their costs and low specific capacities have limited their practical applications.[26-28] Therefore, the design of a strategy to reduce side reactions in the carbon electrode is imperative to achieve high electrochemical stability of Li–O_2 batteries.[29-31]

Our previous work demonstrated that defect sites on carbon materials are more susceptible to reaction with discharge products and are prone to decompose

more easily, serving as seeds for side reactions.[22] Thus, a carbon air electrode with higher crystallinity could exhibit more stable cycle properties. However, the preparation of highly crystalline carbon generally requires high-temperature treatment above 2000°C and substantially reduces the surface area, leading to a relatively small discharge capacity.[22] Moreover, the complete removal of the defects in the production of large-surface carbon materials is not trivial. Instead, appropriate passivation of defect sites for a given carbon material may be a suitable approach to fabricate stable carbon-based air electrodes. Selective growth of materials specifically on the defect sites with the minimal amount of coating would be ideal to prohibit the side reactions without excessively increasing the weight of the air electrode. It was previously reported that Al_2O_3 and Pd could be coated on carbon using atomic layer deposition (ALD) to protect the air electrode and reduce the overpotential, resulting in enhanced cycle stability.[31] Nevertheless, the insulating nature of Al_2O_3 caused a large overpotential during cycling, and the high price of the noble metal remains an issue. Moreover, it is not clearly understood how and to what extent these coating materials can aid in the reduction of the side reactions and whether its effect is maintained with extended cycling.

Herein, we demonstrate that the effect of coating is not limited to the protection of the carbon electrode but also remarkably suppresses the decomposition of the electrolyte. These results were analyzed using *in situ* differential electrochemical mass spectroscopy (DEMS) with labeled isotopic ^{13}C air electrode in the electrolyte composed of ^{12}C for the Li–O_2 cell. During electrochemical charge

and discharge, byproducts from the electrolyte and carbon electrode were simultaneously detected to discern their origin by analyzing the ratio of $^{12}CO_2$ and $^{13}CO_2$ evolution. Moreover, the evolution of these ratios with cycling for coated electrodes was monitored, providing insight into the mechanism by which the coating enhances the cycling. Our findings demonstrate the importance of defect control on the carbon electrode and suggest that effective coating strategies are required for the optimal operation of carbon electrodes in Li–O_2 batteries along with providing further understanding of the growth mechanism of discharge products on the carbon surface.

3.2 Experimental method

3.2.1 Preparation of air electrodes

The active carbon materials composed of ^{13}C (97%) were purchased from Cambridge Isotope Laboratory. The conventional air electrode for the Li–O_2 cell was fabricated using a mixture of the prepared ^{13}C carbon and binder (Kynar 2801) with a weight ratio of 90:10. The mixture was dispersed in N-methyl-2-pyrrolidone (NMP, Sigma-Aldrich, 99.5%) and cast onto a Ni-mesh current collector (1/2 inch diameter). The loading densities of the ^{13}C electrodes were ~1 mg cm^{-2}. The freestanding CNT air electrodes used as a reference were synthesized using the following procedure. First, 40 mg of the CNTs (CM 250, Hanwa Chemical, Korea) was dispersed in 80 mL of deionized (DI) water containing a small amount of poly(4-styrenesulfonic acid) (PSS, M_w = 75,000, 18 wt.% in H_2O, Sigma-Aldrich, USA) and mixed in a sonicator for 1 h. A stable CNT dispersion with a concentration of 0.5 mg mL^{-1} was obtained. The mixture was then sonicated for 10 min and filtered using a polyvinylidene fluoride (PVDF) filter membrane (pore size: 0.45 μm, diameter: 47 mm, Millipore, USA). The filtered films were dried in ambient air for 12 h before being peeled off from the membrane. The CNT papers were then cut into 3/8-inch-diameter fragments for use as freestanding electrodes. The loading densities of the freestanding CNT electrodes were ~0.25 mg cm^{-2}. ALD of ZnO and Al_2O_3 on the carbon electrodes was performed in a laminar flow ALD reactor (CN-1 Co., Ltd., ATOMIC-CLASSIC 2nd edition) consisting of a

chamber, canisters, mass flow controllers, pneumatic valves, a pressure gage, and a pump. The carbon electrodes were loaded on the center of the reactor for 30 min at 150 °C in high-purity N_2 (>99.999 %) flow to reach thermal equilibrium and outgas the carbon electrodes. To measure the thickness of the ZnO and Al_2O_3 coatings on the electrode, a bare Si wafer was loaded concurrently as a reference in the same chamber, and its thickness was measured using a spectroscopic ellipsometer (SE, MG-1000, NanoView). Diethyl zinc (DEZ, Nuritech Co., Ltd.) was employed as the zinc precursor, and water was used as the oxygen precursor to deposit ZnO. For the Al_2O_3 coating, trimethylaluminum (TMA, Nuritech Co.) and water were used as the aluminum and oxygen precursors, respectively. The supplements of each precursor were approximately 1.3×10^{-4}, 4.5×10^{-5}, and 1.3×10^{-3} mol s^{-1} for DEZ, TMA, and water, respectively. All the precursors were vaporized from external canisters at room temperature and led into the chamber. The deposition processes of ZnO and Al_2O_3 consisted of four steps: metal precursor (DEZ or TMA) dosing (0.5 s) – N_2 purge (10 s) – H_2O dosing (1 s) – N_2 purge (10 s). For purging the reactor, N_2 gas was used at a flow rate of 400 sccm. All the delivery lines were maintained at 100 °C. The base pressure of the reactor was less than 10 mTorr, and ALD was performed at a working pressure of 0.2–1.7 Torr. ZnO was deposited on the carbon electrode for 8, 15, and 50 cycles, which correspond to 0.5-, 2.5-, and 10-nm thicknesses of the ZnO film on the Si wafer. These samples were donoted as 8-cyc, 15-cyc, and 50-cyc ZnO/carbon. Ten cycles

of Al_2O_3 correspond to an Al_2O_3 film thickness of 0.5 nm on the Si wafer and it was denoted as 10-cyc Al_2O_3.

3.2.2 Preparation of protected Li metal

The composite protective layer (CPL) on Li metal was fabricated using a simple doctor-blading and roll-pressing method. The CPL slurry was prepared by mixing 0.8 g of 480 nm-sized Al_2O_3 (AES-II, Ishihara Inc., Japan) and 0.2 g of PVdF–HFP in 0.6 g of propylene carbonate (PC) (≥99.7%, Sigma-Aldrich, USA) and 0.9 g of dimethylacetamide (DMAc) (≥99.9%, Sigma-Aldrich, USA) for 24 h. The CPL was coated on a glass plate using a doctor blade (blade thickness = 150 μm; Honzo, Japan) and then dried at room temperature for 1 h in vacuum to evaporate the DMAc. The free-standing CPL was spontaneously detached from the glass substrate, and the PC in the CPL was removed in a DI water bath. Then, the CPL was dried at 60 °C for 2 days in vacuum to completely remove any residual water and subsequently stored in an Ar-filled glove box. The CPL was laminated on a Li metal foil (450 μm) by roll-pressing at room temperature.

3.2.3 Preparation of Li–O_2 cells

Li metal foil (7/16 inch diameter) or CPL-coated Li metal, a glass fiber separator (Whatman GF/F microfiber filter paper, 0.7 μm pore size), the electrolyte, and the prepared air electrodes were stacked in sequence in a Swagelok-type cell. The electrolyte was 1 M LiTFSI in TEGDME, and 0.05 M LiI was added into the electrolyte for the redox mediator test. The electrolyte contain <30 ppm water (determined by Karl Fischer titration). All the cells were assembled in a glove box (H_2O < 0.5 ppm, O_2 < 0.5 ppm) and operated in an O_2 atmosphere (770 Torr). Each cell was relaxed for 1 h in an O_2 atmosphere and operated using the capacity-limited mode of 0.5 mAh (^{13}C electrode) and 1000 mAh g^{-1} (CNT electrode) within the voltage range of 2.0–4.5 V. All the cells were galvanostatically discharged and charged at a current density of 0.1 mA cm^{-2}. A potentio-galvanostat (WBCS 3000, WonA Tech, Korea) was used to measure the electrochemical properties.

3.2.4 Characterization

The morphologies of the samples were examined using scanning electron microscopy (SEM, MERLIN Compact, ZEISS, Germany) and TEM (JEM2100F, JEOL, Japan). The chemical compositions of the air electrodes were probed using XPS (Thermo VG Scientific). The Raman spectra (LabRam HR, Horiba Jobin-Yvon, France) were recorded using a continuous-wave linearly polarized laser (wavelength: 514.5 nm; 2.41 eV; power: 16 mW). *In situ* gas detection spectrometry was carried out to analyze the gases evolving from the Li−O_2 cell, by purging the cell with an Ar carrier gas (10 mL min^{-1}) continuously during charging. Simultaneously, the Ar carrier gas with gaseous products were pumped off to ~10^{-7} Torr with rotary pump and turbomolecular pump sequentially (differential pumping), and then transferred to quadrupole mass spectrometer (MS; HPR-20, Hiden Analytical, U.K.). Before the DEMS experiment, the cells were initially discharged and then connected to the MS being fully relaxed in the Ar flow for 4 h before charging. During charging, electrochemical reaction and concomitant gas evolution from the cell were analyzed concurrently. The MS was calibrated for O_2, CO_2, and Ar with the use of known gas concentrations (2000 ppm O_2, 2000 ppm CO_2/Ar balance) to establish linear relationship between the gas concentration and ion current.

3.3 Results and Discussions

3.3.1 Characterization of ZnO-coated air electrodes

In our study of the effects of coating, ZnO was coated on the carbon electrode using ALD.[32-34] Although ALD method may not be practically feasible for the large-scale process, it was used to coat ZnO on the defect sites of carbon cathode homogeneously to model the cases to alter the state of defect sites in the controlled manner. In order to focus on the effect of coating on the stability of carbon air electrode, coating materials which have shown catalytic effects on the Li–O_2 chemistry such as Pt, Pd, Ru, RuO_2 and Co_3O_4 were ruled out.[13,31,35-37] Since ZnO does not generally exhibit catalytic effect on the reactions of Li–O_2 battery and is relatively conductive, we chose ZnO as a model coating material. Based on the predetermined protocol for coating ZnO on carbon (see Supporting Information), we prepared the ZnO-coated air electrode using isotope ^{13}C. The use of isotope ^{13}C enabled us to distinguish the relative stabilities of the carbon electrode and electrolyte based on the naturally abundant ^{12}C, as will be discussed later. Figure 3.1a and b present transmission electron microscopy (TEM) images of the pristine ^{13}C and ZnO-coated ^{13}C electrodes, respectively. The pristine electrode exhibited the microstructure of amorphous carbon, whereas ZnO was deposited on the surface of ^{13}C in the form of nanoparticles for the ZnO–coated ^{13}C electrode. Figure 3.1c presents the Zn 2*p* X-ray photoelectron spectroscopy (XPS) spectra of the electrodes with increasing number of ALD cycles of ZnO deposition (pristine ^{13}C, 8-cyc

ZnO/^{13}C, and 15-cyc ZnO/^{13}C). With increasing number of ALD cycles, the characteristic ZnO peaks at 1022.4 eV (Zn $2p_{3/2}$) and 1045.4 eV (Zn $2p_{1/2}$) became stronger, indicating more ZnO deposition on the carbon. Notably, the Raman analyses in Figure 3.1d and e reveal systematic changes in the I_D/I_G ratio with increasing ZnO thickness. On the magnified scale in Figure 3.1e, the I_D/I_G ratio decreased as more ZnO was deposited, indicating the reduction of the exposed defective (*i.e.*, non-graphitic disordered) carbon in the structure.[22,38] For the optimal deposition of ZnO on a conventional carbon electrode, a CNT electrode was used as a reference to precisely probe the amount and morphology of ZnO, and similar observations were made for the series of CNT-type electrodes with increasing number of ALD cycles of ZnO deposition, as described in Supporting Information. This finding implies that the ZnO is preferably deposited on defect sites of the carbon surface and effectively shielded the defects in the structure.

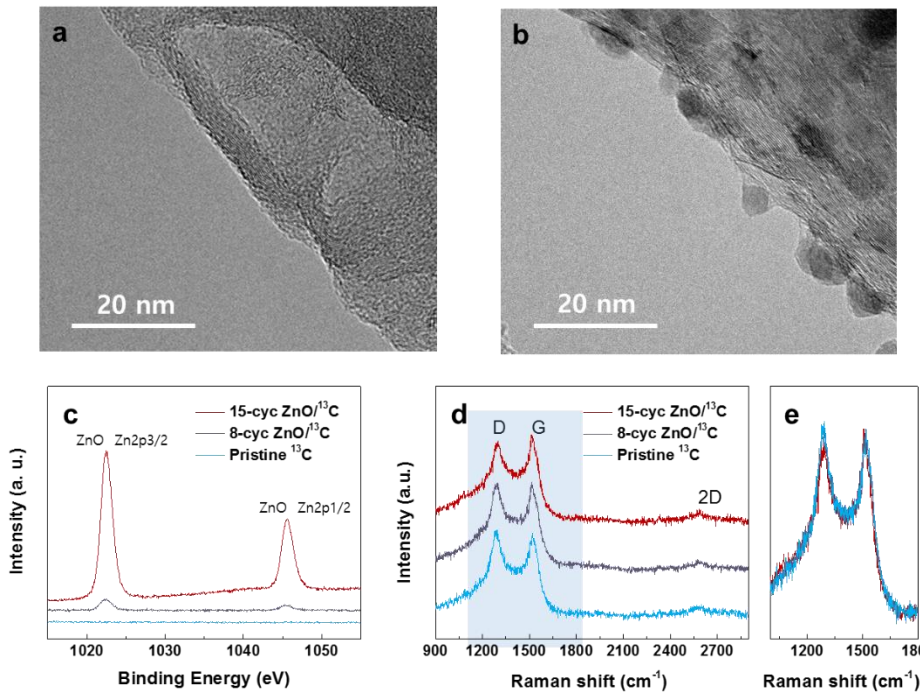

Figure 3.1. TEM images of (a) pristine ^{13}C and (b) ZnO-coated ^{13}C. (c) XPS and (d, e) Raman spectra of pristine ^{13}C, 8-cyc ZnO/^{13}C, and 15-cyc ZnO/^{13}C.

Supplementary note 3.1. Electrochemical properties of Li–O_2 cells using coated CNTs and determination of coating protocol

To verify the effect of ZnO on the stability of the Li–O_2 cell and for comparison with the insulating Al_2O_3 coating, Li–O_2 cells were tested for 5 cycles using pristine CNT, 8-cyc ZnO/CNT, and 10-cyc Al_2O_3/CNT as the air electrodes (Figure 3.2). For the electrolyte, 1 M LiTFSI in TEGDME was used because it has relatively high stability and non-volatility. The discharge capacity of the Li–O_2 cell using the pristine CNT decreased to 32% of the initial capacity after 5 cycles, whereas the Li–O_2 cell using 8-cyc ZnO/CNT maintained a stable discharge–charge profile, implying that the defect shielding effect of ZnO leads to improved stability of the cell. In contrast, the Li–O_2 cell using 10-cyc Al_2O_3/CNT exhibited a negligible initial discharge capacity because of the high resistivity of Al_2O_3, demonstrating the importance of the low resistivity of coating materials and the suitability of ZnO as a protective material for carbon cathodes in the Li–O_2 cell. To investigate the thickness effect of ZnO on the cell performance, 15-cyc ZnO/CNT and 50-cyc ZnO/CNT were used as air electrodes for a Li–O_2 cell test (Figure 3.3). For the cell using 15-cyc ZnO/CNT, the initial discharge capacity was reduced by 30%, and negligible discharge capacity was observed for the cell using 50-cyc ZnO/CNT. Although ZnO is ~10^{18} times more conductive than Al_2O_3, it is still less conductive than carbon materials; therefore, too much ZnO coating results in a high resistivity of the carbon cathode.[1] SEM images of the pristine CNT, 8-cyc ZnO/CNT, and 50-cyc ZnO/CNT are presented in Figure 3.4. The 8-cyc ZnO/CNT has almost the same morphology

as that of the pristine CNT, whereas the 50-cyc ZnO/CNT was distinctly covered by coating material, clogging the porous structure of the CNTs. For these reasons, 8-cyc ZnO coating prepared using the ALD method was used in this study to shield the defect sites of carbon to maintain the conductive property, low weight, and porous structure of the carbon cathode.

[1] *J. Electrochem. Soc.* **2003**, 150, G339.

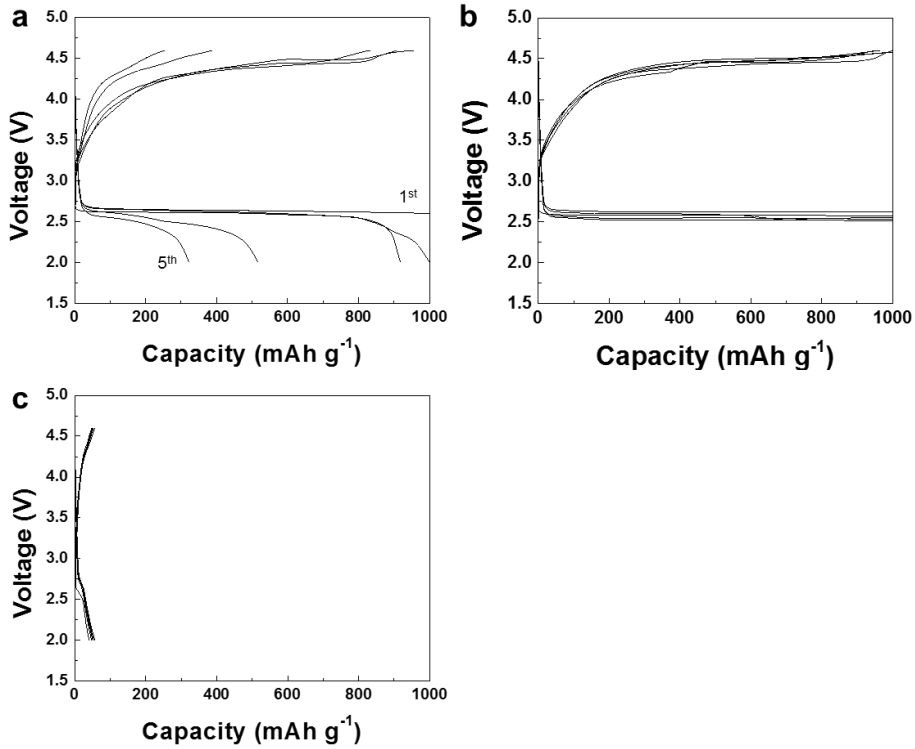

Figure 3.2. Discharge–charge profiles of Li–O_2 cells with (a) pristine CNT, (b) 8-cyc ZnO/CNT, and (c) 10-cyc Al_2O_3/CNT cathodes.

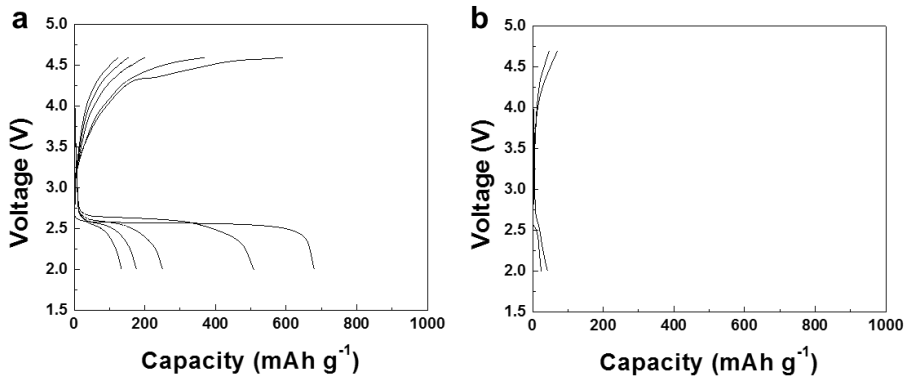

Figure 3.3. Discharge–charge profiles of Li–O_2 cells with (a) 15-cyc ZnO/CNT and (b) 50-cyc ZnO/CNT cathodes.

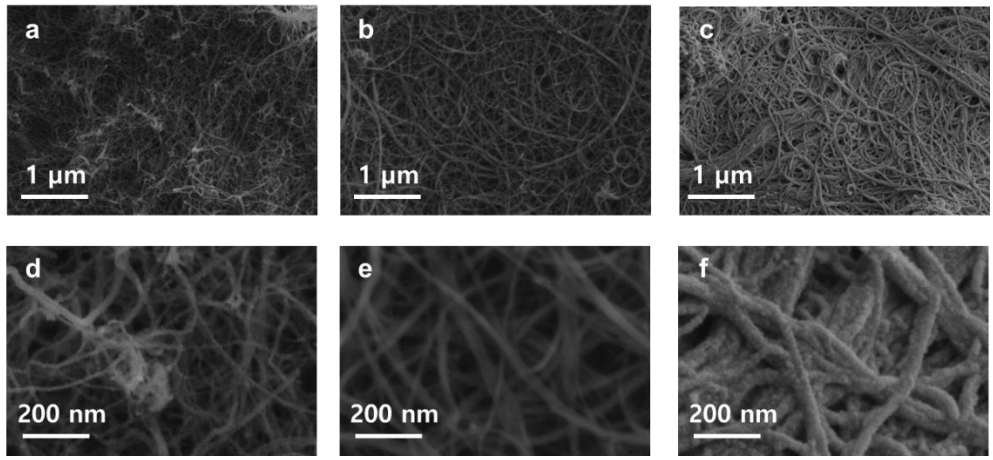

Figure 3.4. SEM images of (a,d) pristine CNT, (b,e) 8-cyc ZnO/CNT, and (c,f) 50-cyc ZnO/CNT.

Supplementary note 3.2. Characterization of ZnO-coated CNTs

Figure 3.5a,b presents TEM images of the as-prepared CNTs and CNTs coated with ZnO using ALD. The as-prepared CNTs have a one-dimensional morphology consisting of several layers of walls and internal voids (Figure 3.5a). Figure 3.5b shows that ZnO was deposited on the CNTs after the ALD process in the form of nanoparticles rather than as a film. Figure 3.5c presents Zn 2p XPS spectra of the CNTs with increasing numbers of ALD cycles of ZnO (pristine CNT, 8-cyc ZnO/CNT and 15-cyc ZnO/CNT). With increasing number of ALD cycles, the ZnO peaks at 1022.4 eV (Zn $2p_{3/2}$) and 1045.4 eV (Zn $2p_{1/2}$) increased, indicating that the nanoparticles deposited on the CNTs were ZnO. The TEM–energy-dispersive X-ray spectroscopy (EDS) analyses of the ZnO deposited CNT bundles in Figure 3.6 reveal that ZnO nanoparticles were uniformly dispersed on the surface of the CNTs. The amount of Zn was approximately 0.8 at% on 95.7 at% of carbon for the 15-cyc ZnO/CNT sample (the remaining 3.5 at% corresponded to oxygen), which resulted in a relatively small increase (~15%) of the electrode weight. The three samples were also subjected to Raman analyses to determine whether ZnO deposition results in a shielding effect of the carbon defects (Figure 3.5d,e). The D and G bands in the Raman spectra correspond to disorder in the A_{1g} breathing mode of the aromatic ring and the E_{2g} vibration mode of the hexagon structure, respectively. Therefore, the I_D/I_G ratio can be an indicator of the degree of defectiveness in the carbon structure. On the magnified scale in Figure 3.5e, a systematic decrease of the I_D/I_G ratios was observed with increasing amount of deposited ZnO, which demonstrates that the

deposited ZnO nanoparticles effectively shield the defect sites of carbon. The numerical values of the I_D/I_G ratios for each sample are listed in Table 3.1.

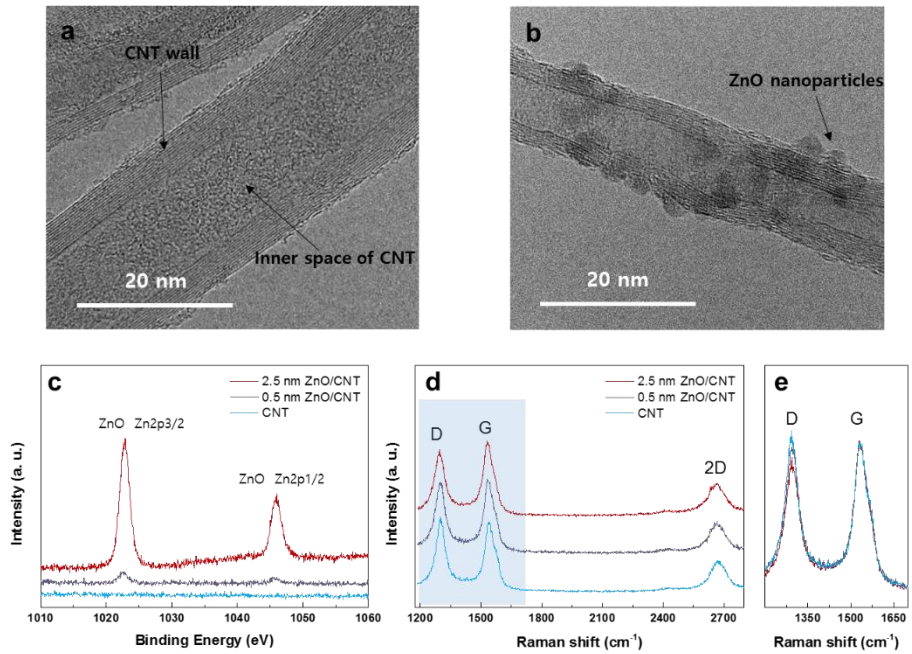

Figure 3.5. TEM images of (a) pristine CNT and (b) ZnO-coated CNT. (c) XPS and (d, e) Raman spectra of CNT, 8-cyc ZnO/CNT, and 15-cyc ZnO/CNT.

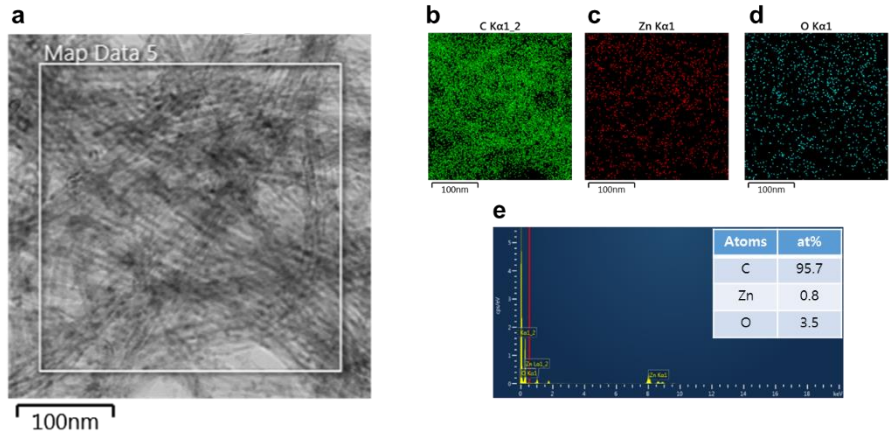

Figure 3.6. (a) EDS mapping region in TEM images of the ZnO-coated CNT. (b–d) EDS mapping (C, Zn, and O elements) of the ZnO-coated CNT. (e) EDS spectrum of the ZnO-coated CNT.

Table 3.1. I_D/I_G ratios of CNT, 8-cyc ZnO/CNT, and 15-cyc ZnO/CNT.

Samples	I_D/I_G
CNT	1.07
8-cyc ZnO/CNT	0.96
15-cyc ZnO/CNT	0.89

3.3.2 Electrochemical properties of Li–O_2 cells using ^{13}C and ZnO-coated ^{13}C cathodes with redox mediator and CPL

To verify the effect of ZnO coating, two Li–O_2 cells were assembled using ^{13}C air electrodes with and without the ZnO coating, as shown in Figure 3.7. The assembled Li–O_2 cells were composed of the respective carbon air electrodes, a protected Li metal anode, and tetraethylene glycol dimethylether (TEGDME) dissolved with 1 M lithium bis(trifluoromethane)sulfonimide (LiTFSI) and 0.05 M LiI as the electrolyte containing redox mediator.[12,39-41] (The detailed cell configuration is provided in the experimental section.) Figure 3.7a and b display the discharge–charge profiles and cycle stability of the Li–O_2 cell with the pristine ^{13}C air electrode, respectively, compared with those of the ZnO-coated electrode (Figure 3.7c and d). The use of the redox mediator and protected Li metal aided in reducing the polarization and enhancing the cycle efficiency of the cell compared with conventional Li–O_2 cells.[41] Nevertheless, it is noteworthy that the ZnO-coated air electrode further improved the cycle stability with relatively smaller overpotentials being maintained throughout the cycles. For the pristine electrode in Figure 3.7a and b, the charging overpotential gradually increased, leading to rapid cycle degradation after 40 cycles. The increase in the overpotential is typically related to the accumulation of insulating byproducts, which originate from parasitic reactions in the electrolyte or at the carbon electrode.[19,20,22] However, the ZnO-coated electrode delivered a remarkably enhanced cycle stability over 100 cycles and small charging

overpotentials, as observed in Figure 3.7c and d, which strongly supports the efficacy of ZnO coating on the carbon electrode. Although LiI containing Li–O_2 cell with ZnO coated cathode showed stable cycle retention, issues related to side reactions involving LiI should be considered including the formation of LiOH due to H-abstraction of solvent molecules or residual water.[42,43] This phenomenon was known to be severe at high concentration of LiI or water. Nevertheless, in our case, we used 1 M LiTFSI + 0.05 M LiI in TEGDME which contains under 30 ppm H_2O for the cell test, and this low concentration of LiI and H_2O resulted in relatively less side reactions. Also, there were several reports that confirmed enhanced cycle stability using 0.05 M LiI as a redox mediator recently.[44-46]

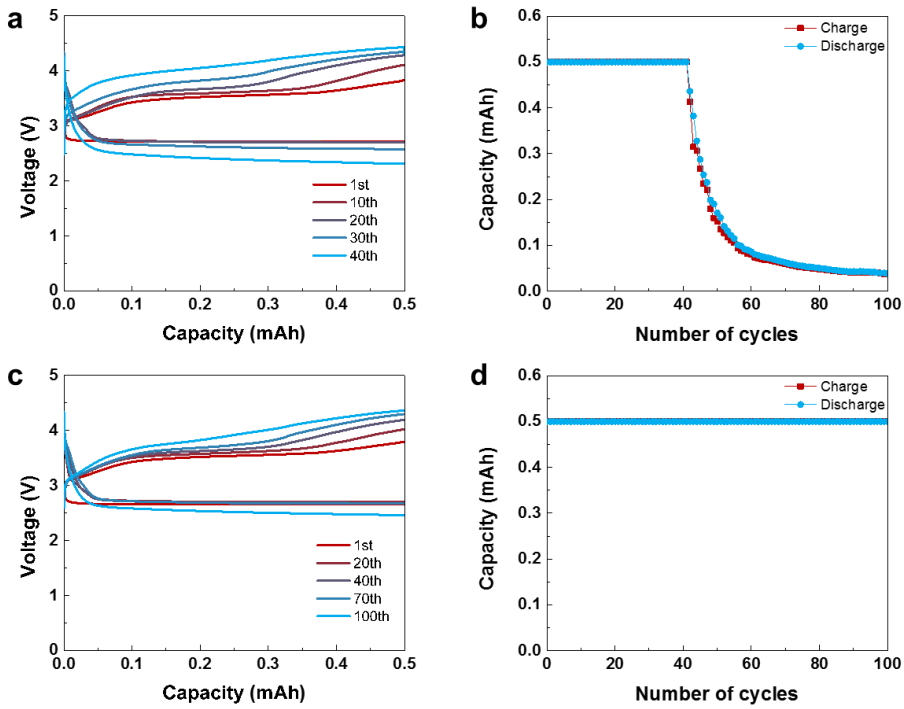

Figure 3.7. Discharge–charge profiles of Li–O_2 cells with the LiI redox mediator and CPL-protected Li metal using (a) pristine ^{13}C and (c) ZnO-coated ^{13}C as the air electrodes at a current rate of 0.1 mA/cm^2. Cycle stability of each Li–O_2 cell using the (b) pristine ^{13}C and (d) ZnO-coated ^{13}C as the air electrodes.

Supplementary note 3.3. Electrochemical properties of Li–O_2 cells using ^{13}C and ZnO-coated ^{13}C cathodes without redox mediator and CPL

Figure 3.8a,b present the discharge–charge profile and current cycle stability of the Li–O_2 cell with pristine ^{13}C as the air electrode. Similar to the results in our previous report, the initial charge capacity was well maintained up to 10 cycles; however, the overpotential gradually increased during cycling, resulting in cell failure.[2] As shown in Figure 3.8c,d, the Li–O_2 cell with ZnO-coated ^{13}C as the air electrode retained its charge capacity up to 31 cycles and the overpotentials during cycling were almost constant. The ZnO coating on the carbon improved the cycle life by a factor of approximately three, confirming that ZnO, which protects carbon defect sites from contact with discharge products, byproducts, and electrolytes, positively affects the stability of Li–O_2 batteries. In these cell tests, the capacity was limited to 0.5 mAh (~400 mAh g^{-1}, ~40% of the depth of discharge) to avoid deep discharge, which results in high resistivity of the cathode. For the DEMS analyses in next chapter, the cell configuration in Figure 3.8, which does not contain the CPL or redox mediator, was adapted to focus on the effect of ZnO on the degradation of carbon materials and electrolytes.

[2] *Chem. Mater.* **2016**, 28, 8160.

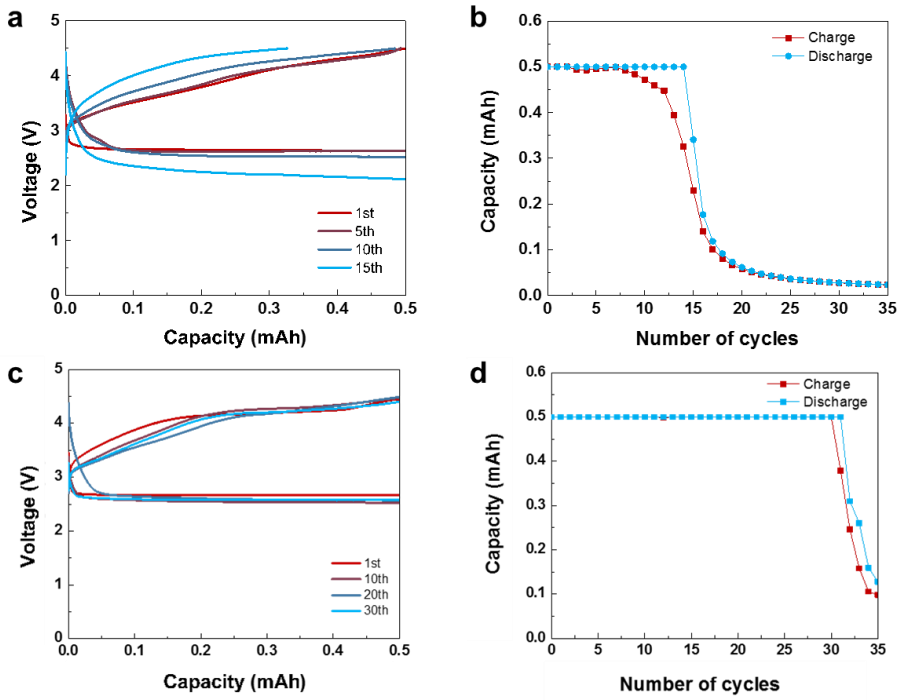

Figure 3.8. Discharge–charge profiles of Li–O_2 cells with the (a) pristine ^{13}C cathode and (c) ZnO-coated ^{13}C cathode. Cyclability of Li–O_2 cells with the (b) pristine ^{13}C cathode and (d) ZnO-coated ^{13}C cathode.

3.3.3 Gas analyses during charge in Li–O_2 cells with ^{13}C and ZnO-coated ^{13}C cathodes

To elucidate the enhancement of the Li–O_2 cell performance with the coating, the reactions occurring in each Li–O_2 cell were scrutinized using *in situ* DEMS during the charge to monitor the evolution of the gas species, as shown in Figure 3.9. DEMS analyses were also performed with the number of cycles to probe the evolution of the parasitic reactions of the electrolyte and carbon electrode with time/cycling and to determine the extent to which each side reaction was responsible for the deterioration of the cell. Additional information on the *in situ* DEMS setup and cell conditions is provided in the Supporting Information. Figure 3.9 presents the gas analysis results for the first ten cycles of the pristine ^{13}C air electrode, where the evolutions of O_2, $^{12}CO_2$, and $^{13}CO_2$ gases are shown in red, gray, and blue, respectively, along with the voltage profile in purple. During the first charging process, as shown in Figure 3.9a, the evolution of oxygen was relatively constant with the typical "M" shape, which is consistent with previous reports.[22,47-51] The shape of the oxygen evolution curve has been reported to generally hint at the types of the discharge products formed with respect to the crystallinity/stoichiometry or morphology of Li_2O_2.[22,47-51] Based on the previous studies, we speculate that the oxygen evolution in the first hill of the "M" profile is attributed to the non-stoichiometric $Li_{2-x}O_2$ film on the electrode, which can be easily decomposed, whereas the oxygen evolution from the second hill originates from the more

crystalline or segregated Li_2O_2 (most likely from the solution process), which would involve a slightly higher overpotential during charging.[52,53] In the Supporting Information, we provide the additional discussions on the origin of the "M" shape, taking account of other possible side reactions such as carbon corrosion and the presence of singlet oxygen.[19-22,54,55]

The amount of evolved oxygen during first charging was 3.87 μmol, which is far smaller than the theoretically expected value of 9.33 μmol, indicating the occurrence of serious side reactions even in the first cycle, which is common in Li–O_2 batteries.[56] $^{12}CO_2$ and $^{13}CO_2$ started to evolve when the charging voltage was approximately 4 V (*vs.* Li/Li^+), and their evolution gradually increased until the end of charging. Moreover, the Li–O_2 cell with the pristine ^{13}C electrode exhibited a significant increase in the amount of evolved CO_2 gases with the number of cycles, which agrees with previous reports.[19,22,50] The CO_2 evolution not only indicates the instability of the electrolyte and the carbon cathode but also promotes carbonate formation deteriorating the cell more severely.[57,58] During the fifth charge, the amount of evolved oxygen was reduced to 2.43 μmol, and the point at which $^{12}CO_2$ and $^{13}CO_2$ started to evolve shifted to the beginning of the charging region, resulting in a larger amount of evolved $^{12}CO_2$ and $^{13}CO_2$ (Figure 3.9b). These phenomena became more severe during the tenth charge; the oxygen evolution was reduced to 1.82 μmol, and the "M" shape transformed into a single-hill shape along with the evolution of $^{12}CO_2$ and $^{13}CO_2$ upon starting the charging process (Figure 3.9c). Figure 3.9d quantitatively compares the relative ratios of the evolved gases with

cycling, with the share of oxygen in the entire gas evolution being significantly reduced from 68% to 20% over ten cycles, accompanied by the rapid cycle degradation of the Li–O_2 cell using the pristine ^{13}C air electrode.

The gas analyses for the ZnO-coated electrodes during cycling, however, were quite dissimilar. Figure 3.10a–d show the evolution of the gases during the first, fifth, tenth, and fifteenth charge processes from Li–O_2 cells using coated ^{13}C air electrodes. Compared with the pristine electrode, the starting point of the CO_2 evolution at charge in Figure 3.10a is significantly retarded (> 4.2 V *vs.* Li/Li^+), and the total amounts of CO_2 are also noticeably reduced, whereas the extent of the oxygen evolution is correspondingly higher. More importantly, both $^{12}CO_2$ and $^{13}CO_2$ evolution were substantially suppressed, indicating that the ZnO coating subdues the degradation of both the electrolyte and carbon electrode. Considering that the coating could effectively shield the defects in the carbon structure, as illustrated in Figure 3.1d, this finding support the assumption that the damaged carbon surface in typical Li–O_2 cells aggravates decomposition of the electrolyte. Notably, the second hill of the oxygen "M" shape increased and the voltage plateau around ~4.2 V was more pronounced with ZnO coating compared with the pristine ^{13}C cathode in Figure 3.9a. This result may indicate that the ZnO coating reduces the formation of $Li_{2-x}O_2$ on the electrode surface, whereas crystalline Li_2O_2, which is charged at a relatively higher voltage, is formed in larger quantities. This phenomenon was more dominantly observed with thicker ZnO coating as shown in Figure 3.11. For the cells with larger amounts of ZnO coating, the reduction of the first hill and increase of the

second hill in the “M” shape were more noticeably observed. Furthermore, as the thickness of the ZnO coating increased, the plateau at ~4.2 V became longer in the charging profile. Compared with the pristine ^{13}C electrode for the fifth charge, the coated electrode exhibited more oxygen evolution and greatly reduced amounts of $^{12}CO_2$ and $^{13}CO_2$, as observed in Figure 3.10b, although the CO_2 evolution slightly increased compared with that during the first charge. In addition, the first hill of the “M” shape of the oxygen evolution rose and the second hill was reduced along with shortening of the 4.2-V plateau, whose origin will be discussed later with respect to the stability of ZnO on the carbon surface. In the subsequent tenth and fifteenth charges in Figure 3.10c and d, no further significant deterioration of the electrolyte or carbon electrode was observed, and the oxygen evolution profile remained roughly the same. The total amounts of each gas for the ZnO-coated electrode are plotted as a function of cycle number in Figure 3.10e, revealing no dramatic increase in the CO_2 evolution after five cycles. This finding is in clear contrast to the case of the pristine carbon electrode, as comparatively illustrated in Figure 3.10f–h for the $^{12}CO_2$, $^{13}CO_2$, and O_2 evolutions, respectively, for each air electrode. The total amount of CO_2 evolution in the coated electrode remained approximately the same with a marginal rise or fall, whereas that in the pristine electrode showed rapid growth with cycling, and, in particular, the evolution of $^{13}CO_2$ gas became more dominant for the later cycles. Interestingly, both the $^{12}CO_2$ and $^{13}CO_2$ evolutions showed similar trends of suppression with coating, indicating that the correlated parasitic reactions of the electrolyte and carbon electrode could be inhibited with

coating of the electrode. The oxygen evolutions were also maintained with only a slight reduction with cycling, whereas those in the pristine electrode were sharply reduced, as shown in Figure 3.10h. This finding confirms that the use of a ZnO coating on carbon could successfully enhance the stability of the electrolyte and carbon electrode during the cycling. Nevertheless, the shape of the oxygen evolution profile indicates some changes after cycles, with the first hill becoming slightly larger than the second hill, implying the alteration of the nature of the discharge products with cycles and possible progress of the electrode degradation.

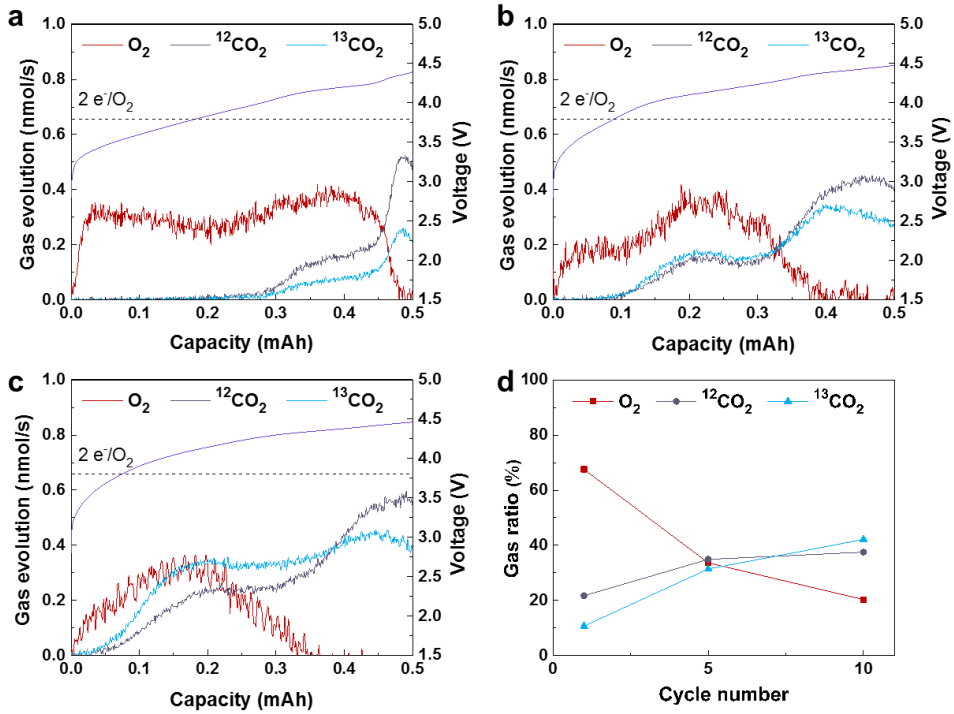

Figure 3.9. *In situ* DEMS analyses in Li–O_2 cells with pristine ^{13}C cathode during (a) first, (b) fifth, and (c) tenth charge. (d) Ratios of evolved gases at pristine ^{13}C cathode during cycling.

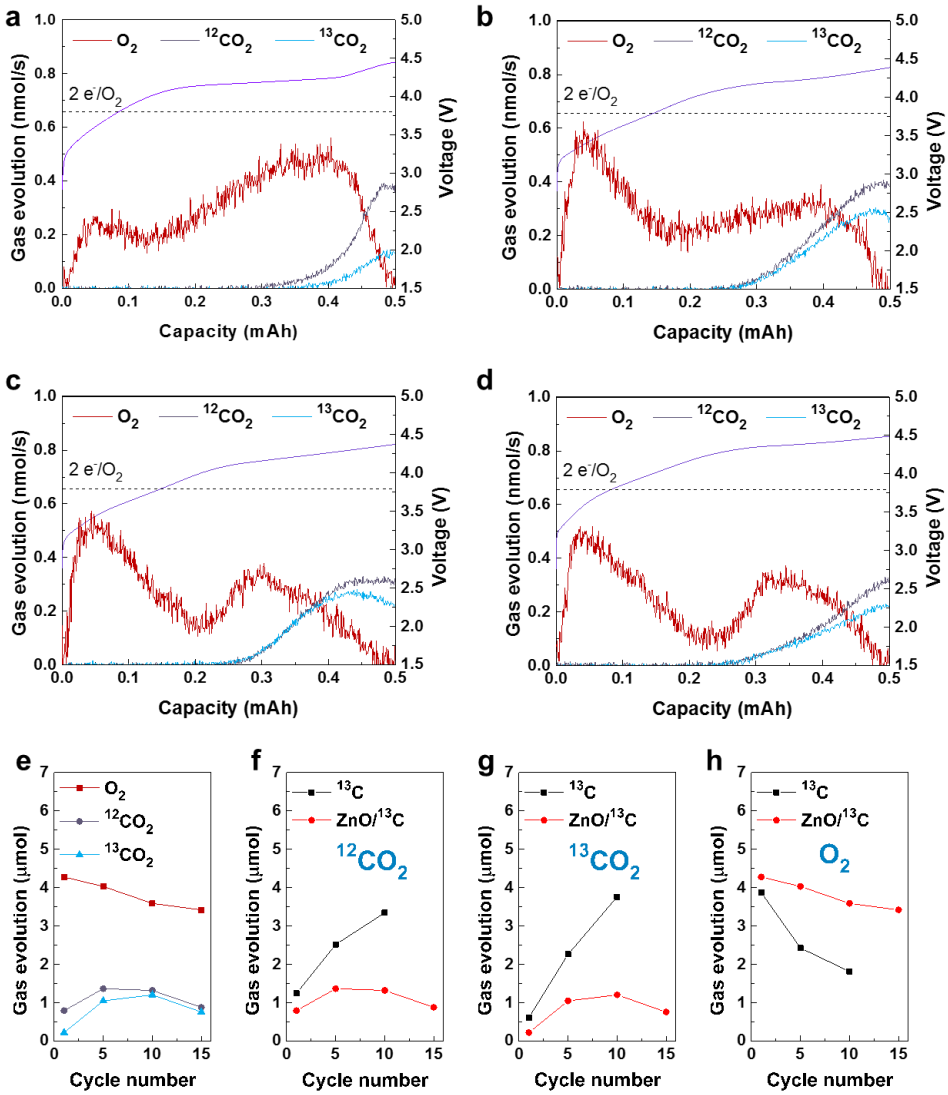

Figure 3.10. *In situ* DEMS analyses in Li–O_2 cells with ZnO-coated ^{13}C cathode during (a) first, (b) fifth, (c) tenth, and (d) fifteenth charge. (e) Amounts of evolved gases at the ZnO-coated ^{13}C cathode during cycling. Summary of the amounts of (f) $^{12}CO_2$, (g) $^{13}CO_2$, and (h) O_2 evolutions during cycling at pristine ^{13}C and ZnO-coated ^{13}C cathodes.

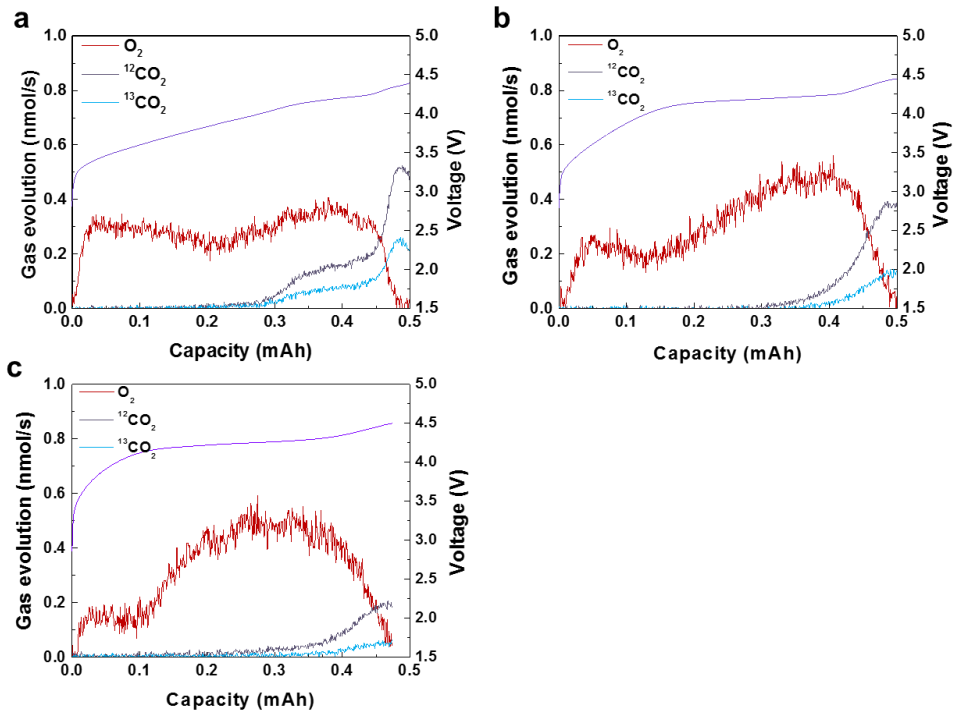

Figure 3.11. *In situ* DEMS analyses in Li–O_2 cells with (a) pristine ^{13}C, (b) 8-cyc ZnO/^{13}C, and (c) 15-cyc ZnO/^{13}C cathodes during the first charge.

Supplementary note 3.4. The formation of "M" shape at oxygen evolution during charging

The typical shape of the oxygen evolution may be influenced by side reactions, not solely by the Li_2O_2 oxidation. In particular, considering the lower oxygen evolution amount compared with the theoretical value, it is certain that side reactions are continuously involved along with the desirable Li_2O_2 decomposition reaction. While the lower value of the oxygen evolution measured is partly due to the under-estimation of the oxygen calibration in our DEMS setup, the relative amount of the oxygen amount varying over the charging process hints at distinct reactions occurring. In the previous paper by Bruce *et al*., carbon corrosion usually occurs above 3.5 V and gets severe with higher charging voltage.[3] In our case in Figure 3.9a which shows gas evolutions in Li-O_2 cell with pristine ^{13}C cathode during the first charge, $^{13}CO_2$ originating from the carbon corrosion starts to evolve at about 4 V and more $^{13}CO_2$ was generated at higher voltage. Nevertheless, if the carbon corrosion is the main factor for the reduction of O_2 evolution in the middle of 'M' shape, O_2 evolution should be getting even smaller above 4 V because of the more severe carbon corrosion and increasing CO_2 evolution. However, O_2 evolution rises above 4 V forming the second hill of 'M' shape, which indicates that the carbon corrosion cannot solely explain the decrease of O_2 evolution specifically in the middle region. In addition, previous works similarly demonstrated that the oxygen evolution like 'M' shape arises even with carbon-free RuO_x/TiN cathode.[4]

Another possible cause is side reactions caused by singlet oxygen.[5,6] In the recent work by Freunberger *et al*., the formation of singlet oxygen gets larger at higher charging voltage, which implies that, for the same reason discussed above, the singlet oxygen is not likely the major factor of 'M' shape.[6] It was shown that singlet oxygen evolution also occurs during the oxidation of chemically synthesized Li_2O_2 above 3.5 V.[6] Accordingly, in our new set of experiments as shown in Figure 3.12, we analyzed the oxygen evolution in chemically synthesized Li_2O_2–containing cathode (ketjenblack, chemically synthesized Li_2O_2, and PVDF with 4.5: 4.5: 1 in wt%) during charge to verify the effect of singlet oxygen without involving complications of different discharge products. In this case, the decrease of O_2 evolution in the middle was not observed despite the presumed singlet oxygen formation above 3.5 V, which again supports that side reactions by singlet oxygen are not the main factor for the 'M' shape.

Because those side reactions are not directly related with the reduction of O_2 evolution in the middle and generally get aggravated with higher charging voltages, explaining the 'M' shape in terms of the nature of discharged Li_2O_2 seems to be more appropriate. At the end of the discharge, two distinct Li_2O_2 phases which contain crystalline toroidal Li_2O_2 and film-like amorphous Li_2O_2 were observed, which depends on various conditions including current density, discharge voltage, presence of solid catalyst, and property of electrolyte.[7-9] In most of practical lithium-oxygen systems, both crystalline and amorphous Li_2O_2 were found to coexist after the discharge, and they are expected to have different natures of ionic and electronic

conductivities.[10,11] Indeed, according to a previous report, ionic and electronic conductivities of amorphous Li_2O_2 are 3–4 orders of magnitude higher than those of crystalline Li_2O_2, which resulted in different charging behaviors between amorphous Li_2O_2 and the crystalline one.[12] These strongly support that first and second hill of 'M' shape is likely to originate from the sequential oxidation of amorphous Li_2O_2 and crystalline Li_2O_2, respectively, while the middle region with the depressed oxygen evolution is attributed to other side reactions arising from the lack of the proper Li_2O_2 to be decomposed at the potential.

[3] *J. Am. Chem. Soc*. **2013**, 135, 494.

[4] *Adv. Sci*. **2015**, 2, 1500092.

[5] *Angew. Chem*. **2016**, 128, 1.

[6] *Nat. Energy* **2017**, 2, 17036.

[7] *Energy Environ. Sci*. **2013**, 6, 1772.

[8] *Nano Lett*. **2013**, 13, 4679.

[9] *Nat. Chem.* **2014**, 6, 1091.

[10] *Adv. Mater*. **2013**, 25, 3129.

[11] *Energy Environ. Sci*. **2013**, 6, 2370.

[12] *Angew. Chem. Int. Ed*. **2016**, 55, 10717.

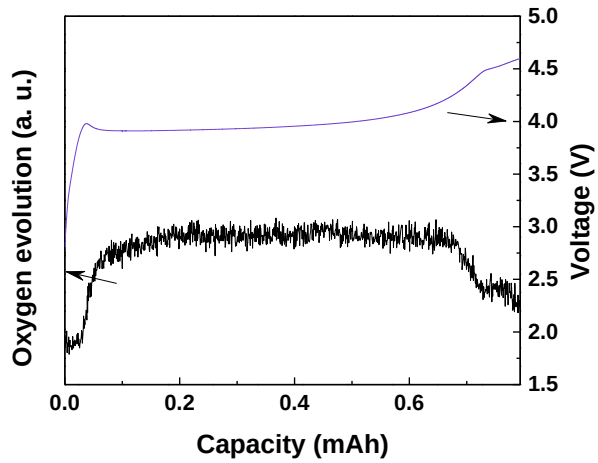

Figure 3.12. *In situ* DEMS analyses during charging of chemically synthesized Li_2O_2.

3.3.4 XPS analyses on ^{13}C and ZnO-coated ^{13}C cathodes after cycling in Li–O_2 cells

XPS spectra in Figure 3.13 were analyzed to compare chemical states of pristine and ZnO-coated ^{13}C electrodes at various cycled states (0, 5, 10, and 15 cycles). As-prepared pristine ^{13}C and ZnO-coated ^{13}C electrodes showed C-C bondings as a major peak with a signature of C−O bondings along with C−F bondings from the binder (Figure 3.13a and b). After five cycles in Figure 3.13c and d, C−C bondings decreased and C−O bondings increased with additional formation of O−C=O bondings which stems possibly from carbonate, acetate, or formate. These phenomena were more noticeable for the pristine ^{13}C electrode, indicating the suppressed side reactions for the coated carbon electrode in consistent with the DEMS results. After ten cycles in Figure 3.13e and f, the difference between the two electrodes became remarkable. The pristine ^{13}C electrode showed an enlarged portion of O−C=O bondings and a negligible signal of C−C bondings, which indicated the excessive accumulation of byproducts by severe side reactions. In contrast, ZnO-coated ^{13}C electrode contained only a small portion of O−C=O bondings, although the amount of byproducts increased slightly in comparison with those after five cycles. Besides, C−C bondings remained clear demonstrating that carbon surface was maintained without the significant passivation. After fifteen cycles in Figure 3.13g and h, O−C=O bondings became larger for both electrodes, while the ZnO coated-^{13}C electrode still displayed the C−C bondings. These XPS

data confirmed cleaner carbon surface with ZnO coating, which is well matched with DEMS data that showed subdued side reactions for ZnO-coated carbon electrode.

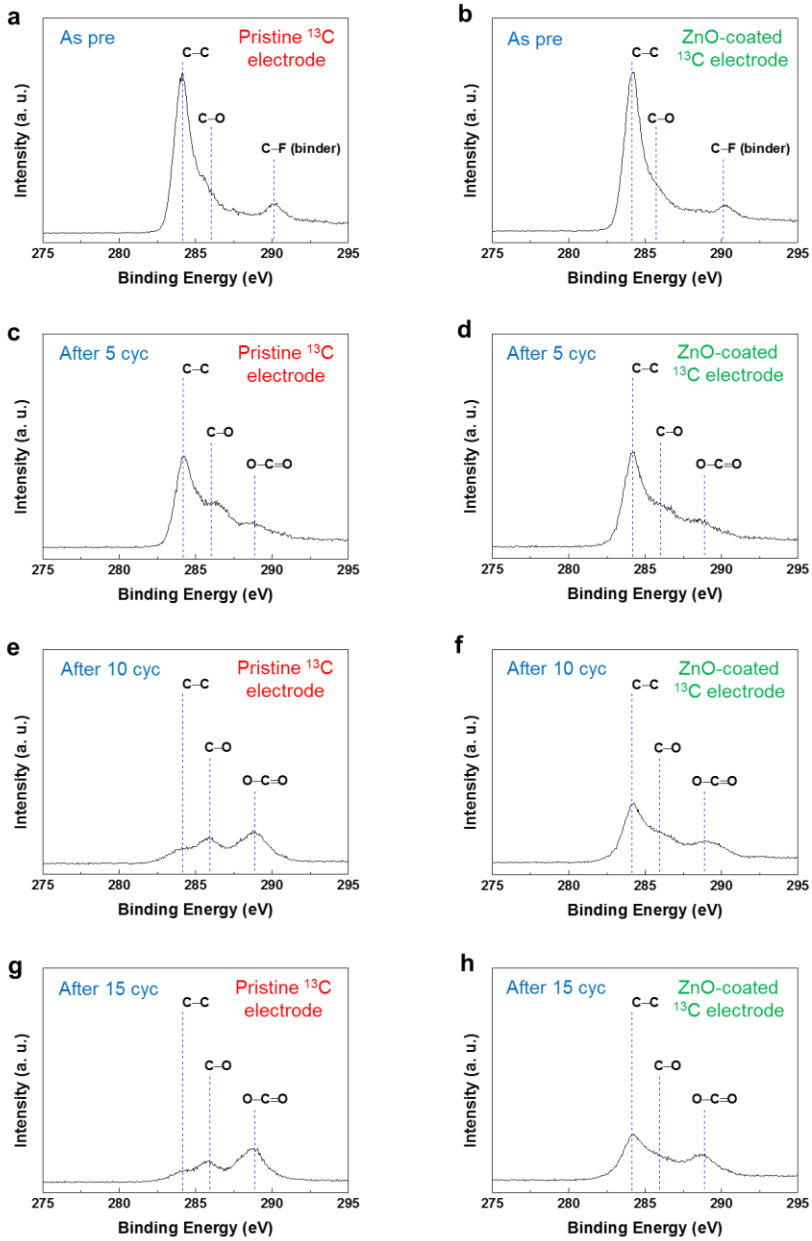

Figure 3.13. XPS spectra of pristine ^{13}C electrode and ZnO-coated ^{13}C electrode (a, b) as prepared, (c, d) after five cycles, (e, f) after ten cycles, and (g, h) after fifteen cycles, respectively.

3.3.5 dq/dV analyses during cycling in Li–O_2 cells with ^{13}C and ZnO-coated ^{13}C cathodes

Figure 3.14 show dq/dV curves of Li-O_2 cell using pristine ^{13}C cathode with the number of cycles and Figure 3.15 is magnified dq/dV curves in Figure 3.14 for the precise analysis of oxidation region. In Figure 3.14, oxygen reduction reaction mainly occurred at 2.65 V during first cycle, and the reduction voltages gradually decreased during cycling (under 2.5 V at fifteenth cycle). This phenomenon indicate increased resistance of the cell and is well matched with XPS results showing build-up of insulating byproducts. In Figure 3.15a and b, there are five voltage region where oxidation reactions actively occurred (3.22, 3.61, 4.02, 4.21 and 4.34 V). Given that CO_2 evolution above 4 V and decrease of O_2 evolution above 4.2 V at pristine ^{13}C electrode during first and fifth charge in Figure 3.9a and b, 4.21 and 4.34 V regions are likely to be mainly related with oxidation of byproducts evolving CO_2 and first two voltage regions are matched with oxidation of Li_2O_2. At the middle region around 4.02 V, oxidation of both Li_2O_2 and byproduct could occur. During fifth charge, 4.21 V oxidation region increased, which resulted in expanded amount of CO_2 evolution in DEMS analysis, and reduction of 3.22 V region may resulted in the shrinkage in first hill of O_2 evolution. During tenth charge, CO_2 started to evolve above ~3.5 V and O_2 evolution ceased above 4.2 V as shown in Figure 3.9c. In addition, oxidation voltages are elevated (3.22, 3.80, 4.30, and 4.43 V) in Figure 3.15 due to increased polarization over cycles. In this case, CO_2 evolution occurred at

3.80, 4.30, and 4.43 V oxidation regions and enormous amount of CO_2 evolution in Figure 3.9c was mainly originated from increase of 4.30 and 4.43 V regions in Figure 3.15c. During fifteenth charge in Figure 3.15d, oxidation mainly occurred above 4.25 V which implied negligible Li-O_2 chemistry and approaching cell failure.

Li-O_2 cell using ZnO-coated ^{13}C cathode was also analyzed using dq/dV curves with the number of cycles in Figure 3.16, and their magnified graphs were presented in Figure 3.17. Unlike the case in pristine ^{13}C cathode, ZnO-coated ^{13}C cathode showed constant reduction voltage around 2.70 V during all the cycles in Figure 3.16, which demonstrate high reversibility of coated carbon cathode. In Figure 3.17a and b, oxidation reactions mainly occurred at 4.02 and 4.27 V during first and fifth cycles. As shown in Figure 3.10 which present DEMS result at ZnO-coated ^{13}C electrode, CO_2 evolution started above 4.2 V. Therefore, it can be inferred that 4.02 V peak was related to the oxidation of Li_2O_2, whereas 4.27 V and above region was originated from oxidation of byproducts evolving CO_2. During fifth and tenth cycles, oxidation regions near 4.27 V increased, which resulted in a bit more enlarged amounts of CO_2 evolution in Figure 3.10b and c. The oxidation region near 3.07 V after tenth cycle seems to be related with detachment of ZnO which led to formation of defective Li_2O_2. Although Li_2O_2 oxidation peak shifted to 4.18 V during fifteenth cycle, oxidation peak was sustained well in comparison with dq/dV curve during fifteenth cycle at pristine ^{13}C electrode in Figure 3.15d, which demonstrate high stability at coated carbon electrode.

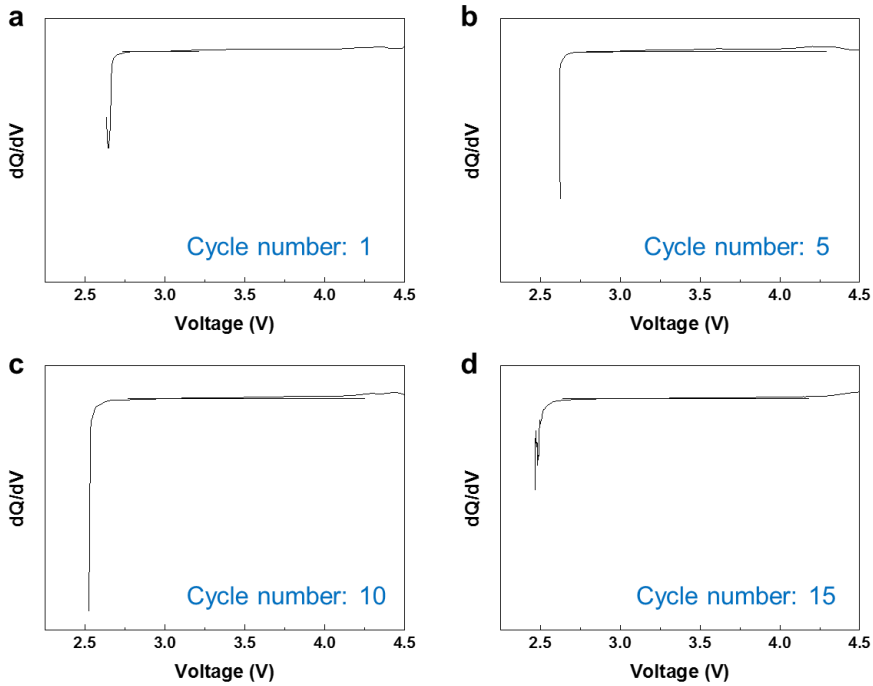

Figure 3.14. dq/dV curves at (a) first, (b) fifth, (c) tenth, (d) fifteenth cycles in Li-O_2 cell with pristine ^{13}C cathode as a cathode.

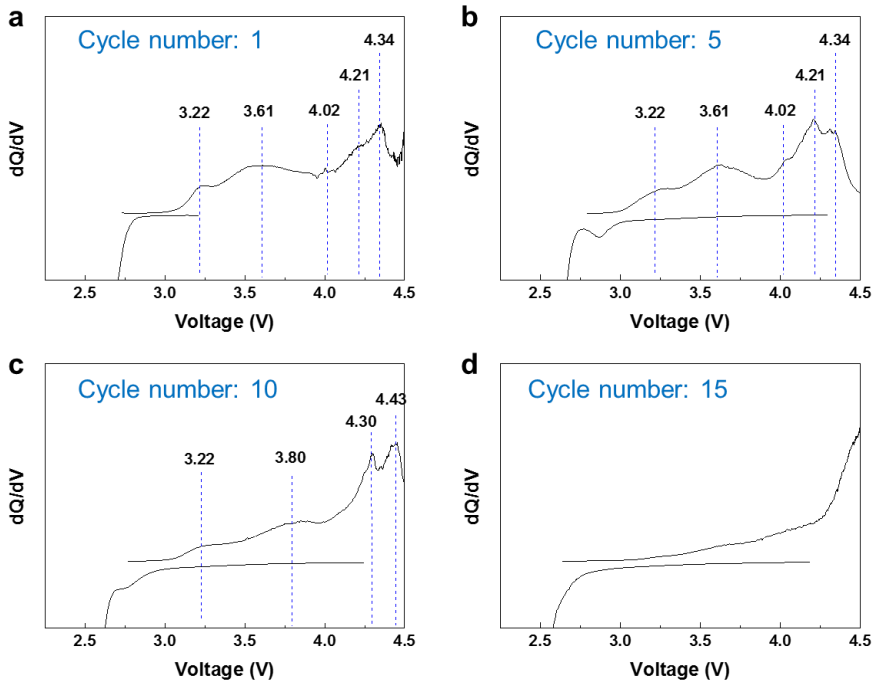

Figure 3.15. Magnified dq/dV curves at (a) first, (b) fifth, (c) tenth, (d) fifteenth cycles in Li-O_2 cell with pristine ^{13}C cathode as a cathode.

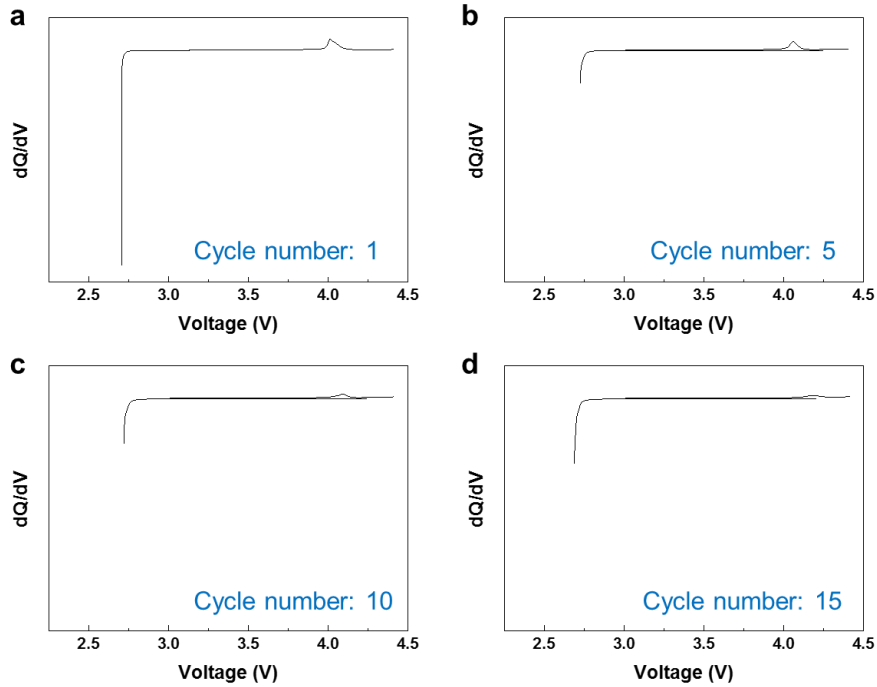

Figure 3.16. dq/dV curves at (a) first, (b) fifth, (c) tenth, (d) fifteenth cycles in Li-O_2 cell with ZnO-coated ^{13}C cathode as a cathode.

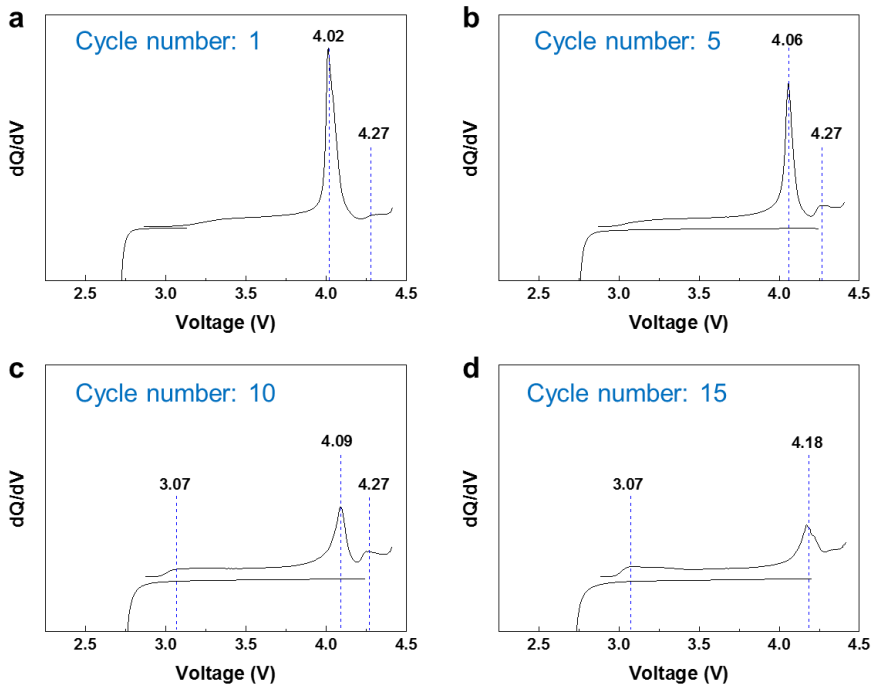

Figure 3.17. Magnified dq/dV curves at (a) first, (b) fifth, (c) tenth, (d) fifteenth cycles in Li-O_2 cell with ZnO-coated ^{13}C cathode as a cathode.

3.3.6 Degradation mechanism of ZnO-coated carbon cathodes

The stability of the coating was investigated by carefully disassembling the degraded cell and examining the electrode using TEM to understand the gradual change of the gas evolution profile and the possible degradation mechanism. Figure 3.18a and b present TEM images of the ZnO-coated electrode after the cell became electrochemically inactive after extended cycling (>100 cycles). Compared with the initial morphology in Figure 3.1b, most of the ZnO nanoparticles (marked in yellow) were detached from the surface of the carbon after cycling, which is similar to CeO_2 in the previous report.[59] To confirm this observation and for clearer visualization, we performed similar sets of experiments for the CNT electrode coated with ZnO at different cycle numbers. The TEM images in Figure 5c–f illustrate how the surface coated ZnO evolves during cycling. After the first discharge in Figure 5c, discharge products were uniformly deposited on both the CNT and ZnO nanoparticles. On the other hand, more Li_2O_2 discharge product began to form at the interface between CNT and ZnO during the third discharge, leading to the detachment of some ZnO nanoparticles from the CNT wall (Figure 3.18d). However, after the charging process when Li_2O_2 between the carbon surface and ZnO would significantly be reduced in the amount, it appears that ZnO gets stuck to the carbon surface due to the remaining residual Li_2O_2 that may hold the ZnO on the carbon surface to some extent as shown in Figure 3.19. Nevertheless, ZnO already detached after the charge would lose the adhesion to the carbon surface, and more serious detachments were observed after

the fifth discharge, as shown in Figure 3.18e and f. The amount of isolated ZnO nanoparticles continued to increase with increasing cycles. The origin of the Li_2O_2 formation at the interface between carbon and the coating material is not currently clear but we believe that it may depend on several factors such as the binding strength between coating materials and carbon cathode, electrical conductivity of coating material, and the discharge mechanism involving surface coating or precipitation from the solution. Binding strength can be an intuitive and direct index to the detachment. Strong binding between the coating material and carbon would lead to a difficulty for Li_2O_2 to be formed between the two. Also, if the coating material is as electrically conductive as the carbon, Li_2O_2 can be formed relatively easily on the surface of coating materials, which is expected to result in non-detaching coating. On the other hand, if the coating material is insulating, Li_2O_2 cannot grow on the surface of coating material, bringing about Li_2O_2 growth primarily between the carbon surface and coating material, and finally fall-off of the coating. Based on this speculation, the conductive noble metal oxide or metal particle will suffer less detachment problem. Indeed, previous works showed that FeCo particles were not detached after discharge.[60] Discharge mechanism can be also closely related to where the discharge product is formed, and coating materials are likely to be less affected by the solution-mediated reaction. The detachment problem implies that the effect of the ZnO coating would be less effective with cycling and may explain the gradual change of the gas evolution behavior and the capacity degradation with extended cycles.

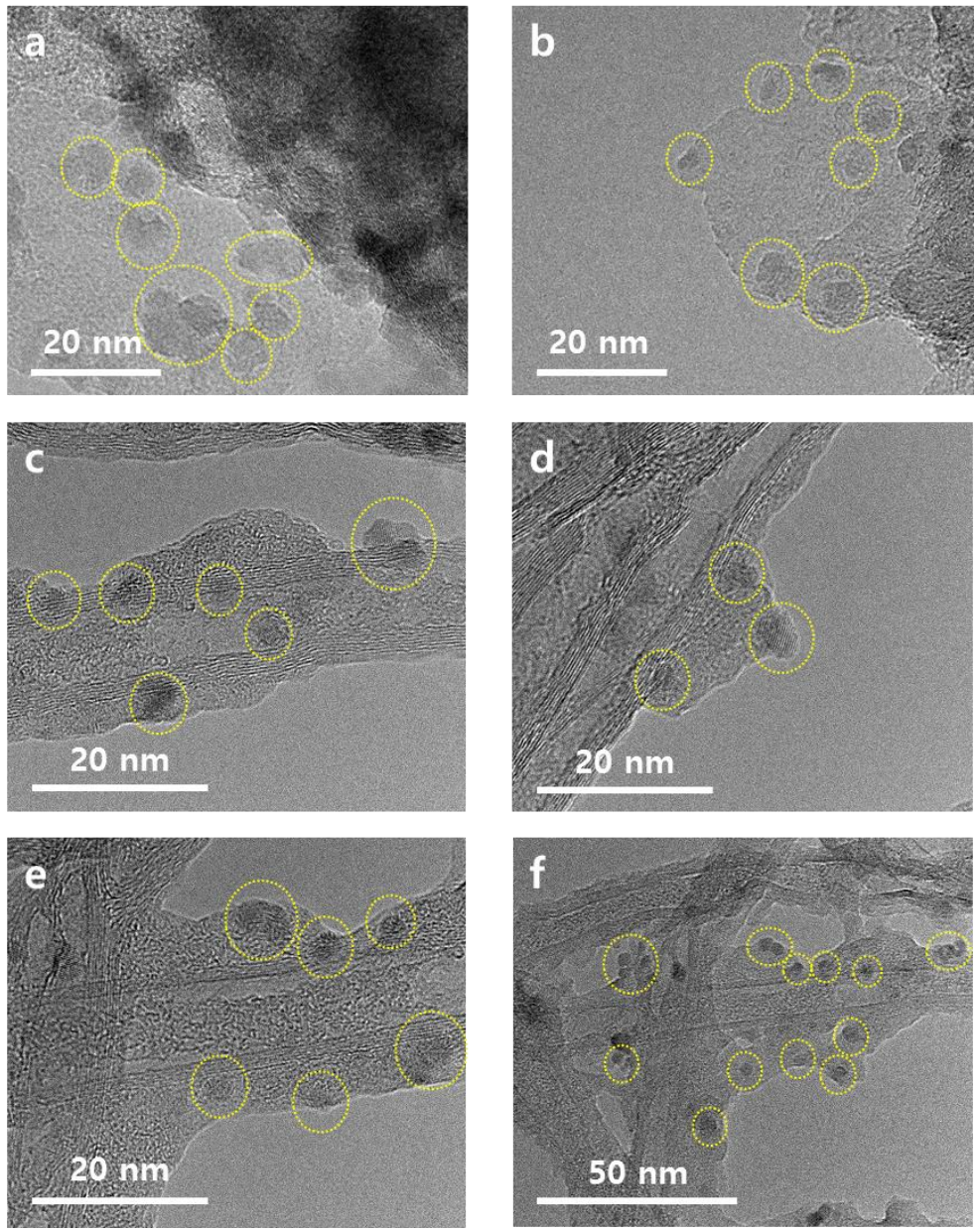

Figure 3.18. (a,b) TEM images of ZnO-coated ^{13}C cathode after cycling. TEM images of ZnO-coated CNT cathode after (c) first, (d) third, and (e,f) fifth discharge.

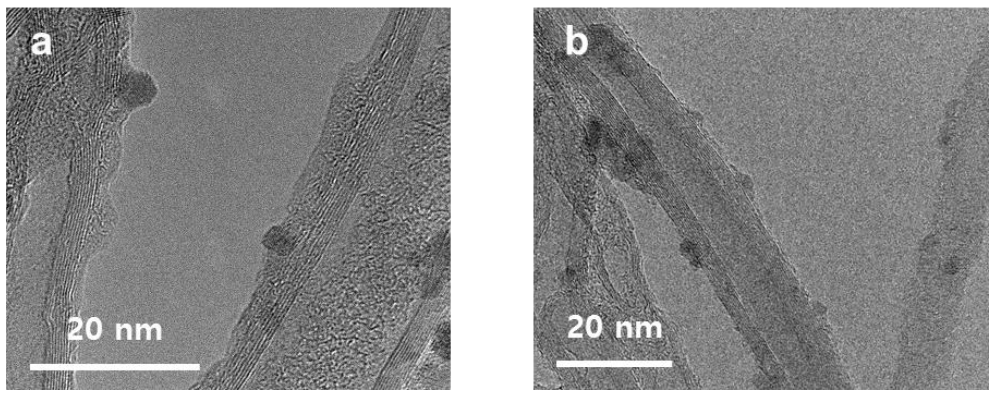

Figure 3.19. TEM images of ZnO-coated CNT cathode after (a) third and (b) fifth charge. The capacity was limited to 1000 mAh g^{-1}.

3.4 Concluding remarks

The effect of surface coating on a carbon air electrode was investigated using isotope ^{13}C carbon and *in situ* DEMS analysis. The ZnO-coated carbon air electrode was highly resistant to side reactions both in the electrolyte and carbon air electrode, which resulted in enhanced cycle performance. In contrast to the pristine carbon electrode, the coating provided effective protection, which reduced the evolution of undesirable gases from both the electrolyte ($^{12}CO_2$) and carbon electrode ($^{13}CO_2$), with high efficiency of O_2 evolution. Nevertheless, the coating materials were gradually detached from the surface of the carbon materials because of the formation of a discharge product at the interface between the carbon and coating materials during cycling, leading to exposure of the bare carbon electrode and degradation of the Li–O_2 cell. This study suggests that a method to prevent the detachment of the coating material as well as further understanding of the growth mechanism of discharge products, which affects the delamination of the coating, should be sought after in the future.

3.5 References

[1] M. Armand, J.-M. Tarascon, *Nature* **2008**, 451, 652.

[2] R. Black, B. Adams, L. Nazar, *Adv. Energy Mater.* **2012**, 2, 801.

[3] P. G. Bruce, S. A. Freunberger, L. J. Hardwick, J.-M. Tarascon, *Nat. Mater.* **2012**, 11, 19.

[4] G. Girishkumar, B. McCloskey, A. Luntz, S. Swanson, W. Wilcke, *J. Phys. Chem. Lett.* **2010**, 1, 2193.

[5] M. S. Whittingham, *Chem. Rev.* **2004**, 104, 4271.

[6] M. D. Bhatt, H. Geaney, M. Nolan, C. O'Dwyer, *Phys. Chem. Chem. Phys.* **2014**, 16, 12093.

[7] Y.-C. Lu, Y. Shao-Horn, *J. Phys. Chem. Lett.* **2012**, 4, 93.

[8] H. Kim, H.-D. Lim, J. Kim, K. Kang, *J. Mater. Chem. A* **2014**, 2, 33.

[9] S. J. Kang, T. Mori, S. Narizuka, W. Wilcke, H.-C. Kim, *Nat. Commun.* **2014**, 5, 3937.

[10] Y. Bae, H.-D. Lim, Y. S. Yun, K. Kang, *J. Electrochem. Sci. Technol.* **2014**, 5, 49.

[11] H. D. Lim, K. Y. Park, H. Song, E. Y. Jang, H. Gwon, J. Kim, Y. H. Kim, M. D. Lima, R. O. Robles, X. Lepró, R. H. Baughman, K. Kang, *Adv. Mater.* **2013**, 25, 1348.

[12] H. D. Lim, H. Song, J. Kim, H. Gwon, Y. Bae, K. Y. Park, J. Hong, H. Kim, T. Kim, Y. H. Kim, X. Lepró, R. Ovalle-Robles, R. H. Baughman, K. Kang, *Angew. Chem., Int. Ed.* **2014**, 53, 3926.

[13] H.-D. Lim, H. Song, H. Gwon, K.-Y. Park, J. Kim, Y. Bae, H. Kim, S.-K. Jung, T. Kim, Y. H. Kim, X. Lepró, R. Ovalle-Robles, R. H. Baughman, K. Kang, *Energy Environ. Sci.* **2013**, 6, 3570.

[14] Z. K. Luo, C. S. Liang, F. Wang, Y. H. Xu, J. Chen, D. Liu, H. Y. Sun, H. Yang, X. P. Fan, *Adv. Funct. Mater.* **2014**, 24, 2101.

[15] R. Mi, H. Liu, H. Wang, K.-W. Wong, J. Mei, Y. Chen, W.-M. Lau, H. Yan, *Carbon* **2014**, 67, 744.

[16] W.-H. Ryu, T.-H. Yoon, S. H. Song, S. Jeon, Y.-J. Park, I.-D. Kim, *Nano Lett.* **2013**, 13, 4190.

[17] G. Wu, N. H. Mack, W. Gao, S. Ma, R. Zhong, J. Han, J. K. Baldwin, P. Zelenay, *ACS Nano* **2012**, 6, 9764.

[18] J. Xie, X. Yao, Q. Cheng, I. P. Madden, P. Dornath, C. C. Chang, W. Fan, D. Wang, *Angew. Chem.* **2015**, 127, 4373.

[19] M. M. Ottakam Thotiyl, S. A. Freunberger, Z. Peng, P. G. Bruce, *J. Am. Chem. Soc.* **2012**, 135, 494.

[20] B. McCloskey, A. Speidel, R. Scheffler, D. Miller, V. Viswanathan, J. Hummelshøj, J. Nørskov, A. Luntz, *J. Phys. Chem. Lett.* **2012**, 3, 997.

[21] D. M. Itkis, D. A. Semenenko, E. Y. Kataev, A. I. Belova, V. S. Neudachina, A. P. Sirotina, M. Hävecker, D. Teschner, A. Knop-Gericke, P. Dudin, *Nano Lett.* **2013**, 13, 4697.

[22] Y. Bae, Y. S. Yun, H.-D. Lim, H. Lee, Y.-J. Kim, J. Kim, H. Park, Y. Ko, S. Lee, H. J. Kwon, H. Kim, H.-T. Kim, D. Im, K. Kang, *Chem. Mater.* **2016**, 28, 8160.

[23] M. Leskes, A. J. Moore, G. R. Goward, C. P. Grey, *J. Phys. Chem. C* **2013**, 117, 26929.

[24] B. M. Gallant, R. R. Mitchell, D. G. Kwabi, J. Zhou, L. Zuin, C. V. Thompson, Y. Shao-Horn, *J. Phys. Chem. C* **2012**, 116, 20800.

[25] S. A. Freunberger, Y. Chen, N. E. Drewett, L. J. Hardwick, F. Bardé, P. G. Bruce, *Angew. Chem., Int. Ed.* **2011**, 50, 8609.

[26] Z. Peng, S. A. Freunberger, Y. Chen, P. G. Bruce, *Science* **2012**, 337, 563.

[27] M. M. O. Thotiyl, S. A. Freunberger, Z. Peng, Y. Chen, Z. Liu, P. G. Bruce, *Nat. Mater.* **2013**, 12, 1050.

[28] W.-J. Kwak, H.-G. Jung, S.-H. Lee, J.-B. Park, D. Aurbach, Y.-K. Sun, *J. Power Sources* **2016**, 311, 49.

[29] X. Gao, Y. Chen, L. R. Johnson, Z. P. Jovanov, P. G. Bruce, *Nat. Energy* **2017**, 2, 17118

[30] J.-J. Xu, X.-B. Zhang, *Nat. Energy* **2017**, 2, 17133

[31] J. Lu, Y. Lei, K. C. Lau, X. Luo, P. Du, J. Wen, R. S. Assary, U. Das, D. J. Miller, J. W. Elam, H. M. Albishri, D. A. El-Hady, Y.-K. Sun, L. A. Curtiss, K. Amine, *Nat. Commun.* **2013**, 4, 2383.

[32] J. Elam, D. Routkevitch, S. George, *J. Electrochem. Soc.* **2003**, 150, G339.

[33] Y.-S. Min, I. H. Lee, Y. H. Lee, C. S. Hwang, *CrystEngComm* **2011**, 13, 3451.

[34] Y.-S. Min, E. J. Bae, J. B. Park, U. J. Kim, W. Park, J. Song, C. S. Hwang, N. Park, *App. Phys. Lett.* **2007**, 90, 263104.

[35] E. Yilmaz, C. Yogi, K. Yamanaka, T. Ohta, H. R. Byon, *Nano Lett*. **2013**, 13, 4679.

[36] F. Li, Y. Chen, D.-M. Tang, Z. Jian, C. Liu, D. Golberg, A. Yamada, H. Zhou, *Energy Environ. Sci*. **2014**, 7, 1648.

[37] Q.-C. Liu, J.-J. Xu, Z.-W. Chang, X.-B. Zhang, *J. Mater. Chem. A* **2014**, 2, 6081.

[38] J. Schwan, S. Ulrich, V. Batori, H. Ehrhardt, S. Silva, *J. Appl. Phys.* **1996**, 80, 440.

[39] B. J. Bergner, A. Schürmann, K. Peppler, A. Garsuch, J. Janek, *J. Am. Chem. Soc.* **2014**, 136, 15054.

[40] W.-J. Kwak, D. Hirshberg, D. Sharon, M. Afri, A. A. Frimer, H.-G. Jung, D. Aurbach, Y.-K. Sun, *Energy Environ. Sci.* **2016**, 9, 2334.

[41] D. J. Lee, H. Lee, Y. J. Kim, J. K. Park, H. T. Kim, *Adv. Mater.* **2016**, 28, 857.

[42] W.-J. Kwak, D. Hirshberg, D. Sharon, H.-J. Shin, M. Afri, J.-B. Park, A. Garsuch, F. F. Chesneau, A. A. Frimer, D. Aurbach, Y.-K. Sun, *J. Mater. Chem. A* **2015**, 3, 8855.

[43] C. M. Burke, R. Black, I. R. Kochetkov, V. Giordani, D. Addison, L. F. Nazar, B. D. McCloskey, *ACS Energy Lett.* **2016**, 1, 747.

[44] S. H. Yoon, Y. J. Park, *Sci. Rep.* **2017**, 7, 42617.

[45] J. Kang, J. Kim, S. Lee, S. Wi, C. Kim, S. Hyun, S. Nam, Y. Park, B. Park, *Adv. Energy Mater.* **2017**, 7, 1700814

[46] B. G. Kim, C. Jo, J. Shin, Y. Mun, J. Lee, J. W. Choi, *ACS nano* **2017**, 11, 1736.

[47] D. Kundu, R. Black, E. J. Berg, L. F. Nazar, *Energy Environ. Sci*. **2015**, 8, 1292.

[48] D. Oh, K. Virwani, L. Tadesse, M. Jurich, N. Aetukuri, L. E. Thompson, H.-C. Kim, D. S. Bethune, *J. Phys. Chem. C* **2017**, 121, 1404.

[49] S. M. Ahn, J. Suk, D. Y. Kim, Y. Kang, H. K. Kim, D. W. Kim, *Adv. Sci.* **2017**, 4, 1700235.

[50] D. W. Kim, S. M. Ahn, J. Kang, J. Suk, H. K. Kim, Y. Kang, *J. Mater. Chem. A* **2016**, 4, 6332.

[51] Y. Chang, S. Dong, Y. Ju, D. Xiao, X. Zhou, L. Zhang, X. Chen, C. Shang, L. Gu, Z. Peng, G. Cui, *Adv. Sci*. **2015**, 2, 1500092.

[52] B. D. Adams, C. Radtke, R. Black, M. L. Trudeau, K. Zaghib, L. F. Nazar, *Energy Environ. Sci.* **2013**, 6, 1772.

[53] Y. Zhang, Q. Cui, X. Zhang, W. C. McKee, Y. Xu, S. Ling, H. Li, G. Zhong, Y. Yang, Z. Peng, *Angew. Chem. Int. Ed*. **2016**, 55, 10717.

[54] J. Wandt, P. Jakes, J. Granwehr, H. A. Gasteiger, R.-A. Eichel, *Angew. Chem*. **2016**, 128, 7006.

[55] N. Mahne, B. Schafzahl, C. Leypold, M. Leypold, S. Grumm, A. Leitgeb, G. A. Strohmeier, M. Wilkening, O. Fontaine, D. Kramer, C. Slugovc, S. M. Borisov, S. A. Freunberger, *Nat. Energy* **2017**, 2, 17036.

[56] B. D. Adams, R. Black, C. Radtke, Z. Williams, B. L. Mehdi, N. D.

Browning, L. F. Nazar, *ACS nano* **2014**, 8, 12483.

[57] S. R. Gowda, A. Brunet, G. M. Wallraff, B. D. McCloskey, *J. Phys. Chem. Lett.* **2013**, 4, 276.

[58] S. Zhang, M. J. Nava, G. K. Chow, N. Lopez, G. Wu, D. R. Britt, D. G. Nocera, C. C. Cummins, *Chem. Sci.*, **2017**, 8, 6117

[59] C.Yang, R. A. Wong, M. Hong, K. Yamanaka, T. Ohta, H. R. Byon, *Nano Lett*. **2016**, 16, 2969

[60] W.-J. Kwak, T.-G. Kang, Y.-K. Sun, Y. J. Lee, *J. Mater. Chem. A*, **2016**, 4, 7020

Chapter 4. Dual-Functioning Molecular Carrier of Superoxide Radicals for Stable and Efficient Lithium–oxygen Batteries

4.1 Research Background

With increasing demands for electric vehicles (xEVs), researches on next-generation rechargeable batteries have been spurred in the past decades. Among various battery systems, non-aqueous lithium oxygen (Li-O_2) batteries have attracted a particular attention as a potential game changer due to their extremely high theoretical specific energy (~3500 Wh kg^{-1}) based on the simple oxygen reduction and evolution reaction: $2Li^+ + O_2 + 2e^- \leftrightarrow Li_2O_2$ (E^o = 2.96 V vs. Li/Li^+).[1-3] During discharge, oxygen is reduced to superoxide radical (O_2^-) and reacts with lithium ion to form metastable LiO_2 (Reaction 1 and 2).[4-6] Subsequently, LiO_2 can undergo two different reaction pathways in which either further electrochemical reduction of LiO_2 with an electron and Li^+ ion (Reaction 3) or a chemical disproportionation of two LiO_2 (Reaction 4) occur, both resulting in the formation of final discharge product, Li_2O_2.[7, 8] During charge, Li^+ ion and electrons are extracted from Li_2O_2 evolving oxygen gases ($Li_2O_2 \rightarrow 2Li^+ + 2e^- + O_2$).

Reaction 1: $O_2 + e^- \rightarrow O_2^-$

Reaction 2: $Li^+ + O_2^- \rightarrow LiO_2$

Reaction 3: $LiO_2 + Li^+ + e^- \rightarrow Li_2O_2$

Reaction 4: $2LiO_2 \rightarrow Li_2O_2 + O_2$

Intermediate radical species like O_2^- or LiO_2 have been known to be quite reactive causing various side reactions with electrolyte solvent and typical carbon-based cathodes, deteriorating the Li-O_2 cell operation.[5, 9-18] Representative side products triggered by these reactive radical species includes lithium carbonate (Li_2CO_3),[7, 18-20] whose accumulation on the air-electrode leads to high overpotential during charge and exacerbates the corrosion of the electrode.[16-18] Extensive research efforts have been placed in resolving the issues, proposing new electrolyte systems and/or cathode materials robust against these radical species.[5, 11-17, 21-28] Various solvent properties related to electrolyte stability in Li-O_2 cell such as donor and acceptor numbers, pKa, and highest occupied molecular orbital (HOMO) level have been explored.[5, 12-15, 24] Ether-based electrolytes have shown suitable values in those categories, thus have been expected to be relatively stable against side reactions caused by oxygen radicals such as H-abstraction and nucleophilic attack.[14, 15, 24] Modifications of conventional electrolyte systems to enhance the intrinsic stability of solvent have been also carried out, such as methylation of dimethyl ether (DME) or cyclic ether.[22, 23] The employment of the new electrolytes led to the partial success in improving the cycle stability, however remains still far from practice. Stable materials for the air-cathode were also intensively sought after. Various carbon materials including carbon blacks, graphene and carbon nanotube have been mainly

utilized as cathode materials due to light weight, high electrical conductivity, and large specific surface area, however they were often accompanied by serious degradations involving reactive oxygen species during cycling.[16-18, 28-34] Au, TiC, and Ag were employed to replace the conventional carbon-based electrode, exhibiting much improved stability against the parasitic reactions.[25-27] Nevertheless, the high prices and low specific capacities from the use of heavy elements remain as problems, limiting their practical applications. Reactive oxygen radical species are one of the main causes of parasitic reactions, prohibiting the use of conventional electrolytes and carbon cathodes. The breakthrough in suppressing such side reactions is imperative for the stable operation of Li-O_2 batteries.

Herein, we attempt to regulate the reactivity of oxygen radical species by inducing the reversible formation of stable intermediate complex carrying superoxide radicals. The concept of oxygen carrying materials such as FePc and Heme based on $Fe^{2+/3+}$ redox centers have been reported, and shown improved solution process in Li-O_2 chemistry induced by oxygen carriers.[35, 36] Nevertheless, it is not clearly understood how and to what extent these oxygen carriers suppress the reactivity of oxygen radicals and whether their effects are directly related to the stability of Li-O_2 cells. In this study, it is shown that 5-dimethyl-1-pyrroline N-oxide (DMPO), which is a widely-known chemical agent to detect O_2^-, is capable of capturing O_2^- to form an intermediate DMPO-O_2^- complex and mediating the formation of the final Li_2O_2 discharge product.[37-41] The stabilization of the complex attributable to the resonance effect leads to the substantial reduction in the parasitic

reactions involving the radicals.[42, 43] We also reveal the dual function of DMPO, which promotes the charging process by actively scavenging the superoxide species formed on the surface of the solid $Li_{2-x}O_2$ upon charging. It leads to the remarkable reduction in the overpotential and high oxygen efficiency as will be shown by differential electrochemical mass spectrometry (DEMS) and cyclability test. Our findings demonstrate the importance of regulating the radical reactivity for stable Li-O_2 battery and propose that the radical stabilizing molecules can serve as a platform to enhance the stability and efficiency of Li-O_2 batteries, prompting further community effort for the development of better superoxide carrier.

4.2 Experimental method

4.2.1 Preparation of Li–O_2 cells and conditions for electrochemical cell tests

Li metal foil (7/16 inch diameter), a glass fiber separator (Whatman GF/F microfiber filter paper, 0.7 μm pore size), the electrolyte, and the carbon cathodes were stacked in sequence in a Swagelok-type cell. The electrolyte was 1 M lithium bis(trifluoromethane)sulfonimide (LiTFSI) in tetraethylene glycol dimethylether (TEGDME), and 0.2 or 0.5 M DMPO (Sigma-Aldrich) was added into the electrolyte for the DMPO test. All the cells were assembled in a glove box (H_2O < 0.5 ppm, O_2 < 0.5 ppm) and operated in an O_2 atmosphere (770 Torr). Each cell was relaxed for 1 hour in an O_2 atmosphere. For the first discharge charge test in Figure 2, the Li-O_2 cells with and without DMPO were operated with a current density of 0.1 mA cm^{-2} using the capacity-limited mode of 0.5 mAh (^{13}C cathode) within the voltage range of 2.0 to 4.5 V. For the cycle test in Figure 5, the cells were operated using the capacity-limited mode of 1,000 mAh g^{-1} (Hierarchical CNT electrode) with a current density of 1,000 mA g^{-1} within the voltage range of 2.0 to 4.6 V. For the CV tests, Ag/$AgNO_3$, Pt wire, and gold electrode were used as reference, counter, and working electrode, respectively, and the scan rate was 100 mV s^{-1}.A potentio-galvanostat (WBCS 3000, WonA Tech, Korea) was used to measure the electrochemical properties.

4.2.2 Characterizations

The morphologies of the samples were examined using field-emission SEM (FE-SEM, MERLIN Compact, ZEISS, Germany). The chemical composition and crystallinity of the carbon-based air electrodes were probed using XPS (Thermo VG Scientific) and XRD (D2 PHASER, Bruker). The Raman spectra (LabRam HR, Horiba Jobin-Yvon, France) were recorded using a continuous-wave linearly polarized laser (wavelength: 514.5 nm; 2.41 eV; power: 16 mW). *In situ* DEMS was used to analyze the gases evolved from the Li–O_2 cell during charging. The details of the DEMS system were provided in previous work.[16] EPR analysis was performed using a Bruker EMX/Plus spectrometer equipped with a dual-mode cavity (ER 4116 DM) at room temperature. The experimental conditions were as follows: microwave frequency: 9.64 GHz; modulation amplitude: 1 G; modulation frequency: 100 kHz; microwave power: 1 mW. All the samples were loaded into the capillary tube for EPR measurement.

4.3 Results and Discussions

4.3.1 Verification of the effect of DMPO on the stabilization of Li–O_2 cells during discharge

DMPO has been commonly used as a chemical agent to probe and quantify the contents of oxygen radicals in the fields of analytic chemistry, and is known to be capable of forming a stable DMPO-O_2^- complex, whose stable nature offers sufficient time and steadiness to analyze the radical species.[37-41] To verify its potential application in Li-O_2 cell, we first examined whether the formation of the stable DMPO complex would permanently passivate the oxygen and prevent the intrinsic electrochemical reaction with lithium ions. In this regard, Li-O_2 cells employing DMPO in the electrolyte (0.2 M) were constructed, and the discharge products were scrutinized comparatively with those of the cell without DMPO. Figure 4.1a-c present X-ray diffraction (XRD), Raman, and X-ray photoelectron spectroscopy (XPS) spectra of the discharge products from both cells (See supplementary information for the discharge profiles). Characteristic peaks of Li_2O_2 are observable at 32.8°, 34.9°, and 58.6° for the reference cell, which agrees with previous studies, indicating the formation of crystalline Li_2O_2.[44, 45] On the other hand, no apparent peaks were observed in the XRD of the discharged electrodes from the cell employing DMPO, even though a same amount of discharge capacity was delivered with the reference cell, indicating the alternation of the discharge process with the presence of DMPO. Raman and XPS spectra revealed that the discharge

products of both cells with and without DMPO are all Li_2O_2 in Figure 4.1b and c. Raman shifts of 256 and 788 cm^{-1} are clearly detectable, which are characteristic peaks of Li_2O_2. Moreover, XPS Li 1s spectra illustrate that peaks at binding energy of 54.5 eV corresponding to Li_2O_2 phase are consistently observed in both samples, supporting that final discharge product is Li_2O_2. Combining XRD, Raman and XPS data, it is supposed that the addition of DMPO in the electrolyte results in discharge product, Li_2O_2, with much less crystallinity. The morphological change in Li_2O_2 in the presence of DMPO could be also suggested by the scanning electron microscopy (SEM) in Figure 4.2. It shows that, after discharge without DMPO, representative toroidal Li_2O_2 particles are observed in Figure 4.2c and d, whereas a film-like morphology with undefined small particles is observed when discharged with DMPO in Figure 4.2e and f. According to previous works, the morphological aspects of discharge products are key indicator of the discharge mechanism, inferring the solution or surface mechanism, which also affects the crystallinity of the Li_2O_2.[45, 46] While the properties of the electrolyte (*e.g.* donor number or water contents) are generally known to sensitively influence the discharge mechanism, thus the morphology of Li_2O_2; we speculate that the transition of the morphology here is attributed to the inhibition of the crystalline Li_2O_2 formation in the presence of DMPO in the electrolyte. Bulky DMPO-O_2^- complex may impede the agglomeration of LiO_2 in the electrolyte and subsequent crystallization, resulting in the amorphourization of Li_2O_2, which will be discussed more in detail later.

We found that the discharge products from the cell employing DMPO

contain noticeably smaller amount of lithium carbonate, major byproducts of typical Li-O_2 cells during discharge. Figure 4.1d presents C 1s XPS spectra of discharged carbon cathodes with (blue) and without (red) 0.2 M DMPO, respectively. The discharged cathode with DMPO exhibits lower O-C=O peak corresponding to Li_2CO_3 to C-C peak ratio, which implies that side reactions yielding Li_2CO_3 have been suppressed in the presence of DMPO. Inspired by this finding, we decided to further confirm the reduced side reactions by DMPO in a separate series of cells by quantitatively analyzing the carbonate species in the discharged electrodes. In a new setup, the isotopic ^{13}C was used as the cathode materials, and the electrolyte is composed of naturally abundant ^{12}C, so that the origin of the possible lithium carbonate formation in the electrode can be distinguished between the electrolyte and the carbon cathode corrosion. For the quantifications of Li_2CO_3 in the carbon cathode, both carbon cathodes discharged (0.5 mAh) with and without 0.2 M DMPO were immersed in acidic solution to selectively decompose Li_2CO_3 in the discharge products to gaseous CO_2.[18] Subsequently, $^{13}CO_2$ and $^{12}CO_2$ were respectively measured by gas analysis, as presented in Figure 4.1e and f. It shows that, in a reference cell without DMPO, the evolution of $^{12}CO_2$ is dominant (1.051 μmol) with only small amount of $^{13}CO_2$ detected (0.016 μmol), indicating that the substantial amount of the byproducts was produced after the discharging and it is originated mostly from the instability of the electrolyte. In contrast, it is noted that the evolution of $^{12}CO_2$ was significantly reduced in the electrode employing DMPO, exhibiting less than a half (0.439 μmol) compared with the reference cell. Moreover, the

evolution of $^{13}CO_2$ was still negligible (0.013 μmol). The suppressed formation of the carbonate byproducts especially containing ^{12}C supports that the electrolyte stability was enhanced in the presence of DMPO, which is attributable to the reduced reactivity of oxygen radicals through the formation of DMPO-O_2^- complex during discharge.

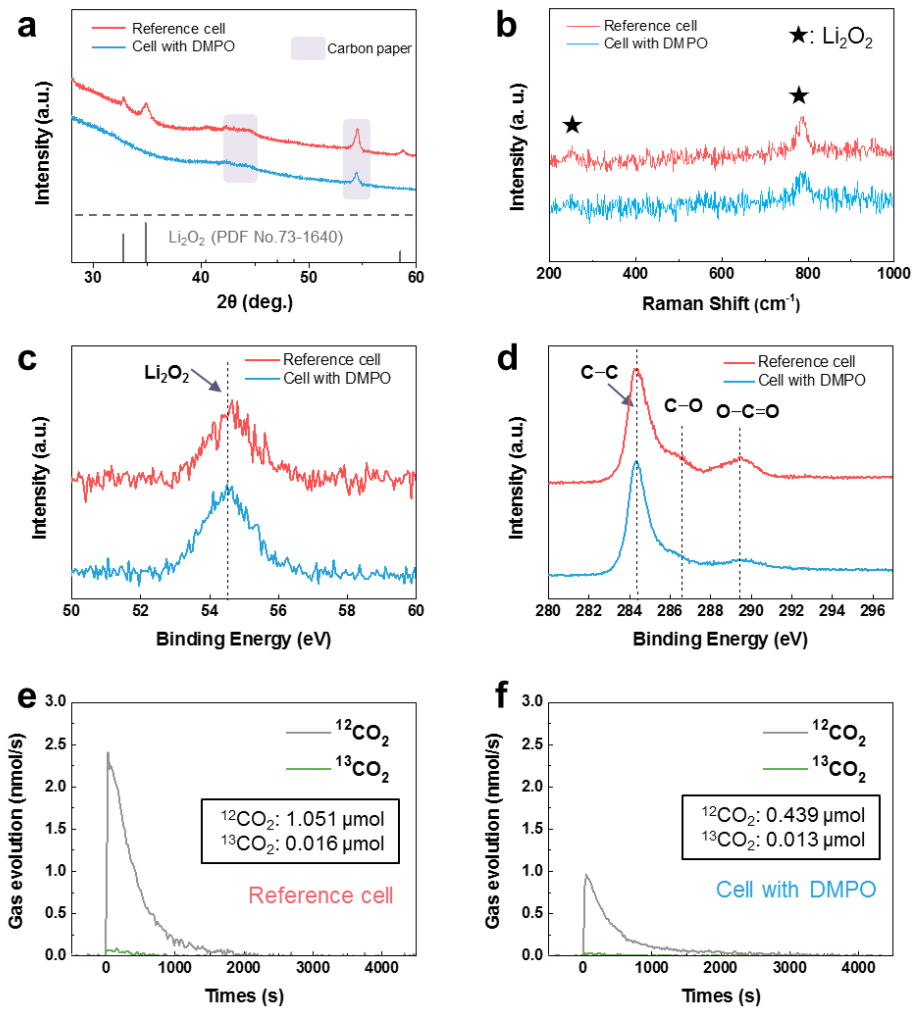

Figure 4.1. (a) XRD and (b) Raman spectra of discharged cathode with and without DMPO. XPS (c) Li 1s and (d) C 1s spectra of discharged cathode with and without DMPO. DEMS analyses with acid treatment on discharged ^{13}C cathode (e) without DMPO and (f) with DMPO.

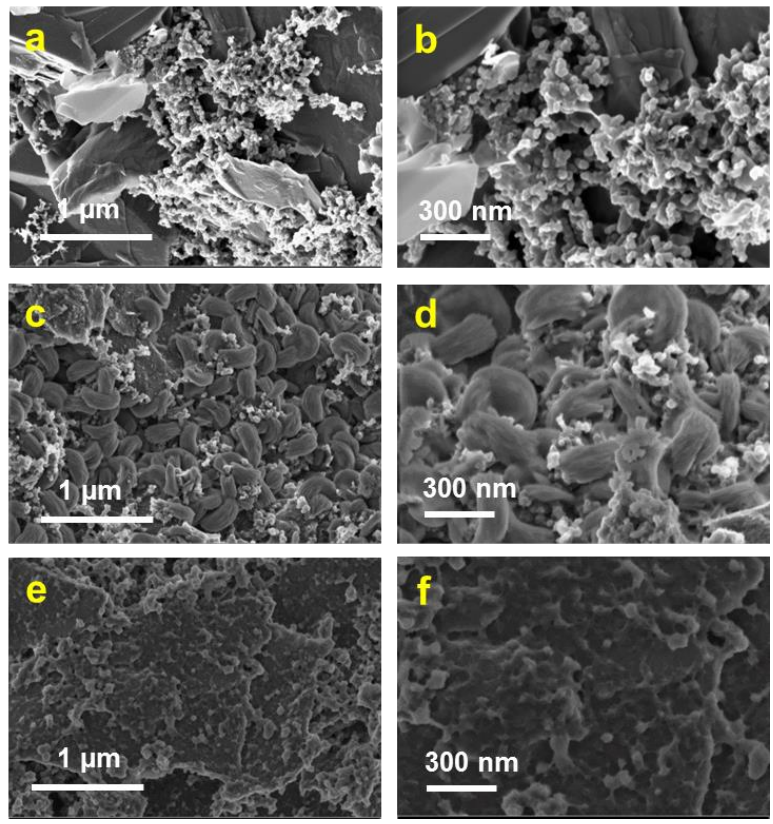

Figure 4.2. SEM images of (a, b) pristine carbon cathode, (c, d) 0.5 mAh discharged carbon cathode without DMPO, and (e, f) 0.5 mAh discharge carbon cathode with DMPO.

4.3.2 Unexpected role of DMPO during charge in Li–O_2 cells

To our surprise, the charge overpotential was significantly reduced, while the DMPO was expected to play a role during the discharge because it captures the oxygen radicals produced during the discharge. In order to elucidate this unexpected result, we carried out several model experiments. In the previous reports, amorphous Li_2O_2 led to lowered charging overpotential compared to crystalline one.[45, 47] In this regard, discharged amorphous Li_2O_2 in the presence of DMPO are expected to be decomposed at reduced charging potential. For the verification of this effect, Li-O_2 cells with and without 0.2 M DMPO were galvanostatically tested for one cycle in Figure 4.3a. The discharge profiles of the two cells are almost identical because the addition of DMPO does not change the electrochemical reaction during discharge in which oxygen molecules are reduced to superoxide radicals. In contrast, the charge profiles of the two cells display clear difference. The charge voltage of the reference cell shows typical increasing curve over 4 V,[16, 17] whereas the DMPO cell displays about 0.5 V lower charge voltage. Although amorphourization of Li_2O_2 bring about lower charge voltage, the 0.5 V difference is huge reduction compared to the 0.1~0.2 V decrease with amorphourization of Li_2O_2 in the previous reports.[45, 47] Therefore, it is highly plausible that there is an unexpected effect of DMPO on charging. To rule out any effects of DMPO during charge, the cathode containing amorphous Li_2O_2 which produced during discharge in DMPO cell was taken out, washed with DME, and reassembled with the reference electrolyte without DMPO into a new cell which

was charged subsequently. The charge profile of the new cell in Figure 4.3b shows ~0.2 V lower charge voltage than that in the reference cell. In comparison with the 0.5 V decrease in charge voltage with DMPO during both the discharge and charge in Figure 4.3a, this results indicate that DMPO reduced charge voltage by not only amorphourization of discharge products but also another mechanism. For the direct comparison of the role of DMPO during charge, another reference cell without DMPO was discharged, and the discharged cathode was washed as above, reassembled with DMPO containing electrolyte, and then charged subsequently. The voltage profile of this cell is compared with that of the reference cell in Figure 4.3c. Even though the discharge products of the two cell were identical, the cell charged with DMPO shows decreased charge voltage, which demonstrates that DMPO apparently affect and facilitate the charge process. Taken together, these data indicate that DMPO lowers charge voltage by forming amorphous Li_2O_2 and through unexpected effective role which will be discussed later.

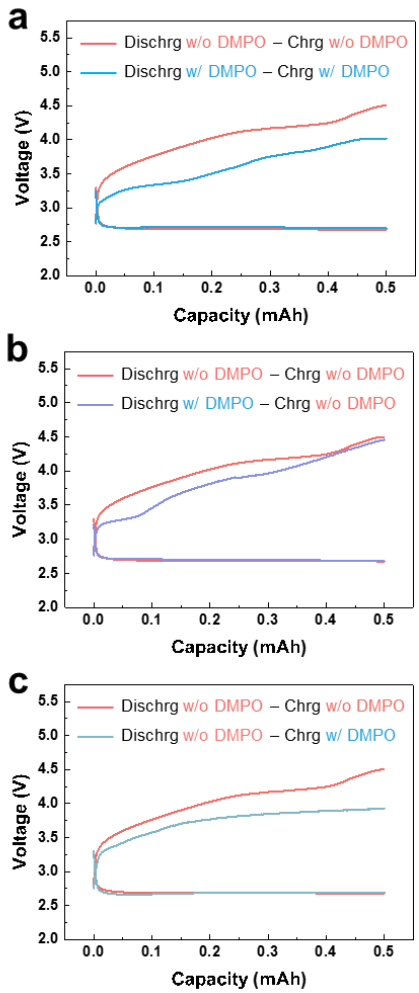

Figure 4.3. First discharge/charge curves of Li-O_2 cells with presence or absence of DMPO during discharge and charge. (a) Discharge and charge without DMPO (red)/Discharge and charge with DMPO (blue) (b) Discharge and charge without DMPO (red)/Discharge with DMPO and charge without DMPO (purple) (c) Discharge and charge without DMPO (red)/Discharge without DMPO and charge with DMPO (light blue)

4.3.3 Visualization of the effect of DMPO during charge in Li–O_2 cells

To visualize the effect of DMPO during charge, SEM images were observed at the various states of charge in the Li-O_2 cells with and without 0.2 M DMPO. The initial state is 0.5 mAh discharged carbon cathode in reference cell which displays the toroidal morphology in Figure 4.4a and g. The well-defined toroidal morphology was selected as the initial state for the clear comparison of the charged states for the two cases. The sizes of toroidal Li_2O_2 were almost unchanged until 0.015 mAh regardless of the presence of DMPO in Figure 4.4b and h. After charged to 0.05 mAh with DMPO in Figure 4.4c, toroidal Li_2O_2 were effectively and homogeneously decomposed and some of them showed plate like morphology, whereas the toroidal morphology was well maintained in the reference electrolyte without DMPO in Figure 4.4i. After charged to 0.1 and 0.2 mAh, even though the sizes of Li_2O_2 gradually decreased with charging in both cases (Figure 4.4d and e for DMPO cell, Figure 4.4j and k for reference cell), charging with DMPO showed more efficient and homogeneous decomposition of Li_2O_2, which hint at the effective role of freely-mobile DMPO on charging process. After the end of charging at 0.5 mAh, both the cathodes showed clear disappearance of discharge products (Figure 4.4f and l).

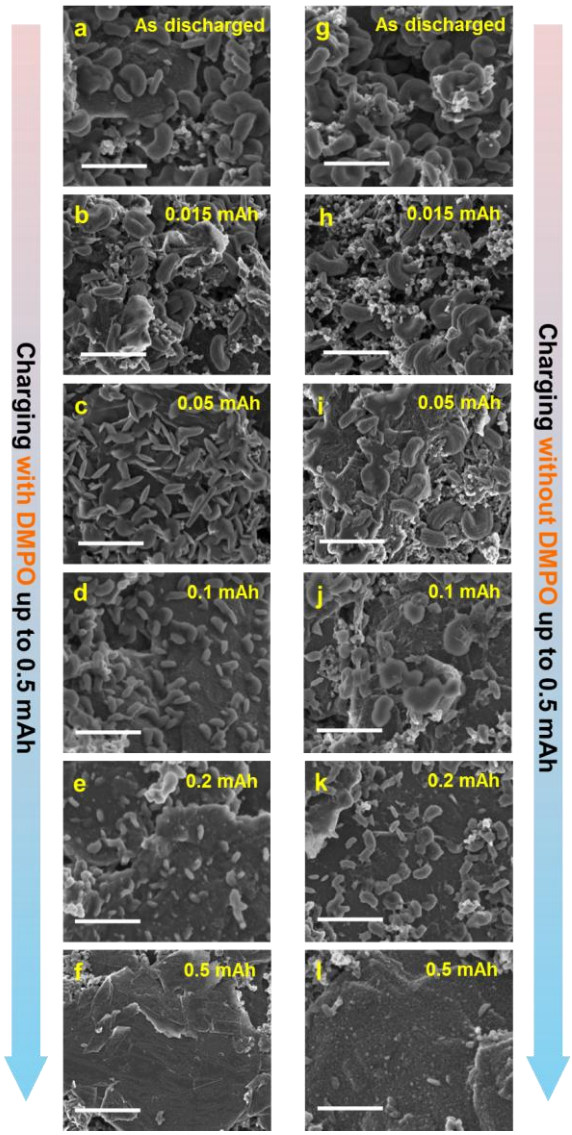

Figure 4.4. SEM images of carbon cathode on various state of charge with and without DMPO. (a, g) 0.5 mAh discharged cathode without DMPO. (b-f) 0.015, 0.05, 0.1, 0.2, and 0.5 mAh charged cathode with DMPO, respectively. (h-l) 0.015, 0.05, 0.1, 0.2, and 0.5 mAh charged cathode without DMPO, respectively. Scale bar: 1 μm.

4.3.4 Reaction mechanism of DMPO during discharge and charge in Li–O_2 cells

To further understand the working mechanism of DMPO during discharge and charge, EPR analyses were conducted. After discharge to 0.1, 0.2, 0.3, 0.4, and 0.5 mAh in DMPO cells, each cell was disassembled and the electrolytes in the cells were extracted to be analyzed with EPR. Figure 4.5a presents the EPR spectra of each discharged electrolyte and confirms the formation of DMPO-O_2^- complex during discharge. At the early discharge states until 0.3 mAh, the six pairs of characteristic peaks of DMPO-O_2^- which were marked with inverted triangles (▼) increased as the discharge progressed. At discharged states of 0.4 and 0.5 mAh, the intensities of peaks were almost unchanged with that at discharged state of 0.3 mAh, which is attributable to that the concentration of DMPO-O_2^- was saturated at the discharge state. These EPR spectra clearly demonstrate the formation of DMPO-O_2^- in electrolyte during discharge, which resulted in the formation of amorphous Li_2O_2 and stabilization of discharge process as discussed in Figure 4.1. Similar EPR analyses were conducted after charge to verify the charging mechanism with DMPO. Before the charging, a discharge process (to 0.5 mAh) was preceded in reference cells as shown in Figure 4.4a and g for the comparison study between the SEM and EPR results. The carbon cathodes accommodating toroidal Li_2O_2 were extracted from the cell, washed with DME, and reassembled into new cells with 0.2 M DMPO containing reference electrolyte. Subsequently, each cell was charged to 0.015, 0.05,

0.2, and 0.5 mAh, and the remaining electrolytes in the cells were analyzed with EPR. To exclude the signatures of DMPO-O_2^- from residual superoxide after the discharge, a separate cell without charging was prepared and disassembled after 5 hours of resting. Figure 4.5b displays the EPR spectra of rested electrolyte and each charged electrolyte. For the rested electrolyte, although the intensity of peaks were vague, the characteristic peaks of DMPO-O_2^- still existed, which implies the presence of superoxide radical in discharge product. After charged to 0.015 mAh, which corresponds to the SEM image in Figure 4.4b, the peak intensity of DMPO-O_2^- was almost the same as that in rested sample. In contrast, the peak of DMPO-O_2^- suddenly increased after charged to 0.05 mAh which corresponds to the SEM image in Figure 4.4c. This increased DMPO-O_2^- peak was maintained after the middle of the charge state (0.2 mAh) which corresponds to the SEM image in Figure 4.4e. After charging to the end (0.5 mAh), the DMPO-O_2^- peak was largely reduced and returned to the initial rest state, and this result hint at that soluble DMPO-O_2^- can recover to initial state of DMPO to evolve oxygen during charge, which was further demonstrated in Figure 4.5d and Figure 4.7b. These EPR spectra proved that superoxide radicals were generated during not only discharge but also charge. While the presence of superoxides during the discharge has been observed in many previous reports, this is the first direct observation of the superoxide radicals, and clarifies the charging mechanisms. Nevertheless, it is not yet clear whether the formation of the superoxide radicals is intrinsic in the general Li-O_2 reactions or were induced by the presence of the DMPO in the cell. Interestingly, there was negligible DMPO-O_2^-

peak after charge to 0.015 mAh, and the corresponding SEM images in Figure 4.4b showed toroidal Li_2O_2 which is similar to the morphology without DMPO in Figure 4.4h. With the appearance of DMPO-O_2^- signal after charge to 0.05 mAh, the corresponding morphology was notably changed as discussed in Figure 4.4c and i, and this phenomenon continued to be observed in the subsequent charging. It proposes that the capturing of superoxide radical by DMPO during charge is relevant to the homogeneous decomposition of Li_2O_2. For the decomposition of crystalline toroidal Li_2O_2 which is insulating, it is known that surface delithiation occurs first to form defective $Li_{2-x}O_2$ because surface delithiation reaction is relatively easier to take place than electrically charging crystalline Li_2O_2.[48, 49] The defective $Li_{2-x}O_2$ after surface delithiation contains both superoxide and peroxide component. Therefore, superoxide radical in $Li_{2-x}O_2$ can be captured by DMPO in the electrolyte to form DMPO-O_2^- complex which was observed in Figure 4.5b during charge. Because the DMPO in the electrolyte extract superoxide component from discharge products during charge, the charge reaction sites becomes solid-liquid interface between carbon cathode and soluble DMPO-O_2^-, not solid-solid interface between carbon cathode and Li_2O_2 which is main reaction site in typical Li-O_2 batteries.[50] Therefore, homogeneous decomposition of discharge products during charge can be possible as presented in Figure 4.4c-e with the help of DMPO and the solid-liquid interfaces. In contrast, the cell without DMPO showed inhomogeneous Li_2O_2 decomposition during charge as shown in Figure 4.4i-k because the reaction sites are confined to only solid-solid interfaces. In addition to the homogeneous decomposition, the

overall sizes of Li_2O_2 particles during charge with DMPO (Figure 4.4c-e) were smaller than those without DMPO (Figure 4.4i-k), which shows effective decomposition of discharge products. This is because superoxide component are subtracted from discharge products by DMPO during charge, and exists as DMPO-O_2^- in electrolyte.

For the clear demonstration on the effect of DMPO on the electrochemical reaction during discharge and charge in Li-O_2 cell, CV tests in three electrode system were conducted as presented in Figure 4.5c and d. $Ag/AgNO_3$, Pt wire, and gold electrode were used as reference, counter, and working electrode, respectively, and 1 M tetrabutyl ammonium bis (trifluoromethanesulfonyl) imide (TBATFSI) in TEGDME with and without 0.2 M DMPO were used as electrolyte, respectively. Figure 4.5c displays the CV curves in the three electrode cell without DMPO under Ar and O_2 atmosphere, respectively. In Ar atmosphere, there was no electrochemical reaction in the voltage range from 1.8 V to 4.5 V. On the contrary, the oxygen reduction reaction (ORR) and corresponding oxygen evolution reaction (OER) were observed with peak current at 1.88 and 2.25 V, respectively, in the presence of O_2, which was similar to the previous reports.[51, 52] In the case of CV curves with DMPO, there is no electrochemical reaction under Ar atmosphere in the voltage range from 1.8 V to 4.0 V, whereas oxidation reaction of DMPO was observed above 4.0 V, and once oxidation reaction occur, corresponding reduction reaction also take place under 2.5 V (Figure 4.6). Therefore, the voltage range for CV scan with DMPO was set from 1.8 V to 4.0 V. Under O_2 atmosphere with DMPO, the ORR was observed with peak

current at 1.88 V which is same to the case without DMPO, which demonstrates that the electrochemical reaction during discharge producing superoxide radical does not change with the addition of DMPO. However, the reversible OER with peak current at 2.21 V was negligible compared to the case without DMPO, which evinces that most of superoxide radicals produced during ORR react with DMPO to form DMPO-O_2^- complex, resulting in trivial peak current of corresponding OER. The DMPO-O_2^- complex was then oxidized above 2.5 V and these DMPO-O_2^- oxidation is relevant to the unexpected low charge voltage in Figure 4.3. The stable cycling behavior of the CV curves with DMPO under O_2 atmosphere for 100 cycles in Figure 4.6c proved that the DMPO-O_2^- complex recovers to the initial state of DMPO evolving O_2 after oxidation.

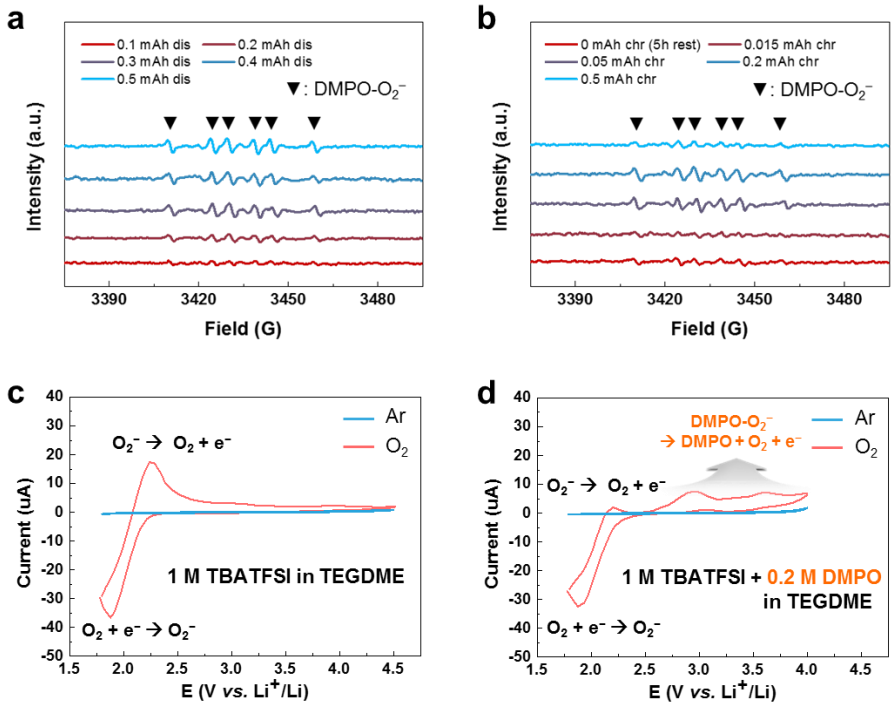

Figure 4.5. (a) EPR analyses after discharge to 0.1, 0.2, 0.3, 0.4, and 0.5 mAh with DMPO. (b) EPR analyses after charge the discharged cathode without DMPO (0.5 mAh) to 0 (5h rest), 0.015, 0.05, 0.2, and 0.5 mAh with DMPO. All the EPR analyses were conducted using the electrolytes in the cells. (c) CV curves in Ar and O_2 atmosphere using 1 M TBATFSI in TEGDME as the electrolyte (without DMPO). (d) CV curves in Ar and O_2 atmosphere using 1 M TBATFSI + 0.2 M DMPO in TEGDME as the electrolyte (with DMPO).

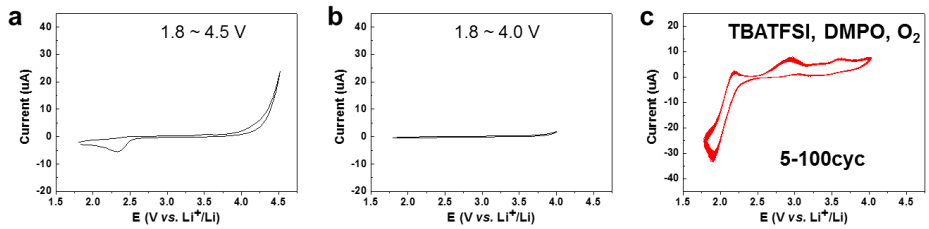

Figure 4.6. (a, b) CV curves in Ar atmosphere using 1 M TBATFSI + 0.2 M DMPO in TEGDME as the electrolyte with 1.8~4.5 V and 1.8~4.0 V voltage scans, respectively. (c) CV curves in O_2 atmosphere using 1 M TBATFSI + 0.2 M DMPO in TEGDME as the electrolyte for 100 cycles.

4.3.5 Gas analyses in Li–O_2 cells with and without DMPO and corresponding cycle stability

In order to further demonstrate the stabilizing effect of DMPO, gas analyses during charge using DEMS were conducted in Li-O_2 cell with and without DMPO. For the distinction between degradation from electrolyte and carbon, ^{13}C was used as the carbon cathode for DEMS analyses. In Figure 4.7a and b, the evolution of O_2, $^{12}CO_2$, and $^{13}CO_2$ corresponded to red, gray, and sky-blue lines, respectively, and purple line represented charge voltage. The amounts of each evolved gas were presented in supporting information. The Li-O_2 cell without DMPO in Figure 4.7a showed typical "M"-shaped O_2 evolution along with $^{12}CO_2$ and $^{13}CO_2$ evolution increasing from the middle of charge state.[17, 48] In contrast, the Li-O_2 cell with DMPO in Figure 4.7b presented increased O_2 evolution and decreased $^{12}CO_2$ and $^{13}CO_2$ evolution, proving the effect of DMPO suppressing side reactions in Li-O_2 cell. Unlike the results in Figure 4.1e which presented negligible evolution of $^{13}CO_2$ from discharge products without DMPO, the DEMS results in Figure 4.7a showed the $^{13}CO_2$ evolution during charge, which corresponds to the previous research by Thotiyl et al., and indicates that carbon degradation is severe with intermediates of Li_2O_2 on oxidation.[18] The electrolyte decomposition is also affected by the intermediates during charge,[17, 18, 48] resulting in larger amount of $^{12}CO_2$ evolution (1.454 μmol) during charge in Figure 4.7a than that (1.051 μmol) after discharge in Figure 4.1e. Considering the residual Li_2CO_3 in cathode after charge,[18] the side

reactions in electrolyte during charge can be more severe. The intermediates of Li_2O_2 on oxidation involve superoxide radical, and this superoxide radical can be captured by DMPO in electrolyte during charge as discussed in Figure 4.5b. The capturing and stabilization of reactive superoxide radical by DMPO during charge finally led to the reduced amount of both $^{12}CO_2$ and $^{13}CO_2$ in the Li-O_2 cell with DMPO (Figure 4.7b). Combining the gas analyses results in Figure 4.1 and Figure 4.7, DMPO stabilizes not only the discharge process, but also the charge process in Li-O_2 battery, acting as dual functioning superoxide carrier.

The cycle stabilities of Li-O_2 cells with and without DMPO were also evaluated to validate the effect of DMPO in a practical Li-O_2 cell. For the cycle test, the hierarchical-fibril CNT was used as carbon air-electrode.[32-34] Without DMPO in Figure 4.7c, the Li-O_2 cell showed discharge voltages around 2.6 V and increasing charge voltages over 4 V, and finally 4.5 V at the end of charge for first 50 cycles. In the case of Li-O_2 cell with 0.2 M DMPO (Figure 4.7d), the discharge voltages around 2.6 V were similar to those of the cell without DMPO. On the other hand, the charge voltages were distinctly lowered under 3.8 V for the first 50 cycles with the aid of amorphourized discharge product and low oxidation potential of DMPO-O_2^- as discussed earlier. The charge voltage slightly increased to 4.0 V after 100 cycles presenting better cycle stability compared to the cell without DMPO which showed largely reduced discharge and charge capacity after 100 cycles. Finally, for the demonstration of the effect of DMPO concentration, discharge/charge voltage profiles for 100 cycles of Li-O_2 cell with 0.5 M DMPO were shown in Figure 4.7e.

The discharge voltages around 2.6 V were well maintained, whereas the charge voltages for the first 50 cycles were further lowered under 3.6 V and charge voltage below 3.8 V was observed after 100 cycles. These distinctly reduced charge overpotentials with 0.5 M DMPO were probably resulted from the increased concentration of DMPO-O_2^- during charge. The concentration of DMPO-O_2^- during charge can be higher with higher DMPO concentration, because the probability that superoxide radicals meet with DMPO and form DMPO-O_2^- is increased as the concentration of DMPO is higher. This high DMPO-O_2^- concentration can lead to low charge voltage with low concentration polarization as shown in Figure 4.7e. The effects of various DMPO concentration were further discussed in Figure 4.8. With the increased cycle stability, the cell with 0.2 M and 0.5 M DMPO stably operated over 200 and 240 cycles, respectively, while the reference cell without DMPO operated only 80 cycles (Figure 4.7f).

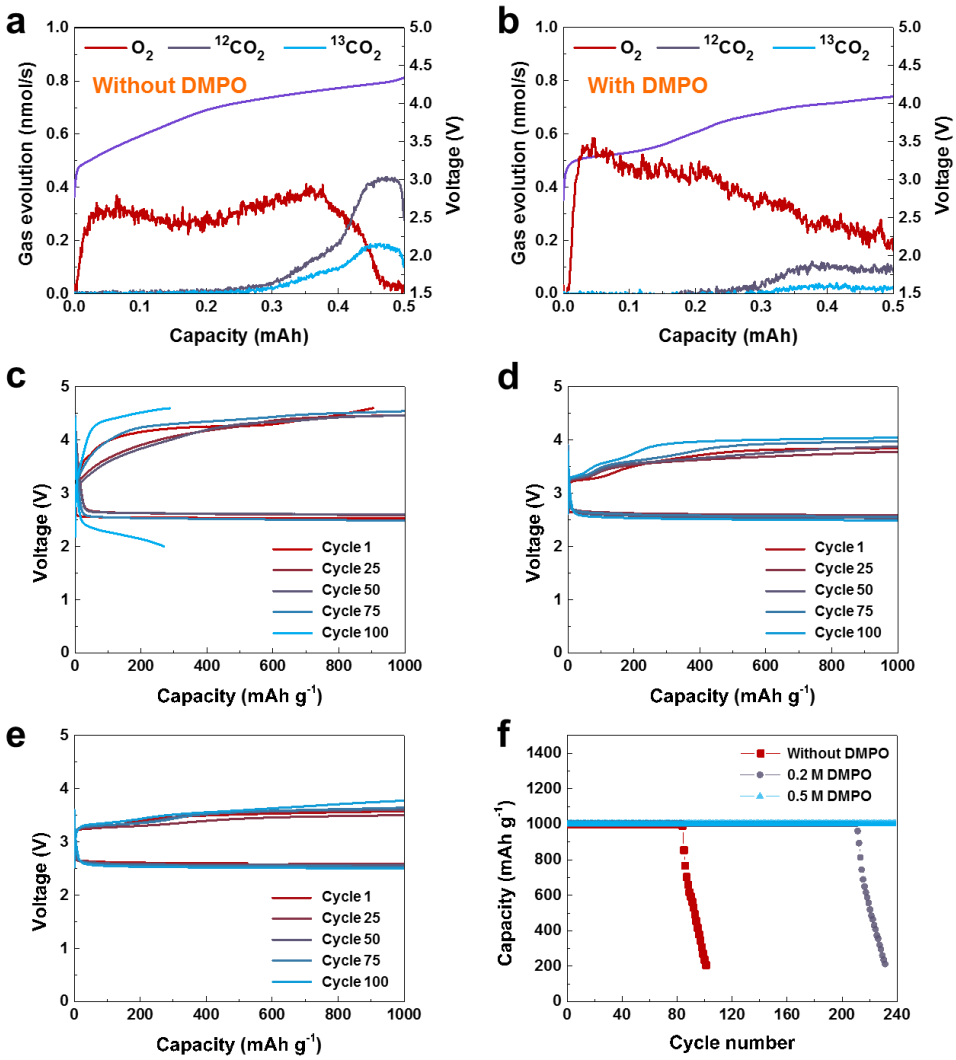

Figure 4.7. DEMS analyses of the Li-O_2 cells using ^{13}C as the carbon cathodes (a) without DMPO and (b) with 0.2 M DMPO, respectively. Discharge/Charge voltage profiles of Li-O_2 cells using hierarchical CNT as the carbon cathodes with (c) 0 M, (d) 0.2 M, and (e) 0.5 M DMPO, respectively. (f) Cycle stabilities of the Li-O_2 cells with 0 M, 0.2 M, and 0.5 M DMPO.

Table 4.1. The amounts of evolved gas in DEMS analyses during charge with and without DMPO.

	With DMPO (μmol)	Without DMPO (μmol)
O_2	3.916	5.275
$^{12}CO_2$	1.454	0.474
$^{13}CO_2$	0.657	0.093

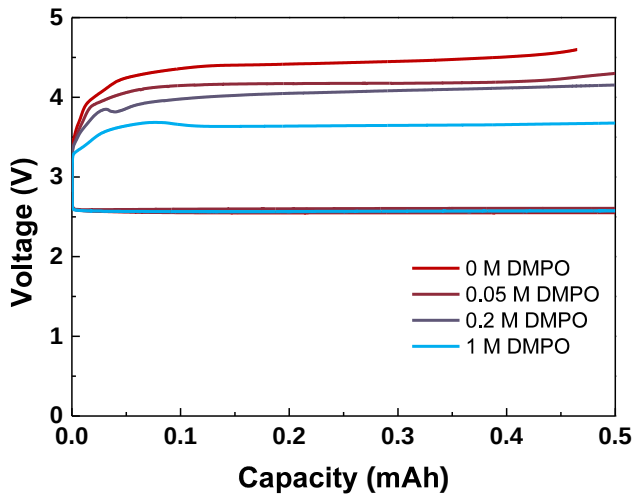

Figure 4.8. Discharge/Charge voltage profiles of Li-O_2 cells using P50 as the carbon cathode with various concentrations of DMPO.

4.4 Concluding remarks

In this study, we demonstrated that regulating the reactivity of radical species can alleviate side reactions in a Li–O_2 cell. By employing a dual-functioning DMPO molecule, it was shown that the reversible formation of an intermediate complex, DMPO–O_2^-, in the presence of superoxide radicals could remarkably mitigate the reactivity of radical species produced in the Li–O_2 cell, thus improving the cycle stability. EPR and *in situ* DEMS analyses revealed that the superoxide radicals were present during both the discharge and charge processes, and the capture of superoxide radicals by DMPO led to the reduction of side reactions in the electrolyte and carbon-based air electrode. It was also observed that the addition of DMPO to the Li–O_2 cell altered the electrochemical reaction between lithium and oxygen by forming an intermediate DMPO–O_2^- complex, which resulted in not only stabilization of the radical species but also amorphization of the discharge product. Moreover, the DMPO could scavenge superoxide components in the discharge product by forming DMPO–O_2^-, which could stabilize and kinetically facilitate the charge process. The combined radical mediation and scavenging of superoxides resulted in extended cycle stability of a practical Li–O_2 cell employing DMPO. This work demonstrates the importance of controlling the reactivity of radical species. We propose that the radical-stabilizing molecules can serve as a new platform for the realization of stable and efficient Li–O_2 batteries, urging further community effort toward the development of other superoxide carriers.

4.5 References

[1] M. D. Bhatt, H. Geaney, M. Nolan, C. O'Dwyer, *Phys. Chem. Chem. Phys.* **2014**, 16, 12093.

[2] P. G. Bruce, S. A. Freunberger, L. J. Hardwick, J.-M. Tarascon, *Nat. Mater.* **2012**, 11, 19.

[3] H.-D. Lim, B. Lee, Y. Bae, H. Park, Y. Ko, H. Kim, J. Kim, K. Kang, *Chem. Soc. Rev.* **2017**, 46, 2873.

[4] Z. W. Chang, J. J. Xu, Q. C. Liu, L. Li, X. b. Zhang, *Adv. Energy Mater.* **2015**, 5, 1500633.

[5] V. S. Bryantsev, V. Giordani, W. Walker, M. Blanco, S. Zecevic, K. Sasaki, J. Uddin, D. Addison, G. V. Chase, *J. Phys. Chem. A* **2011**, 115, 12399.

[6] R. Cao, E. D. Walter, W. Xu, E. N. Nasybulin, P. Bhattacharya, M. E. Bowden, M. H. Engelhard, J. G. Zhang, *ChemSusChem* **2014**, 7, 2436.

[7] D. Aurbach, B. D. McCloskey, L. F. Nazar, P. G. Bruce, *Nat. Energy* **2016**, 1, 16128.

[8] L. Johnson, C. Li, Z. Liu, Y. Chen, S. A. Freunberger, P. C. Ashok, B. B. Praveen, K. Dholakia, J.-M. Tarascon, P. G. Bruce, *Nat. Chem.* **2014**, 6, 1091.

[9] S. A. Freunberger, Y. Chen, N. E. Drewett, L. J. Hardwick, F. Bardé, P. G. Bruce, *Angew. Chem., Int. Ed.* **2011**, 50, 8609.

[10] X. Yao, Q. Dong, Q. Cheng, D. Wang, *Angew. Chem., Int. Ed.* **2016**, 55, 11344.

[11] V. S. Bryantsev and M. Blanco, *J. Phys. Chem. Lett.* **2011**, 2, 379.

[12] V. S. Bryantsev, *Chem. Phys. Lett.* **2013**, 558, 42.

[13] V. S. Bryantsev, J. Uddin, V. Giordani, W. Walker, D. Addison, G. V. Chase, *J. Electrochem. Soc.* **2013**, 160, A160.

[14] A. Khetan, A. Luntz, V. Viswanathan, *J. Phys. Chem. Lett.* **2015**, 6, 1254.

[15] A. Khetan, H. Pitsch, V. Viswanathan, *J. Phys. Chem. Lett.* **2014**, 5, 2419.

[16] Y. Bae, D.-H. Ko, S. Lee, H.-D. Lim, Y.-J. Kim, H.-S. Shim, H. Park, Y. Ko, S. K. Park, H. J. Kwon, H. Kim, H.-T. Kim, Y.-S. Min, D. Im, K. Kang, *Adv. Energy Mater.* **2018**, 8, 1702661.

[17] Y. Bae, Y. S. Yun, H.-D. Lim, H. Lee, Y.-J. Kim, J. Kim, H. Park, Y. Ko, S. Lee, H. J. Kwon, H. Kim, H.-T. Kim, D. Im, K. Kang, *Chem. Mater.* **2016**, 28, 8160.

[18] M. M. Ottakam Thotiyl, S. A. Freunberger, Z. Peng, P. G. Bruce, *J. Am. Chem. Soc.* **2012**, 135, 494.

[19] B. D. McCloskey, A. Speidel, R. Scheffler, D. Miller, V. Viswanathan, J. Hummelshøj, J. Nørskov, A. Luntz, *J. Phys. Chem. Lett.* **2012**, 3, 997.

[20] D. M. Itkis, D. A. Semenenko, E. Y. Kataev, A. I. Belova, V. S. Neudachina, A. P. Sirotina, M. Hävecker, D. Teschner, A. Knop-Gericke, P. Dudin, A. Barinov, E. A. Goodilin, Y. Shao-Horn, L. V. Yashina, *Nano Lett.* **2013**, 13, 4697.

[21] D. Sharon, P. Sharon, D. Hirshberg, M. Salama, M. Afri, L. J. Shimon, W.-J. Kwak, Y.-K. Sun, A. A. Frimer, D. Aurbach, *J. Am. Chem. Soc.* **2017**, 139,

11690.

[22] B. D. Adams, R. Black, Z. Williams, R. Fernandes, M. Cuisinier, E. J. Berg, P. Novak, G. K. Murphy, L. F. Nazar, *Adv. Energy Mater.* **2015**, 5, 1400867.

[23] Z. Huang, H. Zeng, M. Xie, X. Lin, Z. Huang, Y. Shen, Y. Huang, *Angew. Chem.* **2019**, 131, 2367.

[24] A. Khetan, H. Pitsch, V. Viswanathan, *J. Phys. Chem. Lett.* **2014**, 5, 1318.

[25] W.-J. Kwak, H.-G. Jung, S.-H. Lee, J.-B. Park, D. Aurbach, Y.-K. Sun, *J. Power Sources* **2016**, 311, 49.

[26] M. M. O. Thotiyl, S. A. Freunberger, Z. Peng, Y. Chen, Z. Liu, P. G. Bruce, *Nat. Mater.* **2013**, 12, 1050.

[27] Z. Peng, S. A. Freunberger, Y. Chen, P. G. Bruce, *Science* **2012**, 1223985.

[28] S. J. Kang, T. Mori, S. Narizuka, W. Wilcke, H.-C. Kim, *Nat. Commun.* **2014**, 5, 3937.

[29] J. Xie, X. Yao, Q. Cheng, I. P. Madden, P. Dornath, C. C. Chang, W. Fan, D. Wang, *Angew. Chem., Int. Ed.* **2015**, 54, 4299.

[30] W.-H. Ryu, T.-H. Yoon, S. H. Song, S. Jeon, Y.-J. Park, I.-D. Kim, *Nano Lett.* **2013**, 13, 4190.

[31] R. Mi, H. Liu, H. Wang, K.-W. Wong, J. Mei, Y. Chen, W.-M. Lau, H. Yan, *Carbon* **2014**, 67, 744.

[32] H. D. Lim, H. Song, J. Kim, H. Gwon, Y. Bae, K. Y. Park, J. Hong, H. Kim, T. Kim, Y. H. Kim, X. Lepró, R. Ovalle-Robles, R. H. Baughman, K. Kang, *Angew. Chem.* **2014**, 126, 4007.

[33] H.-D. Lim, H. Song, H. Gwon, K.-Y. Park, J. Kim, Y. Bae, H. Kim, S.-K. Jung, T. Kim, Y. H. Kim, X. Lepró, R. Ovalle-Robles, R. H. Baughman, K. Kang, *Energy Environ. Sci.* **2013**, 6, 3570.

[34] H. D. Lim, K. Y. Park, H. Song, E. Y. Jang, H. Gwon, J. Kim, Y. H. Kim, M. D. Lima, R. Ovalle-Robles, X. Lepró, R. H. Baughman, K. Kang, *Adv. Mater.* **2013**, 25, 1348.

[35] W.-H. Ryu, F. S. Gittleson, J. M. Thomsen, J. Li, M. J. Schwab, G. W. Brudvig, A. D. Taylor, *Nat. Commun.* **2016**, 7, 12925.

[36] D. Sun, Y. Shen, W. Zhang, L. Yu, Z. Yi, W. Yin, D. Wang, Y. Huang, J. Wang, D. Wang, *J. Am. Chem. Soc.* **2014**, 136, 8941.

[37] M. Kohno, Y. Mizuta, M. Kusai, T. Masumizu, K. Makino, *Bull. Chem. Soc. Jpn.* **1994**, 67, 1085.

[38] A. Samuni, A. Samuni, H. M. Swartz, *Free Radical Biol. Med.* **1989**, 6, 179.

[39] V. A. E. Barrios, A. Jasso-Salcedo, N. Cervantes-Rincón, D. V. S. Rodríguez: 'Modified Metallic Oxides for Efficient Photocatalysis', in 'Photocatalyst', 2018, IntechOpen.

[40] C. Xia, R. Fernandes, F. H. Cho, N. Sudhakar, B. Buonacorsi, S. Walker, M. Xu, J. Baugh, L. F. Nazar, *J. Am. Chem. Soc.* **2016**, 138, 11219.

[41] L. Zhu, H. Li, Z. Liu, P. Xia, Y. Xie, D. Xiong, *J. Phys. Chem. C* **2018**, 122, 9531.

[42] L. Basumallick, J. A. Ji, N. Naber, Y. J. Wang, *J. Pharm. Sci.* **2009**, 98, 2464.

[43] D. L. Haire, U. M. Oehler, H. D. Goldman, R. L. Dudley, E. G. Janzen, *Can.*

J. Chem. **1988**, 66, 2395.

[44] E. Yilmaz, C. Yogi, K. Yamanaka, T. Ohta, H. R. Byon, *Nano Lett.* **2013**, 13, 4679.

[45] B. D. Adams, C. Radtke, R. Black, M. L. Trudeau, K. Zaghib, L. F. Nazar, *Energy Environ. Sci.* **2013**, 6, 1772.

[46] X. Gao, Y. Chen, L. Johnson, P. G. Bruce, *Nat. Mater.* **2016**, 15, 882.

[47] Y. Zhang, Q. Cui, X. Zhang, W. C. McKee, Y. Xu, S. Ling, H. Li, G. Zhong, Y. Yang, Z. Peng, *Angew. Chem., Int. Ed.* **2016**, 55, 10717.

[48] S. Kang, Y. Mo, S. P. Ong, G. Ceder, *Chem. Mater.* **2013**, 25, 3328.

[49] S. Ganapathy, B. D. Adams, G. Stenou, M. S. Anastasaki, K. Goubitz, X.-F. Miao, L. F. Nazar, M. Wagemaker, *J. Am. Chem. Soc.* **2014**, 136, 16335.

[50] Z. Chang, J. Xu, X. Zhang, *Adv. Energy Mater.* **2017**, 7, 1700875.

[51] X. Gao, Z. P. Jovanov, Y. Chen, L. R. Johnson, P. G. Bruce, *Angew. Chem.* **2017**, 129, 6639.

[52] W. Yin, A. Grimaud, F. Lepoivre, C. Yang, J. M. Tarascon, *J. Phys. Chem. Lett.* **2016**, 8, 214.

Chapter 5. Conclusion

Li-O_2 batteries, which can deliver much higher energy densities than current Li-ion batteries, have attracted considerable attention as a potential alternative chemistry for electric vehicles (EV). However, poor reversibility and efficiency remained as hurdle for the commercialization of Li-O_2 batteries, which mainly caused by parasitic reaction of discharge products with electrolyte and carbon cathode during discharge and charge. In this thesis, I proposed the methods for reducing these side reactions in three ways.

At first, I demonstrate that the defect site on carbon material is the main reason of the carbon degradation and can be an anchor for the decomposition of electrolyte during cycling of Li-O_2 cells. Through the heat treatment of ^{13}C, the crystallinity and defectiveness of carbon materials were controlled. With extremely low content of defect sites in carbon cathode, Li-O_2 cell showed negligible carbon degradation during first charge. In clear contrast, Li-O_2 cell with defective carbon cathode presented large amount of carbon degradation during first charge. With increasing number of cycles, these phenomena become more severe. The O_2 evolutions are distinctively reduced whereas $^{12}CO_2$ and $^{13}CO_2$ evolutions are enlarged in defective carbon cathode after several cycling. On the other hand, O_2, $^{12}CO_2$, and $^{13}CO_2$ evolutions in heat treated carbon cathode remain almost constant compared to the case of defective carbon cathode. With these improved stability of carbon cathode and electrolyte, the Li-O_2 cell with heat treated carbon cathode

showed three-times increased cycle stability.

Second, I focused on the defect sites on the carbon surface, because reactive discharge products are produced on the surface of carbon cathode at which electron transfer take places. Therefore, the effective method to reduce the instability of defect site on carbon surface was developed. ALD method which selectively deposits coating materials on the defect sites of carbon materials is thus great tool for the defect shielding. ZnO was chosen for coating material because its electric conductivity is relatively high and it does not have any catalytic effect on Li-O_2 chemistry. With ZnO coating, O_2 evolution increased and $^{12}CO_2$ and $^{13}CO_2$ evolutions decreased distinctively, which also remained with cycling. Furthermore, XPS analyses demonstrated that carbonate formation in carbon cathode is significantly reduced with ZnO coating, which is well matched with DEMS analyses. Enhanced oxygen efficiency and reduced side reactions in electrolyte and carbon cathode with ZnO coating led to improved cycle stability over 100 cycles. Nevertheless, ZnO coatings on carbon cathode were detached during cycling, which deteriorate the shielding effect of ZnO, finally resulting in cell failure.

At last, superoxide radical, one of the main causes of parasitic reactions in Li-O_2 batteries was thoroughly deactivated by forming stable radical complex with DMPO. With the addition of DMPO in Li-O_2 cells, side reactions in electrolyte and carbon cathode were effectively reduced, along with unexpected low charge overpotential. By EPR and CV analyses, it was found that DMPO extract superoxide radical in $Li_{2-x}O_2$ during charge, forming DMPO-O_2^- complex which can oxidized at

relatively low charge potential. DMPO stabilized not only the discharge process, but also the charge process by forming DMPO-O_2^- complex, which demonstrate dual-functionality of DMPO in Li-O_2 batteries.

Chapter 6. Abstract in Korean

초 록

최근 전기자동차용 전지와 같은 고 용량 에너지 저장 시스템에 대한 수요가 폭발적으로 증가하고 있다. 기존의 리튬 이온 전지는 현재까지 소형 전자기기용으로 성공적인 모습을 보여줬지만 양극 구조 내에 무거운 전위금속을 가지고 있고 리튬 저장 공간이 한정적이기 때문에 전기 자동차에 필요한 높은 에너지 밀도를 가지기엔 한계가 있다. 이를 해결하기 위해 높은 에너지 밀도를 가지는 차세대 이차 전지가 각광받고 있는데 이 중 리튬 공기 전지는 이론 상 3500 Wh/kg 에 해당하는 가장 큰 에너지 밀도를 가지고 있어 전세계에서 많은 연구가 이루어지고 있다. 하지만 충전 시 과전압이 매우 커 에너지 효율이 떨어지고 사이클 안정성이 좋지 않아 상용화하기 위해 해결해야 할 문제점이 많이 남아 있다. 이러한 문제점들은 대부분 방전생성물이 굉장히 반응성이 크기 때문에 나타난다. 대표적으로 방전 시 생성되는 산소 라디칼에 의해 전해질이 분해되고 충전 시에는 반응성이 큰 방전생성물에 고전압 환경이 추가되면서 탄소 전극까지 분해시킨다. 전해질 및 탄소 전극의 부반응을 통해 생성되는 대표적인 부산물로 Li_2CO_3가 있는데 이는 전기 전도도가 낮기 때문에 충방전 시 셀의

과전압을 더욱 향상시킨다. 본 논문에서는 이러한 전해질 및 탄소 부반응을 줄이기 위한 연구를 수행하였고 리튬 공기 전지가 앞으로 나아가야 할 방향을 제시하고자 하였다.

2장에서는 탄소 전극의 부반응이 어디에서 기인하는지 밝히고, 이를 해결하기 위한 방법을 제시하였다. 부반응이 탄소 전극에서 발생하는지 전해질에서 발생하는지 밝히기 위해 탄소 전극을 동위원소 ^{13}C를 사용하였고 2800°C까지의 열처리를 통해 탄소 전극의 결정성을 증가시키고 결함을 감소시켰다. 열처리한 탄소 전극을 사용한 리튬 공기 전지에서 충전 시 탄소에서 발생하는 부반응이 열처리 하지 않은 탄소 전극에 비해 현저히 감소하는 것을 관찰하였고 이를 통해 탄소의 부반응이 탄소의 결함 부분에서 기인하는 것을 알 수 있었다. 사이클이 증가함에 따라 열처리를 하지 않은 전극에서는 전해질 및 탄소의 분해가 급격히 증가하는 것을 관찰할 수 있었는데 열처리를 한 전극에서는 전해질 및 탄소의 분해 정도가 매우 완만히 상승하는 것을 볼 수 있었고, 이를 통해 탄소의 결함 부분이 탄소의 분해 뿐만 아니라 전해질의 분해도 촉진시킨다는 것을 알 수 있었다.

3장에서는 탄소 전극의 결함 중 탄소 표면에 있는 결함에 집중하여 연구를 진행하였다. 방전 생성물들은 전자 전달이 일어나는 탄소의 표면에서 발생하고 최종 방전생성물인 Li_2O_2가 탄소 표면에

쌓이기 때문에 부반응이 일어나는 부분은 대부분 탄소 표면의 결함 부분일 것이라 판단하였다. 탄소 표면의 부반응을 효과적으로 제어하기 위해서 ALD 공정을 통해 ZnO를 탄소 표면에 코팅하였다. ALD 공정은 탄소 표면의 결함 부분에서 증착이 일어나기 때문에 결함 부위에만 선택적으로 코팅이 가능하여 불필요한 코팅에 의한 과도한 전극의 무게 증가를 막을 수 있다는 장점이 있다. ZnO 코팅을 통해 표면의 결함이 방전생성물에 노출되지 않도록 한 결과 충전 시 전해질 및 탄소에 의한 부반응이 크게 감소하는 것을 확인하였고 이에 따라 리튬 공기 전지의 수명이 100 사이클 이상 발현될 수 있었다. 하지만 ZnO 코팅이 충방전 시 탄소 표면에서 떨어져 나오는 것을 관찰하였고 이러한 현상이 결국에는 전지의 수명을 더 이상 늘리지 못하게 하는 것을 확인하였다. 이를 통해 탄소 표면과의 흡착력이 강한 안정적인 코팅 물질이 필요하다는 것을 알 수 있었고, 이 후의 연구 방향을 제시하였다.

4장에서는 전지 내에서 부반응을 일으키는 근본적인 문제점인 초과산화물 라디칼의 반응성 제어에 대한 방법이 제안되었다. 방전생성물 중 하나인 초과산화물 라디칼은 반응성이 매우 커서 전해질과 탄소 분해를 일으키는 주요 원인이기 때문에 이 초과산화물 라디칼의 반응성을 낮추는 것은 리튬 공기 전지의 안정성 향상을 위한 가장 직접적인 방법이라고 볼 수 있다. 이에 본 연구에서는 초과산화물

라디칼과 반응하여 안정적인 형태의 라디칼로 만들어주는 5,5-dimethyl-1-pyrroline-N-oxide (DMPO)를 리튬 공기 전지에 도입하였고 DMPO가 효과적으로 전해질 및 탄소의 부반응을 감소시키는 것을 확인하였다. DMPO는 방전 반응에서 DMPO-O_2^- 복합체를 형성하며 전해질의 분해를 크게 감소시켰고, 충전에서도 동일한 복합체를 형성하며 반응을 촉진시키고 충전전압을 감소시키는 모습을 보이며 방전과 충전 모두에서 안정화 기능을 수행하는 모습을 나타냈다.

주요어: 리튬−공기 전지, 열화 메커니즘, 열처리, 원자층 증착법, 초과산화물 매개체,

학 번: 2014-31063

Curriculum Vitae

Youngjoon Bae

Seoul National University

Department of Materials Science and Engineering

1 Gwanak -ro, Gwanak -gu, Seoul , Republic of Korea

Educational Background

- **Ph. D. Course**

September 2014 – August 2019

Advanced Energy Materials Laboratory

Department of Materials Science and Engineering

Seoul National University | Republic of Korea

(Supervisor: Prof. Kisuk Kang)

- **Master of Science**

March 2012 – February 2014

Advanced Energy Materials Laboratory

Department of Materials Science and Engineering

Seoul National University | Republic of Korea

(Supervisor: Prof. Kisuk Kang)

- **Bachelor of Science**

March 2008 – February 2012

Department of Materials Science and Engineering

Seoul National University | Republic of Korea

Research Interests

Materials science for high-energy rechargeable batteries

Li-O_2 chemistry for extremely high energy density

- Stable and efficient Li-O_2 rechargeable batteries
- Interface chemistry between electrode surface and discharge product
- Degradation of carbon cathode and electrolyte in Li-O_2 batteries
- Electrolytes designs for enhanced Li-O_2 batteries (Superoxide carrier, Redox mediators)
- Solid electrolytes for Li-O_2 batteries
- Inorganic-based protecting layer for stable Li metal batteries

Fundamental studies on the mechanisms of reactions in battery operations

- *In situ* characterizations (Differential electrochemical mass spectroscopy, In situ Raman spectroscopy)
- Electron paramagnetic resonance analyses for radical studies

- Surface and interface study (Electrolyte-electrode interface, SEI, …)

Synthesis of nanomaterials

- Electrospinning
- Atomic layer deposition

Honors and Scholarships

- Korea Federation of Textile Industries Scholarship (2011)

List of Publications

(1) Journals (First author)

† These authors contributed equally.

1) **Youngjoon Bae**, Hyelynn Song, Hee-Dae Lim, Hyeokjun Park, Youngmin Ko, Hyuk Jae Kwon, Chi Huynh, Raquel Ovalle-Robles, Yonghyup Kim, Dongmin Im, Kisuk Kang "Dual-Functioning Molecular Carrier of Superoxide Radicals for Stable and Efficient Lithium-oxygen Batteries", In preparation (2019)
2) **Youngjoon Bae**†, Hyeokjun Park†, Youngmin Ko†, Hyunah Kim†, Sung Kwan Park, Kisuk Kang "Bifunctional oxygen electrocatalysts for lithium-oxygen batteries", *Batteries & Supercaps*, Vol 2, 1-16. (2019)
3) **Youngjoon Bae**, Dong-Hyun Ko, Sunyoung Lee, Hee-Dae Lim, Yun-Jung Kim, Hyun-Soo Shim, Hyeokjun Park, Youngmin Ko, Sung Kwan Park, Hyuk Jae Kwon, Hyunjin Kim, Hee-Tak Kim, Yo-Sep Min, Dongmin Im, Kisuk Kang "

Enhanced Stability of Coated Carbon Electrode for Li–O_2 Batteries and Its Limitations", *Advanced Energy Materials*, Vol 8, 1702661 (2018)

4) **Youngjoon Bae**†, Young Soo Yun†, Hee-Dae Lim, Hongkyung Lee, Yun-Jung Kim, Jinsoo Kim, Hyeokjun Park, Youngmin Ko, Sungho Lee, Hyuk Jae Kwon, Hyunjin Kim, Hee-Tak Kim, Dongmin Im, Kisuk Kang "Tuning the Carbon Crystallinity for Highly Stable Li-O_2 Batteries", *Chemistry of Materials*, Vol 28, pp. 8160-8169. (2016)

5) **Youngjoon Bae**, Hee-Dae Lim, Young Soo Yun, Kisuk Kang "Catalytic Effects of Heteroatom-doped Graphene Nanosheets on the Performance of Li-O_2 Batteries", *Journal of Electrochemical Science and Technology,* Vol 5, pp.49-52. (2014)

(2) Journals (Contributing author)

† These authors contributed equally.

1) Youngmin Ko, Hyeokjun Park, Byungju Lee, **Youngjoon Bae**, Sung Kwan Park, Kisuk Kang "Comparative kinetic study of redox mediators for high-power lithium-oxygen batteries", *Journal of Materials Chemistry A*, Vol 7, 6491-6498. (2019)

2) Youngmin Ko, Hyeokjun Park, Hee-Dae Lim, Byungju Lee, Giyun Kwon, Sechan Lee, **Youngjoon Bae**, Sung Kwan Park, Kisuk Kang "Biological redox mediation in electron transport chain of bacteria for oxygen reduction reaction

catalysts in lithium-oxygen batteries", *Advanced Functional Materials*, Vol 29, 18005623. (2019)

3) Hyeokjun Park, Jinsoo Kim, Myeong Hwan Lee, Sung Kwan Park, Do-hoon Kim, **Youngjoon Bae**, Youngmin Ko, Byungju Lee, Kisuk Kang "Highly durable and stable sodium superoxide in concentrated electrolytes for sodium-oxygen batteries", *Advanced Energy Materials*, Vol 8, 1801760. (2018)
4) Hyeokjun Park, Hee-Dae Lim, Hyung-Kyu Lim, Won Mo Seong, Sehwan Moon, Youngmin Ko, Byungju Lee, **Youngjoon Bae**, Hyungjun Kim, Kisuk Kang "High-efficiency and high-power rechargeable lithium–sulfur dioxide batteries exploiting conventional carbonate-based electrolytes", *Nature Communications*, Vol 8, 14989. (2017)
5) Hee-Dae Lim†, Byungju Lee†, **Youngjoon Bae**, Hyeokjun Park, Youngmin Ko, Haegyeom Kim, Jinsoo Kim, Kisuk Kang "Reaction chemistry in rechargeable Li-O_2 batteries", *Chemical Society Reviews*, Vol 46, pp. 2873-2888. (2017)
6) Hee-Dae Lim†, Young Soo Yun†, Youngmin Ko, **Youngjoon Bae**, Min Yeong Song, Hyeon Ji Yoon, Kisuk Kang, Hyoung-Joon Jin "Three-dimensionally branched carbon nanowebs as air-cathode for redox-mediated Li-O_2 batteries", *Carbon*, Vol 118, pp. 114-119. (2017)
7) Hyunjin Kim, Hyunpyo Lee, Mokwon Kim, **Youngjoon Bae**, WoonJoong Baek, Kwangjin Park, Seongyong Park, Taeyoung Kim, Hyukjae Kwon, Wonsung Choi, Kisuk Kang, Soonchul Kwon, Dongmin Im "Flexible free-standing air electrode with bimodal pore architecture for long-cycling Li–O_2 batteries",

Carbon, Vol 117, pp. 454-461. (2017)

8) Jinsoo Kim†, Hyeokjun Park†, Byungju Lee, Won Mo Seong, Hee-Dae Lim, **Youngjoon Bae**, Haegyeom Kim, Won Keun Kim, Kyoung Han Ryu, Kisuk Kang "Dissolution and Ionization of Sodium Superoxide in Sodium-Oxygen Batteries", *Nature Communications*, Vol 7, 10670. (2016)

9) Jaepyeong Jung†, KyeongSe Song†, **Youngjoon Bae**, Sang-Il Choi, Eunbi Cho, Kisuk Kang, Yong-Mook Kang "Achieving outstanding Li^+-ORR and -OER activities via edge- and corner- embedded bimetallic nanocubes for rechargeable Li-O_2 Batteries", *Nano Energy*, Vol 18, pp. 71-80. (2015)

10) Hee-Dae Lim†, Hyeokjun Park†, Hyungsub Kim, Jinsoo Kim, Byungju Lee, **Youngjoon Bae**, Hyeokjo Gwon, Kisuk Kang "A new perspective on Li-SO_2 batteries for rechargeable systems", *Angewandte Chemie International Edition*, Vol 54, pp. 9663-9667. (2015)

11) Hee-Dae Lim, Hyelynn Song, Jinsoo Kim, Hyeokjo Gwon, **Youngjoon Bae**, Kyu-Young Park, Jihyun Hong, Haegyeom Kim, Taewoo Kim, Yong Hyup Kim, Xavier Lepro, Raquel Ovalle-Robles, Ray H. Baughman, and Kisuk Kang "Superior Rechargeability and Efficiency of Li-O_2 Batteries: Hierarchical Air-electrode Architecture Combined with a Soluble Catalyst", *Angewandte Chemie International Edition*, Vol 53, pp.3926-3931. (2014)

12) Hee-Dae Lim, Hyelynn Song, Hyeokjo Gwon, Kyu-Young Park, Jinsoo Kim, **Youngjoon Bae**, Hyungsub Kim, Sung-Kyun Jung, Taewoo Kim, Yong Hyup Kim, Xavier Lepro, Raquel Ovalle-Robles, Ray H. Baughman and Kisuk Kang

"A New Catalyst-embedded Hierarchical Air Electrode for High-performance Li-O_2 Batteries", *Energy & Environmental Science*, Vol 6, pp. 3570-3575. (2013)

(3) Conferences

1) 2019. 04. Oral Presentation, KECS spring meeting, Jeju, Republic of Korea

2) 2018. 05. Oral Presentation, ECS spring meeting, Seattle, WA, USA

3) 2017. 05. Oral Presentation, ECS spring meeting, New Orleans, LA, USA

4) 2016. 11. Oral Presentation, ENGE meeting, Jeju, Republic of Korea

5) 2017. 10. Poster Presentation, KIM fall meeting, Daegu, Republic of Korea

6) 2014. 04. Poster Presentation, KECS spring meeting, Changwon, Republic of Korea

7) 2015. 10 Poster Presentation, Materials fair, Department of Materials and Science, Seoul National University, Republic of Korea

8) 2014. 09 Poster Presentation, Materials fair, Department of Materials and Science, Seoul National University, Republic of Korea

(4) Patents

1) "고농도 전해질을 포함하는 나트륨 공기 전지 / A SODIUM AIR BATTERY COMPRISING HIGH-CONCENTRATION ELECTROLYTE"

   - Korean Patent [KR] Application Number 1020170063848

   - United States of America Patent [US] Application Number 15/845807

   - China Patent [CN] Application Number 201711402729.1

2) "양극, 이를 포함하는 리튬 공기 전지 및 양극 제조방법 / Cathode, Lithium Air Battery comprising cathode, and Preparation method of cathode"

   - Korean Patent [KR] Application Number 1020170101711

- United States of America Patent [US] Application Number 15/402435

3) “고체전해질, 이를 포함하는 리튬전지 / Solid electrolyte, lithium battery comprising solid electrolyte”

- Korean Patent [KR] Application Number 1020160013538

- United States of America Patent [US] Application Number 15/715645

4) “전해액 첨가제, 이를 포함한 전해질, 상기 전해질을 포함한 양극, 상기 양극을 포함하는 리튬공기전지”

- Korean Patent [KR] Application Number 1020180043568

- United States of America Patent [US] Application Number 16/177496